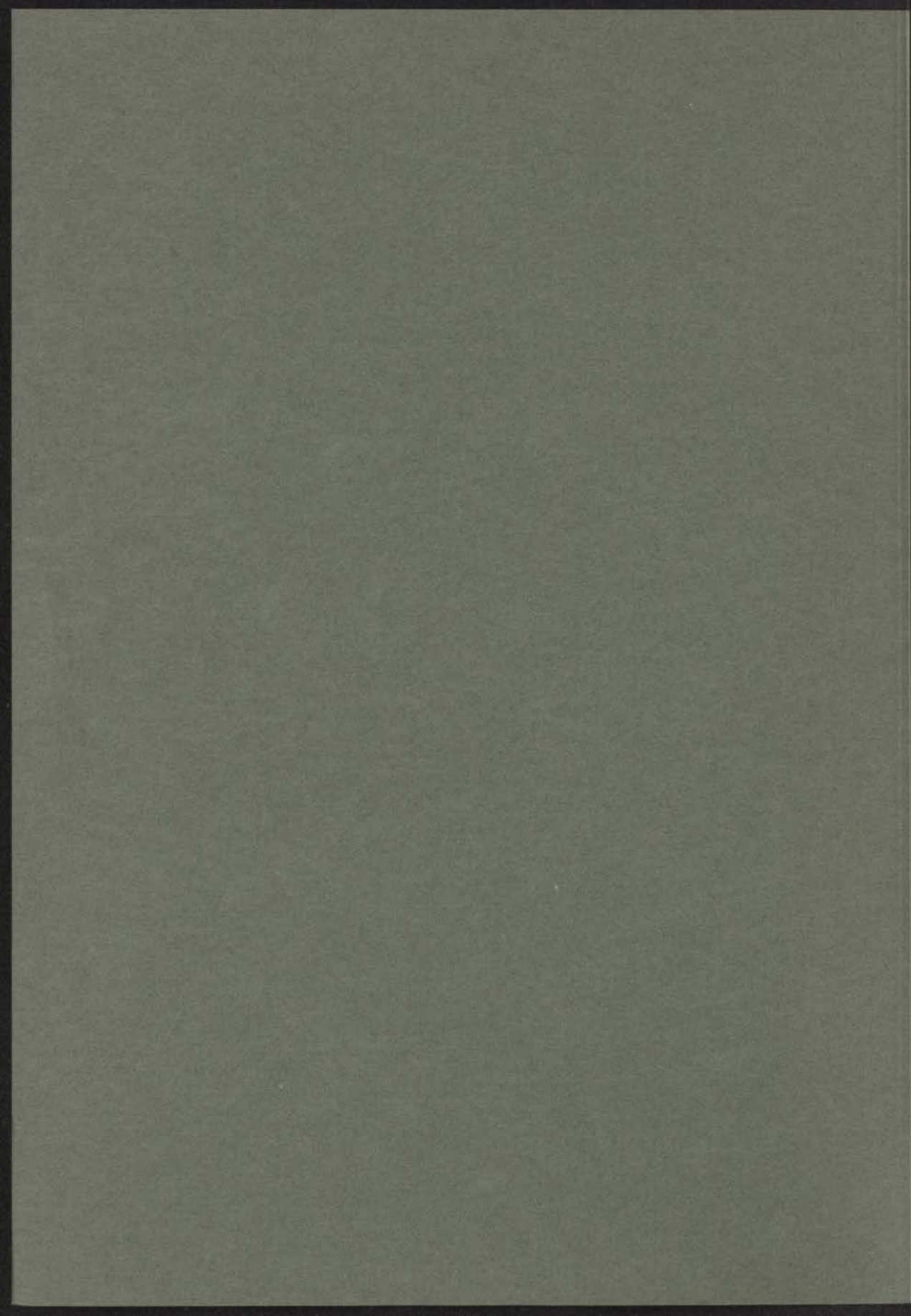


A STUDY OF EXCITATIONS IN  
FERROMAGNETIC NICKEL

E. FRIKKEE



14 JUNI 1973

# A STUDY OF EXCITATIONS IN FERROMAGNETIC NICKEL

PROEFSCHRIFT

TER VERKRIJGING VAN DE GRAAD VAN DOCTOR  
IN DE WISKUNDE EN NATUURWETENSCHAPPEN AAN  
DE RIJKSUNIVERSITEIT TE LEIDEN, OP GEZAG VAN  
DE RECTOR MAGNIFICUS DR. A.E. COHEN, HOOG-  
LERAAR IN DE FACULTEIT DER LETTEREN, VOL-  
GENS BESLUIT VAN HET COLLEGE VAN DEKANEN  
TE VERDEDIGEN OP DONDERDAG 21 JUNI 1973  
TE KLOKKE 16.15 UUR

DOOR

EVERT FRIKKEE

GEBOREN TE EDAM IN 1934

*kast dissertaties*

PROMOTOREN: Prof. Dr. J.A. Goedkoop  
Prof. Dr. G. de Vries

## STELLINGEN

1. Experimentele resultaten van Van Dingenen en Hautecler doen vermoeden dat de in dit proefschrift beschreven gemengde excitaties ook in ijzer waarneembaar zijn.

W. van Dingenen en S. Hautecler, *Physica* 37 (1967) 603.

2. Het is onwaarschijnlijk dat de lokale excitatie in Cu-10ZnAl, waargenomen door Nicklow e.a., zou kunnen worden toegeschreven aan geïsoleerde Al atomen. Nader onderzoek van deze excitatie langs verschillende symmetrierichtingen verdient aanbeveling.

R.M. Nicklow, P.R. Vijayaraghavan, H.G. Smith, G. Dolling en M.K. Wilkinson, in Neutron Inelastic Scattering, Vienna, IAEA (1968) Vol. I, p. 47.

3. De conclusie van Turrell, dat alleen roostervibraties met een golfvector  $\underline{k} = \underline{0}$  optisch actief kunnen zijn, berust op een onjuiste bewijsvoering.

G. Turrell, Infrared and Raman Spectra of Crystals, London, Academic Press (1972) p. 106.

4. Daar de selectieregels voor fotonabsorptie, fotonverstrooiing en neutronverstrooiing onderling verschillen, kan een combinatie van experimenten met behulp van deze methodes in veel gevallen zinvol zijn.

5. Voor de analyse van neutron-verstrooiingsexperimenten in de  $(\omega, Q)$ -ruimte is de gangbare methode, waarbij de variabelen  $\omega$  en  $Q$  worden gescheiden, te verkiezen boven de door Janner en La Fleur voorgestelde gegeneraliseerde Ewaldconstructie.

A.G.M. Janner en P.L. la Fleur, *Phys. Letters* 36A (1971) 109.

6. Tegen de door Liu gegeven verklaring voor de magnon-phonon wisselwerking in terbium zijn bezwaren aan te voeren.

S.H. Liu, Phys. Rev. Letters 29 (1972) 793.

7. De abrupte afname van de neutron-magnon verstrooiing in ferromagnetische 3d metalen boven een bepaalde drempelenergie van de magnonen wordt veelal toegeschreven aan de wisselwerking tussen magnonen en Stoner excitaties. Gezien de resultaten van een recent onderzoek aan nikkel door Mook e.a. is deze verklaring moeilijk te handhaven.

H.A. Mook, J.W. Lynn en R.M. Nicklow, Phys. Rev. Letters 30 (1973) 556.

8. De door Lowde e.a. toegepaste methode voor de analyse van waargenomen "extra" neutronverstrooiing in  $^{60}\text{Ni}$  is gebaseerd op een aantal veronderstellingen die slechts ten dele juist zijn.

R.D. Lowde en C.G. Windsor, Adv. Phys. 19 (1970) 813.

9. Het verdient aanbeveling om bij het experimentele onderzoek aan de ordening van roosterdefecten in kristallen gebruik te maken van neutronendiffractie.
10. De doeltreffendheid van experimenteel natuurkundig onderzoek wordt in belangrijke mate bepaald door de samenstelling van de groep onderzoekers die bij het project betrokken is. Het is vooral van belang dat deze groep zowel experimentele als theoretische elementen bevat.

## CONTENTS

CHAPTER I	INTRODUCTION	1
CHAPTER II	THEORY OF ALIGNED-BOY EXCITATION IN SUPERCONDUCTIVE NICKEL	
	2.1. Introduction	3
	2.2. Physical properties and group theory	3
	2.3. Phonons	15
	2.4. Excitons	14
	2.5. Electromagnetic excitations and magnets	17
CHAPTER III	THEORY OF THERMAL NEUTRON SCATTERING IN FERROMAGNETIC NICKEL	
	3.1. Introduction	21
	3.2. Magnetic and magnetic scattering	21
	3.3. Elastic scattering	25
	3.4. Inelastic scattering	29
	3.4.1. One-phonon scattering	30
	3.4.2. Magnetic magnetic scattering	35
	3.4.3. Selection rules	36
CHAPTER IV	EXPERIMENTAL TECHNIQUES	
	4.1. Introduction	37
	4.2. Time-of-flight spectrometer	37
	4.3. Triple-axis spectrometer	39
	4.4. Radiation	39
CHAPTER V	INTERPRETATION OF A NICKEL NEUTRON SCATTERING EXPERIMENT	
	5.1. Introduction	39
	5.2. Time-of-flight measurements	39
	5.3. Triple-axis experimental measurements	41
	5.3.1. Subtracting by phonon and phonon modes	41
	5.3.2. Subtracting by magnets	42
	5.4. Comparison of time-of-flight and triple-axis measurements	44
	5.5. Discussion	45

*Aan mijn ouders*





## C O N T E N T S

CHAPTER I	INTRODUCTION	1
CHAPTER II	THEORY OF ELEMENTARY EXCITATIONS IN FERROMAGNETIC NICKEL	
	2.1. Introduction	5
	2.2. Crystal symmetry and group theory	5
	2.3. Phonons	15
	2.4. Electrons	21
	2.5. Electron-hole excitations and magnons	27
CHAPTER III	THEORY OF THERMAL NEUTRON SCATTERING IN FERROMAGNETIC NICKEL	
	3.1. Introduction	31
	3.2. Nuclear and magnetic scattering	31
	3.3. Elastic scattering	36
	3.4. Inelastic scattering	39
	3.4.1. One-phonon scattering	40
	3.4.2. Inelastic magnetic scattering	43
	3.4.3. Selection rules	48
CHAPTER IV	EXPERIMENTAL TECHNIQUES	
	4.1. Introduction	50
	4.2. Time-of-flight spectrometer	50
	4.3. Triple-axis spectrometer	53
	4.4. Resolution	55
CHAPTER V	INVESTIGATION OF A NICKEL MULTIDOMAIN SINGLE CRYSTAL	
	5.1. Introduction	58
	5.2. Time-of-flight measurements	59
	5.3. Triple-axis spectrometer measurements	63
	5.3.1. Scattering by phonons and mixed modes	63
	5.3.2. Scattering by magnons	69
	5.4. Comparison of time-of-flight and triple-axis measurements	72
	5.5. Discussion	74

CHAPTER VI	INVESTIGATION OF NICKEL SINGLE-DOMAIN SINGLE CRYSTALS	
6.1.	A crucial experiment	77
6.2.	Choice of single-domain samples	80
6.3.	Time-of-flight measurements on $[001]$ , $[110]$ and $[111]$ domains	82
6.4.	Triple-axis measurements on a $[110]$ domain	88
6.5.	An experiment at liquid-nitrogen temperature	93
6.6.	Discussion	96
CHAPTER VII	DISCUSSION AND CONCLUSION	
7.1.	Introduction	104
7.2.	Observation of mixed modes and forbidden phonon scattering	104
7.3.	A possible interpretation of the mixed modes	107
7.4.	The detailed-balance condition	120
7.5.	Conclusion	123
APPENDIX A		127
APPENDIX B		137
APPENDIX C		143
REFERENCES		149
LIST OF SYMBOLS		154
SUMMARY		159
SAMENVATTING		161
NAWOORD		163

## CHAPTER I

### INTRODUCTION

The scattering of thermal neutrons is an effective means for the investigation of the structure and the dynamical properties of condensed matter in general and magnetic substances in particular. Owing to the fact that the neutron is subject to magnetic and nuclear interactions, it may create or annihilate elementary excitations both in the electron system (electron-hole excitations and magnons) and in the crystal lattice (phonons). From the dispersion relation, i.e. the relation between the frequency and the wave vector, for these elementary excitations one may obtain information about the interatomic force constants and the exchange interaction between the electrons. Hence the aim of neutron-phonon and neutron-magnon scattering experiments is usually the determination of the dispersion relation for these excitations.

As nickel single crystals may be easily obtained, it is not surprising that the phonon dispersion relation in nickel has been the subject of a number of previous investigations [1-3]. In nickel with the natural isotopic composition neutron-magnon scattering is quite weak in comparison with coherent and incoherent neutron-phonon scattering, and early investigations on magnons in natural Ni have therefore been restricted to the low-frequency range [4-7]. The study of magnetic excitations could be extended to higher frequencies when  $^{60}\text{Ni}$  single crystals became available [8-11]. In these samples the magnetic scattering cross section is the same as in natural Ni, whereas incoherent nuclear scattering is absent and the coherent nuclear scattering is an order of magnitude smaller than in natural Ni.

The main purpose of the present work is the investigation of the mutual interaction between elementary excitations in ferromagnetic nickel. Owing to the spin-orbit coupling of the electrons, the electron spin system interacts with the crystal lattice.

Some static magnetic properties of ferromagnets, notably magnetostriction and magnetic anisotropy, are directly related to this spin-lattice interaction. In addition, the interaction gives rise to dynamic effects, such as the coupling between magnons and phonons.

This coupling is particularly strong for magnons and phonons with approximately equal frequencies and wave vectors and results in the formation of mixed excitations, which are usually called magneto-elastic waves [12-14]. However, the perturbation of the phonons is not restricted to this relatively small frequency range. Along the whole dispersion relation one may expect small deviations in the polarization vectors and frequencies of the phonons, as a result of the fact that the interatomic force constants depend on the magnetization direction [15]. Magnon-phonon interference has been observed by Bömmel and Dransfeld by means of ferromagnetic resonance in nickel films at a frequency of 1 Ghz [16], and a variation in the velocity of ultrasound in nickel as a function of the magnetization direction has been observed by Alers et al. for a fixed sound frequency of 10 MHz [17]. The latter result is equivalent with a change of the phonon frequency at a fixed wave vector.

Inelastic scattering experiments with thermal neutrons are usually applied to observe excitations with frequencies larger than 1 THz, a limit which is well above the region where the resonant interference between magnons and phonons in nickel occurs. DeWit and Brockhouse [18] have made a search for magnetic perturbations in the phonon dispersion relation in nickel by carrying out phonon measurements along the main symmetry directions at 400 °C, i.e. above the Curie temperature  $T_c = 359$  °C, at 300 °C and at room temperature, and by comparing the phonon frequencies at these temperatures. It was found that the average frequency shifts could be explained by anharmonic effects, except for some branches, which exhibited frequency shifts almost twice as large as the average. The average result agrees with the conclusion from the ultrasound experiments, that the change in phonon frequency as a function of the field direction is extremely small (<0.1%). As the frequency shifts between 22 °C and 400 °C due to anharmonicity are of the order of 3%, the possible additional shift due to the change in saturation magnetization will be unobservable.

A change in the phonon polarization vectors, however, may be detected more easily by means of neutron scattering than a change in frequency.

In a cubic crystal, transverse phonons along the high-symmetry directions cannot give rise to neutron scattering if the scattering vector is parallel with the phonon wave vector. A lowering of the crystal symmetry by magnetoelastic interaction may be observed by looking for neutron-phonon scattering under experimental conditions for which these scattering processes would be forbidden if the crystal were cubic. Almost all experiments with the triple-axis spectrometer that will be described in chapter V and VI were performed in a configuration where scattering by purely transverse phonons is forbidden, and in this way magnetic perturbations of these phonons could be detected.

Although the spin-lattice interaction leads to an interference and mixing of excitations, the total number of perturbed elementary excitations, which is equal to the number of degrees of freedom in the crystal, is expected to remain the same. In the present report experimental evidence will be presented for the existence of an additional excitation in nickel which appears to possess both electronic and vibrational properties. The first experiments on a nickel multidomain crystal by means of the time-of-flight spectrometer were actually intended as control measurements in an investigation of an additional excitation observed in Ni(4% Fe), which was interpreted originally as a magnetic impurity mode connected with the iron atoms. It turned out, however, that this additional mode was also present in pure nickel, and the present work was to a large extent aimed at a further investigation of its properties. To this end an extensive use is made of group-theoretical selection rules that govern, on the one hand, the interaction of the new mode with magnons and phonons and, on the other hand, the neutron scattering by each of these excitations.

In chapter II a review is given of the theory of phonons and electronic excitations in a ferromagnetic metal, followed by a short summary of the theory of neutron scattering by these excitations in chapter III. The spectrometers used for the scattering experiments, which are installed at two of the horizontal beam facilities of the High Flux Reactor in Petten, are described in chapter IV. In the chapters V and VI the experimental results are presented, mainly according to the

chronological order of the experiments. In view of the unusual aspects of the results a large number of the recorded neutron spectra is inserted. A possible interpretation of the additional mode is suggested in chapter VII.

Some of the results given in this report have been published previously [19]. A comparison of preliminary data obtained for Ni(4% Fe) and Ni multidomain crystals has been given in a report [20], which is available on request.

## CHAPTER II

### THEORY OF ELEMENTARY EXCITATIONS IN FERROMAGNETIC NICKEL

#### 2.1. Introduction

In this chapter a review will be given of the theory of the low-energy elementary excitations in an itinerant ferromagnet like nickel. The theory of lattice vibrations (phonons) will be summarized in section 2.3. In analogy to the phonons, which are the collective elementary excitations in the crystal lattice, the Stoner excitations (single electron excitations) and magnons (collective electron excitations) are the elementary excitations in the system of itinerant electrons. As an introduction to the theory of these magnetic excitations, which will be presented in section 2.5, a short discussion of the electronic band structure will be given in section 2.4. The transformation properties of all these excitations are directly related to the symmetry of the crystal lattice, and may be treated quite generally by means of group theory. In section 2.2. a concise summary will be given of those theorems of group theory that are essential for the description of the excitations.

#### 2.2. Crystal symmetry and group theory

Nickel crystallizes in the face-centred cubic (f.c.c.) structure with a lattice constant  $a = 3.524 \text{ \AA}$ . One may define a primitive lattice, containing one atom per unit cell, by introducing the three basis vectors

$$\underline{a}_1 = \frac{a}{2}(0,1,1) \ , \ \underline{a}_2 = \frac{a}{2}(1,0,1) \ , \ \underline{a}_3 = \frac{a}{2}(1,1,0).$$

The volume  $v_0$  of the primitive cell, which may be written as  $\underline{a}_1 \cdot (\underline{a}_2 \times \underline{a}_3)$ , is equal to  $a^3/4$ . An arbitrary lattice point  $\underline{l} = (l_1, l_2, l_3)$  is defined as

$$\underline{l} = l_1 \underline{a}_1 + l_2 \underline{a}_2 + l_3 \underline{a}_3. \quad (2.1)$$

It will be shown below that the elementary excitations (or any particle within the crystal lattice) may be characterized by a wave vector  $\underline{q}$  in the reciprocal lattice, which is based on the vectors  $\underline{b}_1$ ,  $\underline{b}_2$  and  $\underline{b}_3$ , satisfying the conditions

$$\underline{b}_i \cdot \underline{a}_j = 2\pi \delta_{i,j}.$$

In explicit form the vectors  $\underline{b}_i$  are given by the expressions

$$\underline{b}_1 = 2\pi(\underline{a}_2 \times \underline{a}_3)/v_0, \quad \underline{b}_2 = 2\pi(\underline{a}_3 \times \underline{a}_1)/v_0, \quad \underline{b}_3 = 2\pi(\underline{a}_1 \times \underline{a}_2)/v_0,$$

and for the f.c.c. lattice in particular

$$\underline{b}_1 = 2\pi(\bar{1}, 1, 1)/a, \quad \underline{b}_2 = 2\pi(1, \bar{1}, 1)/a, \quad \underline{b}_3 = 2\pi(1, 1, \bar{1})/a.$$

A reciprocal lattice vector (or point)  $\underline{\tau} = (\tau_1, \tau_2, \tau_3)$  with integer components  $\tau_i$  is defined by means of

$$\underline{\tau} = \tau_1 \underline{b}_1 + \tau_2 \underline{b}_2 + \tau_3 \underline{b}_3$$

and has the property

$$\exp(i\underline{\tau} \cdot \underline{z}) = 1 \quad (2.2)$$

for any vector  $\underline{z}$  of the real lattice. The first Brillouin zone may be considered as the unit cell of the reciprocal lattice and is defined to consist of all the points  $\underline{q}$  that are closer to  $\underline{\tau} = \underline{0}$  than to any other reciprocal lattice point  $\underline{\tau}$ .

Owing to the symmetry properties of the crystal lattice, group theory may be applied to facilitate the computation of the energy of the elementary excitations and the electrons, to label the corresponding eigenfunctions according to their symmetry properties, and to establish the selection rules for interaction between electrons, phonons and magnons. The application of group theory to problems in solid-state physics has been treated extensively in various text-books [21-26], and only a brief outline of the theory will be given here.

#### Classification of eigenfunctions

Consider the time-independent Schrödinger equation for a general system:

$$H\Psi_i = E\Psi_i \quad (2.3)$$

$H$  is the Hamilton operator,  $\Psi_i$  is one of the eigenfunctions belonging to an  $l$ -fold degenerate level with energy  $E$ . If  $H$  is invariant under the transformations  $T$  of a finite group  $G$ , the  $l$  eigenfunctions belonging to the eigenvalue  $E$  constitute the basis for an  $l$ -dimensional, irreducible representation  $\Gamma(T)$  of the group  $G$ . The transformation properties of the  $l$  eigenfunctions  $\Psi_i$  are defined by



$$P(T)\psi_i = \sum_{j=1}^1 \Gamma_{ij}(T)\psi_j \quad (2.4)$$

for  $i = 1, \dots, 1$ , where  $P(T)$  is the operator corresponding to the transformation  $T$ .

A relation similar to (2.4) holds for the expansion of a function in the subspace, which is spanned by the orthogonal set of  $n$  eigenfunctions, belonging to a finite set of energy eigenvalues. The  $n$ -dimensional representation  $\Gamma(T)$  corresponding to this basis of eigenfunctions may be decomposed into a number of irreducible representations of  $G$ , which may be written as

$$\Gamma(T) = c_1 \Gamma^1(T) \oplus c_2 \Gamma^2(T) \oplus \dots \oplus c_\alpha \Gamma^\alpha(T) \quad (2.5)$$

The coefficients  $c_\alpha$  are given by

$$c_\alpha = \frac{1}{g} \sum_T \chi_\alpha^*(T) \chi(T), \quad (2.6)$$

where the summation is over all the elements in  $G$ ,  $g$  is the number of these elements, and the characters  $\chi_\alpha(T)$  and  $\chi(T)$  are the traces of the matrices  $\Gamma^\alpha(T)$  and  $\Gamma(T)$ . Hence, each eigenfunction belongs to a specific irreducible representation of  $G$ , and may be labelled accordingly. To determine the function  $\psi_i^\alpha$  that transforms according to the  $i$ -th row of  $\Gamma^\alpha$  one may apply the projection operators  $P_{ij}^\alpha$  defined by

$$P_{ij}^\alpha = \frac{1}{g} \sum_T \Gamma_{ij}^{\alpha*}(T) P(T) \quad (2.7)$$

where  $l_\alpha$  denotes the dimension of the irreducible representation  $\Gamma^\alpha$ . The operator  $P_{ii}^\alpha$ , in particular, projects the function  $\psi_i^\alpha$  out of an arbitrary linear combination  $\psi$  of the  $n$  basis functions, i.e. if  $\psi$  contains  $\psi_i^\alpha$  with a coefficient  $A_i$ :

$$P_{ii}^\alpha \psi = A_i \psi_i^\alpha \quad (2.8)$$

The functions  $\psi_j^\alpha$  transforming according to the other rows of  $\Gamma^\alpha$  may be obtained from  $\psi_i^\alpha$  by means of the projection

$$P_{ji}^\alpha \psi_i^\alpha = \psi_j^\alpha. \quad (2.9)$$

#### Subduction and compatibility

Suppose that  $G'$  is a subgroup of  $G$ . In this case, the irreducible representations of  $G$  and  $G'$  are connected by compatibility relations,

which may be derived by means of the subduction procedure described below (see ref. [26], p.89,219). Consider an irreducible representation  $\Gamma^\alpha(T)$  of  $G$ . The set of matrices  $\Gamma_{(s)}^\alpha(T')$  from  $\Gamma^\alpha(T)$ , corresponding to the elements  $T'$  of  $G'$  will be referred to as the representation of  $G'$  that is subduced by the representation  $\Gamma^\alpha(T)$  of  $G$ . In general,  $\Gamma_{(s)}^\alpha(T')$  may be decomposed into irreducible representations  $\Gamma^\beta(T')$  of  $G'$  by applying (2.5) and (2.6), where the summation in (2.6) is restricted to the elements  $T'$ . The irreducible representations  $\Gamma^\alpha(T)$  of  $G$  and  $\Gamma^\beta(T')$  of  $G'$  are compatible if  $\Gamma^\beta(T')$  appears in the decomposition of the subduced representation  $\Gamma_{(s)}^\alpha(T')$ .

Subduction will be applied frequently in this report,

- (a) to investigate the influence of a reduction in the symmetry of the crystal on the transformation properties of the eigenfunctions;
- (b) to determine the selection rules for neutron scattering by excitations with a specific wave vector  $\underline{q}$ ;
- (c) to establish the compatibility for branches of dispersion relations between directions and points with different symmetries in the reciprocal lattice.

### Bloch's theorem

Let us now consider a Hamiltonian that is invariant under the symmetry operations that constitute the space group  $G$  of the crystal. For the f.c.c. lattice of nickel the space group is symmorphic, i.e. every symmetry operation  $T = \{R|\underline{n}\}$  of  $G$  is a combination of a rotation  $R$  and a primitive translation  $\underline{n} = n_1\underline{a}_1 + n_2\underline{a}_2 + n_3\underline{a}_3$ . The rotations  $R$  constitute the point group  $G_0$ , where  $R$  may be a proper or improper rotation, the latter being a combination of a proper rotation and space inversion  $I$ . For convenience the total number of lattice sites  $\underline{L}$  (see the definition in (2.1)) is taken equal to  $N = N_1N_2N_3$  by introducing the restriction that  $\underline{L}_i$  can take the values  $0, 1, \dots, (N_i-1)$ . In addition, cyclic boundary conditions are introduced: it is assumed that any eigenfunction  $\Psi(\underline{r})$  satisfies the conditions

$$\Psi(\underline{r}) = \Psi(\underline{r} + N_1\underline{a}_1) = \Psi(\underline{r} + N_2\underline{a}_2) = \Psi(\underline{r} + N_3\underline{a}_3) \quad (2.10)$$

The group of  $N$  primitive translations  $\{E|\underline{n}\}$  ( $E$  is the identity element of  $G_0$ ) is a subgroup  $T$  of  $G$ , and an arbitrary eigenfunction  $\Psi(\underline{r})$  must transform according to one of the irreducible representations  $\Gamma^\alpha$  of  $T$ . It can be shown (cf. [24], p.76) that these representations are all one-dimensional and may be labelled by means of  $N$  wave vectors  $\underline{q}$  in reciprocal space

$$\underline{q} = q_1 \underline{b}_1 + q_2 \underline{b}_2 + q_3 \underline{b}_3,$$

where  $q_i$  can take any of the values  $0, 1/N_i, \dots, (N_i-1)/N_i$ . Hence, there are  $N$  irreducible representations  $\Gamma^{\underline{q}}$ , which are given by

$$\Gamma^{\underline{q}}\{E|\underline{n}\} = \exp(i\underline{q} \cdot \underline{n}), \quad (2.11)$$

and it may be readily verified that the functions transforming as  $\Gamma^{\underline{q}}$  must be of the form

$$\Psi_{\underline{q}}(\underline{r}) = \exp(i\underline{q} \cdot \underline{r}) u_{\underline{q}}(\underline{r}), \quad (2.12)$$

where  $u_{\underline{q}}(\underline{r})$  has the periodicity of the lattice:

$$u_{\underline{q}}(\underline{r}) = u_{\underline{q}}(\underline{r} + \underline{n}).$$

The wave vector  $\underline{q}$  in (2.11) may be defined to be within the first Brillouin zone, because  $\exp\{i(\underline{q} + \underline{\tau}) \cdot \underline{n}\} = \exp(i\underline{q} \cdot \underline{n}) \exp(i\underline{\tau} \cdot \underline{n}) = \exp(i\underline{q} \cdot \underline{n})$  according to (2.2).

The results above are known as Bloch's theorem [27], and are valid for the eigenfunctions of an arbitrary excitation or particle within the lattice. The function  $u_{\underline{q}}(\underline{r})$  characterizes the specific excitation or particle, and transforms according to one of the irreducible representations  $\Gamma^\alpha$  of the point group of  $\underline{q}$ ,  $G_0(\underline{q})$ . This is a subgroup of  $G_0$  and consists of those operations  $\{R|0\}$  that transform  $\underline{q}$  into itself (or, if  $\underline{q}$  is a point on the zone boundary, into  $\underline{q} + \underline{\tau}$ , where  $\underline{\tau}$  is a reciprocal lattice vector). The irreducible representations of the point groups may be found in existing tables [22-26, 28, 29] and by means of the projection operators (2.7) the functions  $u_{\underline{q}}(\underline{r})$  transforming according to  $\Gamma^\alpha$  may be determined. In the following sections of this chapter and in section 7.3 some applications of this procedure will be given.

### Selection rules

The classification of the eigenfunctions by means of the irreducible

representations of  $G$  is particularly useful to establish selection rules for the mutual interaction between electrons, magnons and phonons, and for their interaction with neutrons. If two particles or quasi-particles occupy eigenstates of a Hamiltonian  $H_0$ , and if the interaction operator has the same or a higher symmetry than  $H_0$ , the interaction between the particles or quasi-particles is allowed by symmetry if their eigenfunctions transform according to the same irreducible representation of the group  $G$  of  $H_0$ .

If, on the other hand, the interaction operator has a lower symmetry than  $H_0$ , the selection rules are obtained in the following way. Consider, for example, the electron-phonon interaction, and suppose that the Hamiltonian  $H$  for the electrons contains an interaction operator  $H'(\underline{r})$  corresponding to the electron-phonon interaction:

$$H = H_0 + H' ,$$

where  $H_0$  is the Hamiltonian of the unperturbed electron system. In general  $H'$  may consist of various terms that transform as different irreducible representations of the space group  $G$ , but it will be assumed here for simplicity that  $H'$  transforms as a specific row of the irreducible representation  $\Gamma^P$  of  $G$ . Transitions between the electron states  $\psi_i$  and  $\psi_f$ , which transform as  $\Gamma^i$  and  $\Gamma^f$ , may be induced by electron-phonon interaction if the decomposition of the direct product representation  $\Gamma = \Gamma^P \otimes \Gamma^i$  contains  $\Gamma^f$ . According to (2.5) and (2.6) this is the case if

$$c_f^{pi} = \frac{1}{g_T} \chi_f^*(T) \chi_p(T) \chi_i(T) \neq 0 , \quad (2.13)$$

as the characters of the direct product representation  $\Gamma^P \otimes \Gamma^i$  are given by

$$\chi(T) = \chi_p(T) \chi_i(T).$$

Thus selection rules for the interaction between particles and quasi-particles may be derived from the symmetry properties of  $H_0$  and  $H'$ , and the eigenfunctions of the particles involved, by means of the corresponding character tables.

### Double-valued representations

The theory described above is only applicable to electron states in a crystal if the Hamiltonian does not contain spin-dependent terms. For the explanation of the experimental results it will be necessary to invoke electron spin-orbit coupling, which has as consequence that double groups and double-valued representations must be used to classify the electron eigenfunctions [30-32].

The transformation properties of the spin functions  $u_{\pm\frac{1}{2}}$  of a particle with spin  $\pm\frac{1}{2}$  along the z-axis, under a rotation  $R(\phi)$  about this axis, are given by

$$R(\phi) u_{\pm\frac{1}{2}} = \exp(\pm\frac{1}{2}i\phi) u_{\pm\frac{1}{2}}, \quad (2.14)$$

where  $\phi$  is the angular coordinate in the xy-plane. A characteristic property of these functions is the change in sign under a rotation of  $360^\circ$  about the z-axis, and this leads to a doubling of the number of transformations. For each proper rotation  $R$  there is an additional "barred" rotation  $\bar{R} = \bar{E}R$  ( $\bar{E}$  is a rotation of  $360^\circ$ ), which may be distinguished from  $R$  because it changes the sign of the spin functions. Therefore one has to introduce double-valued representations  $\Gamma_D^\beta$  for particles with spin  $\frac{1}{2}$ :

$$\Gamma_D^\beta(\bar{R}) = -\Gamma_D^\beta(R) \quad (2.15)$$

For the representations corresponding to improper rotations  $IR$  one usually follows the convention (cf. [22], p.87) to assume that the spin functions are invariant under space inversion.

If the two-dimensional representation based on the spin functions  $u_{\pm\frac{1}{2}}$  is denoted by  $D_{\frac{1}{2}}$ , and the single-valued irreducible representations of  $u_{\underline{q}}(\underline{r})$  by  $\Gamma_S^\alpha$ , the double-valued irreducible representations  $\Gamma_D^\beta$  for the functions  $u_{\underline{q}}(\underline{r})u_{\pm\frac{1}{2}}$  are obtained by means of a reduction of the direct-product representation:

$$\Gamma_S^\alpha \otimes D_{\frac{1}{2}} = c_{\alpha 1} \Gamma_D^1 \oplus c_{\alpha 2} \Gamma_D^2 \oplus \dots \oplus c_{\alpha \beta} \Gamma_D^\beta \quad (2.16)$$

The numbers  $c_{\alpha\beta}$  are derived from an equation similar to (2.13):

$$c_{\alpha\beta} = \frac{1}{g_o(\underline{q})} \sum_R \chi_\beta^*(R) \text{Tr}\{D_{\frac{1}{2}}(R)\} \chi_\alpha(R), \quad (2.17)$$

where the summation is over all (proper and improper) rotations of the single group  $G_0(\underline{q})$  and  $g_0(\underline{q})$  denotes the order of  $G_0(\underline{q})$ . The traces of the matrices  $D_{\frac{1}{2}}$  may be found in table A.2.

Time-reversal symmetry

Up to this point, we have only considered the symmetry properties of the eigenvalue equation (2.3) with respect to coordinate transformations. Since the energy eigenvalues are real, taking the complex conjugate of (2.3) yields

$$H \psi_{\underline{q}}^*(\underline{r}) = E_{\underline{q}} \psi_{\underline{q}}^*(\underline{r}),$$

if the Hamiltonian is real. Hence the energies of the states corresponding to  $\psi_{\underline{q}}^*$  and  $\psi_{\underline{q}}$  are equal, while  $\psi_{\underline{q}}^*$  transforms as  $\Gamma^{\alpha*}$  if  $\psi_{\underline{q}}$  transforms as  $\Gamma^{\alpha}$ . The term "time reversal" for taking the complex conjugate is commonly used, because complex conjugation of the time-dependent Schrödinger equation  $H\psi = i\hbar\partial\psi/\partial t$  gives rise to time reversal:  $H\psi^* = i\hbar\partial\psi^*/\partial(-t)$ . Time reversal and taking the complex conjugate are two examples of anti-unitary operators (see [21], p.328).

The existence of additional degeneracies due to time-reversal symmetry will in general depend on the relation between  $\Gamma^{\alpha}$  and  $\Gamma^{\alpha*}$ . According to Wigner [33] one may distinguish three cases:

- (a)  $\Gamma$  is equivalent to a real representation,
- (b)  $\Gamma$  is not equivalent to  $\Gamma^*$ ,
- (c)  $\Gamma$  is equivalent to  $\Gamma^*$ , but not equivalent to a real representation.

In case (a) no additional degeneracy occurs, whereas there is a doubling of the degeneracy in cases (b) and (c). This rule applies to single-valued representations; for double-valued representations the corresponding rule will be given below.

A straightforward method to decide to which case a particular representation  $\Gamma_S^{\alpha}$  of the point group  $G_0(\underline{q})$  belongs, is the application of the following criterion

$$\sum \chi^{\alpha}(\{Q|0\}^2) = \begin{cases} g_0(\underline{q}) & : \text{case (a)} \\ 0 & : \text{case (b)} \\ -g_0(\underline{q}) & : \text{case (c)} \end{cases} \quad (2.18)$$

The summation in (2.18) is over those elements  $\{Q|0\}$  of the point group  $G_0$  that transform  $\underline{q}$  into  $-\underline{q}$  or  $-\underline{q}+\underline{r}$ . Obviously the elements  $\{Q|0\}^2$  belong to  $G_0(\underline{q})$ , whereas  $\{Q|0\}$  in general does not belong to  $G_0(\underline{q})^*$ .

The same criterion (2.18) may be used for the double-valued representations  $\Gamma_D^\beta$ , if the summation is extended over the rotations  $\bar{Q}$  of the double point group  $G_0$  that transform  $\underline{q}$  into  $-\underline{q}$  or  $-\underline{q}+\underline{r}$ . However, the rules for the doubling of the degeneracy are reversed: in cases (a) and (b) the degeneracy is doubled, whereas no additional degeneracy occurs in case (c).

### Magnetic groups

Owing to the existence of a net magnetization, a ferromagnetic crystal has a lower symmetry than a paramagnetic crystal [34,35]. The magnetic point group consists of the operations that take the crystal lattice into itself and leave the magnetization  $\underline{M}$  invariant. Since  $\underline{M}$  is a pseudo-vector, its direction is reversed under reflection in a plane containing  $\underline{M}$ , and therefore only the identity E, the inversion I, rotations  $C_{nM}$  around the direction of  $\underline{M}$  and reflections  $IC_{nM}$  can be elements in the magnetic point group. On the other hand, the magnetization changes sign under time reversal  $\Theta$  and consequently a combination of  $\Theta$  and a coordinate transformation that takes  $\underline{M}$  into  $-\underline{M}$  also belongs to the magnetic point group. Hence the magnetic point group consists of unitary elements (R) and anti-unitary elements ( $\Theta R$ ).

In a similar way one arrives at the following definition of the magnetic point group of the wave vector,  $M(\underline{q})$

$$M(\underline{q}) = G_0^M(\underline{q}) + \Theta G_1(\underline{q}).$$

$G_0^M(\underline{q})$  consists of the unitary elements of the magnetic point group that transform  $\underline{q}$  into  $\underline{q}$  or  $\underline{q}+\underline{r}$ , whereas  $\Theta G_1(\underline{q})$  consists of the anti-unitary elements of the magnetic point group that transform  $\underline{q}$  into  $-\underline{q}$  or  $-\underline{q}+\underline{r}$ .

---

\* )  $\{Q|0\}$  is an element of  $G_0(\underline{q})$  if  $G_0(\underline{q})$  contains I; in all other cases  $\{Q|0\}$  belongs to  $IG_0(\underline{q})$  [23].

The number of elements in  $G_o^M(\underline{q})$  is equal to the number of elements in  $\Theta G_1(\underline{q})$ .  $G_1(\underline{q})$  itself is not a group (it does, for example, not contain the identity operation E), but the elements in  $G_o^M(\underline{q})$  and  $G_1(\underline{q})$  together constitute a group, which will be indicated by  $G_2(\underline{q})$ . The point group  $M(\underline{q})$  will be denoted according to the Schönflies notation  $G_2(G_o^M)$ , used previously by Dimmock and Wheeler |35|.

The concept of magnetic point groups may be illustrated by the following example. Consider a wave vector  $\underline{q}$  along the z-axis of the reciprocal lattice, i.e. parallel with the vector  $(\underline{b}_1 + \underline{b}_2)/2$ , where  $\underline{b}_1$  and  $\underline{b}_2$  are defined on page 6. In the paramagnetic phase the point group  $G_o(\underline{q})$  is  $C_{4v}$ , which consists of 8 elements: E,  $C_{2z}$ ,  $C_{4z}$ ,  $C_{4z}^{-1}$ ,  $IC_{2x}$ ,  $IC_{2y}$ ,  $IC_{2a}$  and  $IC_{2b}$  (the operations are defined in appendix A). In the ferromagnetic phase with the magnetization directed along  $[110]$  (the  $\underline{a}$ -direction), only the elements E and  $IC_{2a}$  remain symmetry operations, i.e.  $G_o^M(\underline{q}) = C_s$ . In addition there are two anti-unitary symmetry operations  $\Theta C_{2b}$  and  $\Theta IC_{2z}$  |36|; the rotational components  $C_{2b}$  and  $IC_{2z}$ , together with E and  $IC_{2a}$ , constitute the point group  $C_{2v}$ , and the magnetic point group  $M(\underline{q})$  is therefore  $C_{2v}(C_s)$  (see table 6.2).

The symmetry properties and the essential degeneracies of the eigenfunctions in the ferromagnetic phase are determined by the irreducible representations of the unitary subgroup  $G_o^M(\underline{q})$  of  $M(\underline{q})$ . Additional degeneracies may occur due to the anti-unitary elements in  $M(\underline{q})$ , and a criterion similar to (2.18) may be applied to distinguish three different cases (see, for example, |21|, p.343, or |35|). We shall not consider this criterion in detail, since this would require a rather lengthy discussion of the so-called corepresentations of  $M(\underline{q})$ . It can be shown that no additional degeneracies will occur for the single domains magnetized along  $[001]$ ,  $[110]$  or  $[111]$ , that were investigated in the present work. For these domains the magnetic point groups  $M(\underline{q})$  for the symmetry points and lines of the reciprocal lattice have been tabulated in |36| (see also table 6.2). By inspection of existing tables of corepresentations |25,37| it may be verified that for the point groups  $M(\underline{q})$  relevant to the investigation on single domains no additional degeneracies exist, neither for the single-valued nor for the double-valued representations.



### Pseudo-magnetic groups

If the Hamiltonian of a system is invariant under a reversal of the magnetization  $\underline{M}$ , the eigenstates with wave vector  $\underline{q}$  transform according to the irreducible representations of the pseudo-magnetic point group  $G_0^{+M}(\underline{q})$ . This group consists of those elements of the crystal point group  $G_0$  that transform  $\underline{q}$  into itself (or, if  $\underline{q}$  is a point on the zone boundary, into  $\underline{q}+\underline{\tau}$ ) and  $\underline{M}$  into  $\underline{M}$  or  $-\underline{M}$ . For the case considered above, i.e.  $\underline{q}$  along the  $z$ -axis in a  $[110]$  domain, the pseudo-magnetic point group  $G_0^{+M}(\underline{q}) = C_{2v}$ , and consists of the elements  $E$ ,  $C_{2z}$ ,  $IC_{2a}$  and  $IC_{2b}$ . The operations  $E$  and  $IC_{2a}$  leave  $\underline{M}$  invariant, whereas  $C_{2z}$  and  $IC_{2b}$  transform  $\underline{M}$  into  $-\underline{M}$ .

### 2.3. Phonons

In this section a survey of the theory of non-interacting phonons will be given [38,39]. In addition to the cyclic boundary conditions (2.10), two other approximations are usually made:

- (a) The adiabatic approximation. It is assumed that the electronic wave functions are at any time determined by the instantaneous positions of the nuclei.
- (b) The harmonic approximation. The motion of an atom due to the potential generated by the other atoms is assumed to be harmonic. In other words, the series expansion of the potential in terms of atomic displacements is terminated at the quadratic term.

Consider a Bravais lattice consisting of  $N$  atoms with equal mass  $M^*$  at positions

$$\underline{R}_l(t) = \underline{l} + \underline{u}_l(t), \quad (2.19)$$

where  $\underline{l}$  is the equilibrium position of the  $l$ -th atom, and  $\underline{u}_l(t)$  the displacement from this position due to thermal vibration. In the harmonic approximation the classical equation of motion for  $\underline{u}_l(t)$  reads

$$M \ddot{u}_l^\alpha = - \sum_{\beta, l'} \phi_{\alpha\beta}(\underline{l}-\underline{l}') u_{l'}^\beta, \quad (2.20)$$

---

\*)  $M = \langle M \rangle_{Ni} = 97.48 \times 10^{-24}$  g.

where  $\alpha$  and  $\beta$  denote the Cartesian coordinate directions and  $\phi_{\alpha\beta}$  the elements of the interatomic force constant matrices. Since Bloch's theorem is based on the periodicity of the lattice and cyclic boundary conditions, it may also be applied to classical equations of motion. Hence  $\underline{u}_l(t)$  may be expanded in  $3N$  normal vibrations:

$$\underline{u}_l(t) = \sum_{j=1}^3 \sum_{\mathbf{q}}^N \underline{\xi}_j(\mathbf{q}) \exp\{i\mathbf{q} \cdot \underline{L} - i\omega_j(\mathbf{q})t\}. \quad (2.21)$$

Each normal mode is characterized by its wave vector  $\mathbf{q}$ , its polarization vector  $\underline{\xi}_j(\mathbf{q})$  and its angular frequency  $\omega_j(\mathbf{q})$ . The summation in (2.21) runs over  $N$  discrete vectors  $\mathbf{q}$  confined to the Brillouin zone. After substitution of (2.21) in (2.20), the following set of  $3N$  homogeneous equations for the  $\underline{\xi}$ 's is obtained:

$$M\omega_j^2(\mathbf{q})\underline{\xi}_j^\alpha(\mathbf{q}) = \sum_{\beta} D_{\alpha\beta}(\mathbf{q})\underline{\xi}_j^\beta(\mathbf{q}). \quad (2.22)$$

The dynamical matrix  $\underline{D}$  is directly related to the force constant matrix  $\underline{\phi}$ :

$$D_{\alpha\beta}(\mathbf{q}) = \sum_{\underline{L}, \underline{L}'} \phi_{\alpha\beta}(\underline{L}-\underline{L}') \exp\{-i\mathbf{q} \cdot (\underline{L}-\underline{L}')\}. \quad (2.23)$$

The condition for the existence of non-trivial solutions  $\underline{\xi}_j$  of (2.22) is

$$\det |M\omega_j^2(\mathbf{q})\underline{E} - \underline{D}(\mathbf{q})| = 0, \quad (2.24)$$

where  $\underline{E}$  denotes the unit matrix. This secular equation yields three solutions  $\omega_j(\mathbf{q})$ , and after substitution in (2.22) the corresponding vectors  $\underline{\xi}_j(\mathbf{q})$  are found. The general form of the matrix elements  $\phi_{\alpha\beta}(\underline{L}-\underline{L}')$  and  $D_{\alpha\beta}$  for an f.c.c. lattice is given in tables 2.1 and 2.2 for interactions ranging out to fourth neighbours.

The calculation of the frequencies and polarization vectors along symmetry directions may be simplified considerably by applying group-theoretical methods [40-43]. Although derived from a classical equation of motion, (2.22) may be considered as an eigenvalue equation similar to (2.3):

$$\underline{D}(\mathbf{q})\underline{\xi}_j(\mathbf{q}) = M\omega_j^2(\mathbf{q})\underline{\xi}_j(\mathbf{q}), \quad (2.25)$$

Table 2.1.

Interatomic force constant matrices  $\underline{\phi}(\underline{l-l'})$   
for the first four neighbours in nickel.

neighbour	$\underline{l-l'}$	$\underline{\phi}(\underline{l-l'})$	exp. values in dyne/cm <sup>2</sup>
first	$\frac{a}{2}(1,1,0)$	$\begin{pmatrix} \alpha_1 & \gamma_1 & 0 \\ \gamma_1 & \alpha_1 & 0 \\ 0 & 0 & \beta_1 \end{pmatrix}$	$\alpha_1 = 17,178$ $\beta_1 = -26$ $\gamma_1 = 19,316$
second	$\frac{a}{2}(2,0,0)$	$\begin{pmatrix} \alpha_2 & 0 & 0 \\ 0 & \beta_2 & 0 \\ 0 & 0 & \beta_2 \end{pmatrix}$	$\alpha_2 = 880$ $\beta_2 = -519$
third	$\frac{a}{2}(2,1,1)$	$\begin{pmatrix} \alpha_3 & \gamma_3 & \gamma_3 \\ \gamma_3 & \beta_3 & \delta_3 \\ \gamma_3 & \delta_3 & \beta_3 \end{pmatrix}$	$\alpha_3 = 626$ $\beta_3 = 320$ $\gamma_3 = 453$ $\delta_3 = -173$
fourth	$\frac{a}{2}(2,2,0)$	$\begin{pmatrix} \alpha_4 & \gamma_4 & 0 \\ \gamma_4 & \alpha_4 & 0 \\ 0 & 0 & \beta_4 \end{pmatrix}$	$\alpha_4 = 275$ $\beta_4 = -160$ $\gamma_4 = 424$

Table 2.2.

Elements of the dynamical matrix  $\underline{D}$  for an f.c.c. lattice.  
Forces between the first four neighbours are taken into account.

$$D_{ii} = 4\alpha_1\{2 - c_i(c_j + c_k)\} + 4\beta_1(1 - c_j c_k) + \\ 2\alpha_2(1 - C_i) + 2\beta_2(2 - C_j - C_k) + \\ 8\alpha_3(1 - C_i c_j c_k) + 8\beta_3\{2 - c_i(C_j c_k + c_j C_k)\} + \\ 4\alpha_4\{2 - C_i(C_j + C_k)\} + 4\beta_4(1 - C_j C_k)$$

$$D_{ij} = 4\gamma_1 s_i s_j + \\ 8\delta_3 c_k (S_i s_j + s_i S_j) + 8\gamma_3 C_k s_i s_j + \\ 4\gamma_4 S_i S_j$$

Notation:  $c_i = \cos(aq_i/2)$ ,  $s_i = \sin(aq_i/2)$

$C_i = \cos(aq_i)$  ,  $S_i = \sin(aq_i)$

In this table  $i$ ,  $j$  and  $k$  have been used to denote the Cartesian coordinate directions, in order to avoid confusion between the coordinates and the force constants. In the expression for  $D_{ii}$ ,  $j$  and  $k$  are the two remaining directions. In the expression for  $D_{ij}$ ,  $k$  denotes the third direction.

where  $M\omega_j^2(\underline{q})$  and  $\underline{\xi}_j(\underline{q})$  are the eigenvalues and eigenvectors of the operator  $\underline{D}; \underline{\xi}_j(\underline{q})$  may be identified with the function  $u_{\underline{q}}(\underline{r})$  in (2.12). According to equation (2.23)  $\underline{D}$  depends only on the lattice vectors  $(\underline{l}-\underline{l}')$  and on  $\underline{q}$ , and is therefore invariant under the operations of  $G_0(\underline{q})$ . Consequently, the eigenvectors transform according to the irreducible representations of  $G_0(\underline{q})$ . For the classification of the normal modes the notation of Bouckaert et al. [44] will be used; the symbols for the symmetry lines and points of the Brillouin zone are indicated in figure 2.1. In accord with common practice, we shall denote  $\underline{q}$  by its components  $q_x, q_y$  and  $q_z$  in the orthogonal coordinate system based on the vectors

$$\underline{b}_x = 2\pi(1,0,0)/a, \quad \underline{b}_y = 2\pi(0,1,0)/a, \quad \underline{b}_z = 2\pi(0,0,1)/a.$$

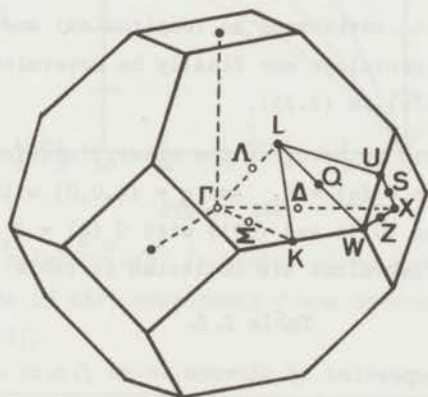


Figure 2.1.

*Brillouin zone of the f.c.c. lattice.  
Symmetry points and lines have been  
indicated in BSW notation [44].*

As an example of the group-theoretical treatment of the lattice vibrations we shall consider the phonons with  $\underline{q} = (\zeta, \zeta, \zeta)$ . The three eigenvectors  $\underline{\xi}_j$  are unit vectors in real space and constitute the basis for a three-dimensional representation  $\Gamma(R)$ . For the Ni crystal  $\Gamma(R)$  is equivalent to the group of six transformation matrices  $\underline{R}$  for the vector  $(x,y,z)$  (see table A.1), corresponding to the six symmetry operations of  $G_0(\zeta, \zeta, \zeta) = C_{3v}$ . From the character table for  $C_{3v}$  (table A.13) and the characters  $\chi(R)$

$$\chi(E) = 3, \quad \chi(C_{3\delta}) = \chi(C_{3\delta}^{-1}) = 0, \quad \chi(IC_{2b}) = \chi(IC_{2d}) = \chi(IC_{2e}) = 1$$

one obtains by means of (2.6):

$$c(\Lambda_1) = 1, \quad c(\Lambda_2) = 0, \quad c(\Lambda_3) = 1,$$

and  $\Gamma$  may therefore be decomposed as follows:

$$\Gamma = \Lambda_1 \oplus \Lambda_3.$$

Consequently, the phonon dispersion relation  $\omega_j(\mathbf{q})$  along  $[111]$  consists of a doubly degenerate branch ( $\Lambda_3$ ) and a non-degenerate branch ( $\Lambda_1$ ). By applying the projection operator (2.8) to an arbitrary vector  $(x, y, z)$  one obtains the eigenvectors

$$\underline{\xi}(\Lambda_1) = 3^{-\frac{1}{2}}(1, 1, 1), \quad \underline{\xi}_1(\Lambda_3) = 2^{-\frac{1}{2}}(1, \bar{1}, 0), \quad \underline{\xi}_2(\Lambda_3) = 6^{-\frac{1}{2}}(1, 1, \bar{2}). \quad (2.26)$$

It is readily verified that the eigenvectors are orthogonal, and that the branches  $\Lambda_1$  and  $\Lambda_3$  correspond to longitudinal and transverse phonons, respectively. The eigenvalues may finally be determined by substituting the eigenvectors (2.26) in (2.25).

The same procedure can be used for the other directions with high symmetry,  $\mathbf{q} = (0, \zeta, \zeta)$  with  $G_o(\mathbf{q}) = C_{2v}$  and  $\mathbf{q} = (\zeta, 0, 0)$  with  $G_o(\mathbf{q}) = C_{4v}$ , and for the mirror planes  $(01\bar{1})$  and  $(001)$  with  $G_o(\mathbf{q}) = C_s$ . The eigenvectors and corresponding eigenvalues are collected in table 2.3. Along the

Table 2.3.

*Symmetry properties of phonons in an f.c.c. lattice*

$\mathbf{q}$	$G_o(\mathbf{q})$	$\underline{\xi}_j$	$M_{\omega_j}^2$	$\Gamma^\alpha$
$(\zeta, 0, 0)$	$C_{4v}$ table A.11	$(1, 0, 0)$ $(0, 1, 0)$ $(0, 0, 1)$ }	$D_{11}$ $D_{22}$	$\Delta_1$ $\Delta_5$
$(\zeta, \zeta, \zeta)$	$C_{3v}$ table A.13	$3^{-\frac{1}{2}}(1, 1, 1)$ $2^{-\frac{1}{2}}(1, \bar{1}, 0)$ $6^{-\frac{1}{2}}(1, 1, \bar{2})$ }	$D_{11} + 2D_{12}$ $D_{11} - D_{12}$	$\Lambda_1$ $\Lambda_3$
$(0, \zeta, \zeta)$	$C_{2v}$ table A.7	$2^{-\frac{1}{2}}(0, 1, 1)$ $(1, 0, 0)$ $2^{-\frac{1}{2}}(0, 1, \bar{1})$	$D_{22} + D_{23}$ $D_{11}$ $D_{22} - D_{23}$	$\Sigma_1$ $\Sigma_3$ $\Sigma_4$
$(\eta, \zeta, \zeta)$ $(01\bar{1})$ plane	$C_s$ table A.5	$2^{-\frac{1}{2}}(0, 1, \bar{1})$ $(a, 2^{-\frac{1}{2}}b, 2^{-\frac{1}{2}}b)$ $(\bar{b}, 2^{-\frac{1}{2}}a, 2^{-\frac{1}{2}}a)$	$D_{22} - D_{23}$ $D_{11} + cD_{12}$ $D_{22} + D_{23} - cD_{12}$	- + +
$(\eta, \zeta, 0)$ $(001)$ plane	$C_s$	$(0, 0, 1)$ $(a, b, 0)$ $(\bar{b}, a, 0)$	$D_{33}$ $D_{11} + dD_{12}$ $D_{22} - dD_{12}$	- + +

$$a^2 + b^2 = 1, \quad c = 2^{\frac{1}{2}}b/a, \quad d = b/a$$

three symmetry directions there are two transverse-phonon branches and one longitudinal-phonon branch. Phonons with  $\underline{q}$  in a mirror plane are polarized either perpendicular to this plane ( $\Gamma^\alpha = -$ ) or in the plane ( $\Gamma^\alpha = +$ ). The phonons belonging to the + branches are not purely longitudinal or transverse, and a and b in table 2.3 are functions of  $\underline{q}$ . Calculation of the dispersion relation along the directions  $\Delta, \Lambda$  and  $\Sigma$  from the dynamical matrix defined in tables 2.1 and 2.2, yields the result shown in figure 2.2.

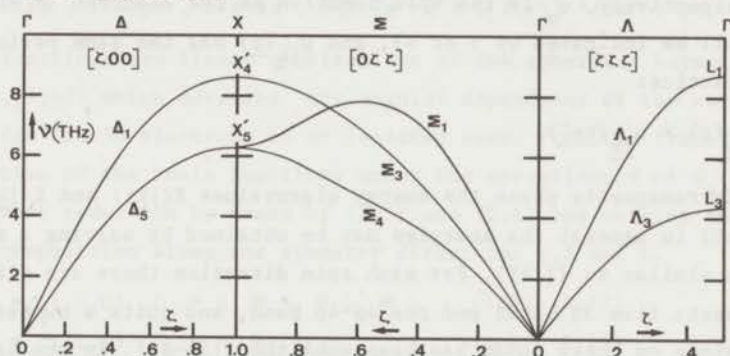


Figure 2.2.

Phonon dispersion relation  $v(\underline{q})$  in nickel along symmetry directions, calculated by means of the interatomic force constants determined by Birgeneau et al. [2]:

#### 2.4. Electrons

Next, we consider the itinerant electrons in the crystal lattice [24], which are in this case the electrons that originate from the atomic 3d, 4s and 4p states. If the spin-orbit coupling is neglected, the total Hamiltonian  $H_T$  for the electron system reads

$$H_T = \sum_i \left[ \frac{\underline{p}_i^2}{2m_e} + V(\underline{r}_i) \right] + \sum_{i \neq j} \frac{e^2}{|\underline{r}_i - \underline{r}_j|} = H_0 + H_c, \quad (2.27)$$

where  $m_e$  is the electron mass,  $\underline{p}_i$  and  $\underline{r}_i$  are the momentum operator and the position vector of the  $i$ -th electron. The first term  $H_0$  consists of the kinetic energy of the electrons and the periodic lattice potential  $V(\underline{r}_i)$  due to the ion cores, the second term  $H_c$  represents the energy resulting from the Coulomb interaction between the electrons. By means of the Hartree-Fock approximation one may obtain the following eigenvalue

equation for the energy of the one-electron states:

$$H_i \psi_i = E_i \psi_i. \quad (2.28)$$

According to Bloch's theorem, the functions  $\psi_i$  are of the form

$$\psi_i = \psi_{jk\sigma}(\underline{r}) = \exp(i\underline{k} \cdot \underline{r}) u_{jk}(\underline{r}) u_{\sigma}, \quad (2.29)$$

where  $j$ ,  $\underline{k}$  and  $\sigma$  denote the band index, wave vector\*) and spin direction, respectively,  $u_{\sigma}$  is the spin function of the electron ( $\sigma = \pm \frac{1}{2}$ , which will be indicated by  $\uparrow$  or  $\downarrow$ ), and  $u_{jk}(\underline{r})$  has the same periodicity as the lattice:

$$u_{jk}(\underline{r}) = u_{jk}(\underline{r} + \underline{l}).$$

In the ferromagnetic phase the energy eigenvalues  $E(j\underline{k}\uparrow)$  and  $E(j\underline{k}\downarrow)$  are different; in general the energies may be obtained by solving a matrix equation similar to (2.25). For each spin direction there are six bands of interest: five 3d bands and one 4s-4p band, and quite a number of computations on these bands has been published [45-51]. In the band structure calculated by Zornberg [48] the effect of spin-orbit coupling has been taken into account.

In connection with the selection rules for interaction between the electrons and the collective excitations it is of interest to establish the symmetry properties of the functions  $u_{jk}(\underline{r}) u_{\sigma}$ , in particular for the 3d bands. The one-electron Hamiltonian in (2.28) is invariant under the operations of the magnetic space group, and therefore the functions  $u_{jk}(\underline{r}) u_{\sigma}$  must transform as the irreducible representations of  $G_o^M(\underline{k})$ . The labelling of the electron states may be performed in three steps. First, we determine the functions  $u_{jk}(\underline{r})$  that transform as the irreducible, single-valued representations  $\Gamma_S^{\alpha}$  of  $G_o(\underline{k})$  (a). In the next step the spin-orbit coupling is introduced and the direct-product representations  $\Gamma_S^{\alpha} \otimes D_{\frac{1}{2}}$  are decomposed into double-valued representations (b).

-----  
\*) According to common practice, the wave vector of the electron will be denoted by  $\underline{k}$ . This should not cause confusion with the wave vector of the scattered neutrons, to be introduced in chapter III.



Finally the lower symmetry of the ferromagnetic state is taken into account by subducing the representations onto the proper magnetic point group (c).

(a) Paramagnetic phase, without spin-orbit coupling.

In the tight-binding approximation, the 5-dimensional representation  $\Gamma_S$  for the 3d bands is based on the functions

$$f(r)xy, f(r)yz, f(r)zx, f(r)(y^2-z^2), f(r)3^{-\frac{1}{2}}(3x^2-r^2).$$

These functions are linear combinations of the spherical harmonics  $Y_m^2$  ( $m = 0, \pm 1, \pm 2$ ) which describe the angular dependence of the wave functions for the 3d electrons in an isolated atom. From the transformation properties of the basis functions under the operations  $R$  of  $G_o(\underline{k})$  and subsequent reduction by means of (2.5) and (2.6) one obtains the following decomposition along the symmetry directions  $\Delta, \Lambda$  and  $\Sigma$ .

$$\begin{aligned} \underline{k} = (\zeta, 0, 0) \quad \Gamma_S &= \Delta_1 \oplus \Delta_2 \oplus \Delta_2' \oplus \Delta_5 & \text{(table A.11)} \\ \underline{k} = (\zeta, \zeta, \zeta) \quad \Gamma_S &= \Lambda_1 \oplus 2\Lambda_3 & \text{(table A.13)} \\ \underline{k} = (0, \zeta, \zeta) \quad \Gamma_S &= 2\Sigma_1 \oplus \Sigma_2 \oplus \Sigma_3 \oplus \Sigma_4 & \text{(table A. 7)} \end{aligned} \quad (2.30)$$

The bands  $\Delta_5$  and  $\Lambda_3$  are doubly degenerate, but become four-fold degenerate if the two possible spin states are taken into account. Also for the other, nondegenerate, bands a doubling of the degeneracy has to be introduced. To construct wave functions with the correct transformation properties, linear combinations of the basis functions must be chosen. The proper combinations listed in the first column of table 2.4 were taken from the tables given by Cornwell [24]. Figure 2.3 shows the electronic band structure in the paramagnetic state [48], for which case the decomposition scheme (2.30) holds.

(b) Paramagnetic phase, spin-orbit coupling included.

As has been mentioned earlier, the removal of band degeneracies by spin-orbit coupling is related to the reduction of  $\Gamma_S^\alpha \otimes D_{\frac{1}{2}}$  according to (2.16) and (2.17). The traces of the matrices  $D_{\frac{1}{2}}(R)$  for the operations of the point groups  $C_{4v}, C_{3v}$  and  $C_{2v}$  are given in table A.2, while the characters of the double-valued representations are listed in the lower part of the tables A.11, A.13 and A.7. For simplicity the operations  $\bar{R}$  have been omitted

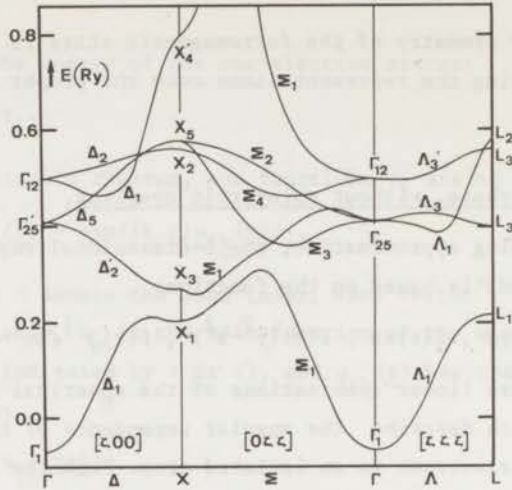


Figure 2.3.

Electronic band structure for the 3d and 4s-4p bands along  $\Delta, \Sigma$  and  $\Lambda$  for paramagnetic nickel [48] if spin-orbit coupling is neglected. In accordance with the selection rule (2.13) the 4s-4p branch hybridizes only with the  $\Delta_1, \Sigma_1$  and  $\Lambda_1$  branches of the 3d bands.

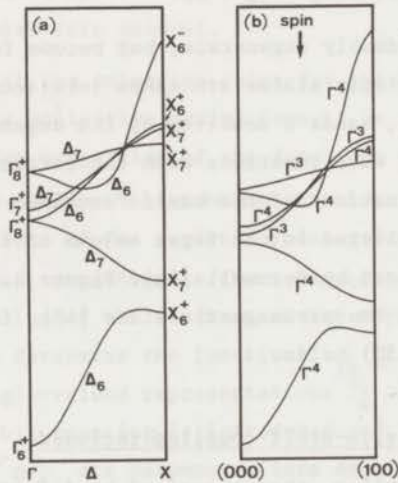


Figure 2.4.

Schematic electronic band structure in nickel along  $[100]$ , showing the band splitting permitted by symmetry if spin-orbit coupling is included.

(a) Paramagnetic phase,  $G_O(\underline{k}) = C_{4v}$ , character table A.11.

(b) Ferromagnetic phase,  $\underline{M} // [01\bar{1}]$ ,  $G_O^M(\underline{k}) = C_s$ , character table A.5.

For the corresponding + bands  $\Gamma^3$  and  $\Gamma^4$  should be exchanged.

The removal of accidental degeneracies at the crossing of branches with the same representation has not been shown.

from the tables, and when using the characters one should bear in mind that  $\chi(\bar{R}) = -\chi(R)$  for the double-valued representations. Application of (2.17) yields the following decomposition scheme

$$\begin{aligned} \Delta_1 \otimes D_{\frac{1}{2}} &= \Delta_6, \quad \Delta_2 \otimes D_{\frac{1}{2}} = \Delta_7, \quad \Delta_2' \otimes D_{\frac{1}{2}} = \Delta_7, \quad \Delta_5 \otimes D_{\frac{1}{2}} = \Delta_6 \oplus \Delta_7 \\ \Lambda_1 \otimes D_{\frac{1}{2}} &= \Lambda_6, \quad \Lambda_3 \otimes D_{\frac{1}{2}} = \Lambda_4 \oplus \Lambda_5 \oplus \Lambda_6 \\ \Sigma_i \otimes D_{\frac{1}{2}} &= \Sigma_5 \quad (i = 1, 2, 3, 4) \end{aligned} \quad (2.31)$$

The splitting of the bands is shown schematically in table 2.4. By means of criterion (2.18) it is found that  $\Delta_6$ ,  $\Delta_7$ ,  $\Lambda_6$  and  $\Sigma_5$  belong to case (c), and  $\Lambda_4$  and  $\Lambda_5$  to case (b). Hence, the  $\Lambda_4$  and  $\Lambda_5$  bands "stick together" as a result of time-reversal symmetry. The four-fold branches  $\Delta_5$  and  $\Lambda_3$  are split up into two double branches, whereas all other branches remain doubly degenerate. Since the quantization axis for the electron spins may be chosen arbitrarily, the matrices  $D_{\frac{1}{2}}(R)$  are not defined uniquely, and a determination of the wave functions with the proper transformation properties becomes quite complicated for the split  $\Delta_5$  and  $\Lambda_3$  bands, unless the quantization axis is chosen in a sensible way (e.g. parallel to  $\underline{k}$ ).

(c) Ferromagnetic phase, spin-orbit coupling included.

Next we take into account the reduction of the symmetry in the ferromagnetic state, which leads to a further splitting of the bands. As an example the magnetization direction is chosen along  $[01\bar{1}]$ , i.e. perpendicular to the wave vectors  $(\tau, 0, 0)$ ,  $(\tau, \tau, \tau)$  and  $(0, \tau, \tau)$ . For these  $\underline{k}$ 's the unitary elements in the magnetic point group  $M(\underline{k})$  are E and  $IC_{2e}$ , i.e.  $G_o(\underline{k}) = C_s$ . It is seen from the character table (table A.5) that the group  $C_s$  has only one-dimensional irreducible representations, which implies that all degeneracies are removed.

Subduction of the representations in (2.31) onto  $C_s$  gives:

$$\begin{aligned} \Delta_6 &\rightarrow \Gamma^3 \oplus \Gamma^4 & \Lambda_4 &\rightarrow \Gamma^3 & \Sigma_5 &\rightarrow \Gamma^3 \oplus \Gamma^4 \\ \Delta_7 &\rightarrow \Gamma^3 \oplus \Gamma^4 & \Lambda_5 &\rightarrow \Gamma^4 & & \\ & & \Lambda_6 &\rightarrow \Gamma^3 \oplus \Gamma^4 & & \end{aligned} \quad (2.32)$$

Since the notation of Bouckaert et al. refers to a purely cubic crystal, the irreducible representations in the ferromagnetic state will be indicated by  $\Gamma^\beta$ , where  $\beta$  corresponds to the row in the relevant character table.

Table 2.4.  
Representations of the 3d electron bands

paramagnetic <sup>a)</sup>			ferromagnetic, $\underline{M}/[01\bar{1}]^b$		
$u_{\underline{q}}(\underline{r})$	$\Gamma_S^\alpha$	$\Gamma_D^\beta$	$\Gamma_D^\beta(+)$	$\Gamma_D^\beta(+)$	$u_{\underline{q}}(\underline{r})$
$3^{-\frac{1}{2}}(3x^2-r^2)$	$\Delta_1$	$\Delta_6$	$\Gamma^3$	$\Gamma^4$	$3^{-\frac{1}{2}}(3x^2-r^2)$
$y^2-z^2$	$\Delta_2$	$\Delta_7$	$\Gamma^4$	$\Gamma^3$	$y^2-z^2$
$yz$	$\Delta'_2$	$\Delta_7$	$\Gamma^3$	$\Gamma^4$	$yz$
$xy$	$\Delta_5$ {	$\Delta_6$	$\Gamma^3$	$\Gamma^4$	$2^{-\frac{1}{2}}x(y+z)$
$xz$ }		$\Delta_7$	$\Gamma^4$	$\Gamma^3$	$2^{-\frac{1}{2}}x(y-z)$
$3^{-\frac{1}{2}}(xy+yz+zx)$	$\Lambda_1$	$\Lambda_6$	$\Gamma^3$	$\Gamma^4$	$yz; 2^{-\frac{1}{2}}x(y+z)$
$x^2-y^2$	$\Lambda_3$ {	$(\Lambda_4, \Lambda_5)$	$\Gamma^4$	$\Gamma^3$	$y^2-z^2$
$3^{-\frac{1}{2}}(3z^2-r^2)$ }		$\Lambda_6$	$\Gamma^3$	$\Gamma^4$	$3^{-\frac{1}{2}}(3x^2-r^2)$
$2^{-\frac{1}{2}}(yz-zx)$	$\Lambda_3$ {	$(\Lambda_4, \Lambda_5)$	$\Gamma^4$	$\Gamma^3$	$2^{-\frac{1}{2}}x(y-z)$
$6^{-\frac{1}{2}}(2xy-yz-zx)$ }		$\Lambda_6$	$\Gamma^3$	$\Gamma^4$	$yz; 2^{-\frac{1}{2}}x(y+z)$
$3^{-\frac{1}{2}}(3x^2-r^2)$	$\Sigma_1$	$\Sigma_5$	$\Gamma^3$	$\Gamma^4$	$3^{-\frac{1}{2}}(3x^2-r^2)$
$yz$	$\Sigma_1$	$\Sigma_5$	$\Gamma^3$	$\Gamma^4$	$yz$
$2^{-\frac{1}{2}}x(y-z)$	$\Sigma_2$	$\Sigma_5$	$\Gamma^4$	$\Gamma^3$	$2^{-\frac{1}{2}}x(y-z)$
$2^{-\frac{1}{2}}x(y+z)$	$\Sigma_3$	$\Sigma_5$	$\Gamma^3$	$\Gamma^4$	$2^{-\frac{1}{2}}x(y+z)$
$y^2-z^2$	$\Sigma_4$	$\Sigma_5$	$\Gamma^4$	$\Gamma^3$	$y^2-z^2$

<sup>a)</sup> See tables A.11, A.13 and A.7. The eigenfunctions  $u_{\underline{q}}(\underline{r})$  listed in the first column transform according to  $\Gamma_S^\alpha$ .

<sup>b)</sup> See table A.5.

The eigenfunctions transforming according to  $\Gamma^3$  and  $\Gamma^4$  are easily derived if one takes into account that the transformation properties of the spin functions, with the  $[01\bar{1}]$  direction as quantization axis, are defined by (see (2.14))

$$\begin{aligned} Eu_{\uparrow} &= u_{\uparrow}, \quad Eu_{\downarrow} = u_{\downarrow}, \quad IC_{2e}u_{\uparrow} = iu_{\uparrow}, \quad IC_{2e}u_{\downarrow} = -iu_{\downarrow} \\ \Gamma^3: & x(y+z)u_{\uparrow}, \quad x(y-z)u_{\downarrow}, \quad yzu_{\uparrow}, \quad (y^2-z^2)u_{\downarrow}, \quad 3^{-\frac{1}{2}}(3x^2-r^2)u_{\uparrow} \\ \Gamma^4: & x(y+z)u_{\downarrow}, \quad x(y-z)u_{\uparrow}, \quad yzu_{\downarrow}, \quad (y^2-z^2)u_{\uparrow}, \quad 3^{-\frac{1}{2}}(3x^2-r^2)u_{\downarrow} \end{aligned} \quad (2.33)$$

In table 2.4 the final splitting of the bands is given. It should be pointed out that there is no relation between the position of the bands in the table and the electron energies. Furthermore, the suggested one-to-one correspondence between wave functions and bands may be misleading. The wave functions belonging to, for example, a  $\Gamma^3$  band are linear combinations of the five 3d-like functions in (2.33) and those 4s, 4p-like functions that transform as  $\Gamma^3$ . The functions listed in the last column of table 2.4 should be interpreted as the dominant term in the wave function for a certain  $\underline{k}$ , and in this way the relation between the bands  $\Gamma_D^{\beta}$  in the ferromagnetic phase and the bands  $\Gamma_S^{\alpha}$  in the paramagnetic phase may be established. An example of the electronic band structure in both phases is shown in figure 2.4. for the  $[100]$  direction.

### 2.5. Electron-hole excitations and magnons

The theory of magnetic excitations in a ferromagnetic metal is based on the electronic band structure. A transition of an electron from the state  $|j\underline{k}\sigma\rangle$  to the state  $|j'\underline{k}'\sigma'\rangle$  is equivalent to the creation of an electron-hole excitation with wave vector  $\underline{q} = \underline{k}' - \underline{k}$ , energy  $\hbar\omega(\underline{q}) = E(j'\underline{k}'\sigma') - E(j\underline{k}\sigma)$  and spin  $\sigma' - \sigma$ . When electron-electron correlations are taken into account, collective excitations (magnons) may exist, which are linear combinations of electron-hole excitations with spin  $(\sigma' - \sigma) = 1$ . Theoretical treatments of the magnetic excitations in metals have been given both for single-band [52-54] and multiple-band systems [55-58].

A convenient method to describe the magnetic excitations is the occupation-number formalism. The electron transitions are expressed in terms of the Fermion operators  $c_{j\underline{k}\sigma}^+$  and  $c_{j\underline{k}\sigma}$ , which create and annihilate an

electron in state  $|j\underline{k}\sigma\rangle$ . The operators obey the anti-commutation rules ( $\{A,B\} = AB+BA$ )

$$\begin{aligned} \{c_{j\underline{k}\sigma}, c_{j',\underline{k}'\sigma'}^+\} &= \delta_{jj'} \delta_{\underline{k}\underline{k}'} \delta_{\sigma\sigma'} \\ \{c_{j\underline{k}\sigma}, c_{j',\underline{k}'\sigma'}\} &= 0 \\ \{c_{j\underline{k}\sigma}^+, c_{j',\underline{k}'\sigma'}^+\} &= 0 \end{aligned} \quad (2.34)$$

A repeated application of  $c_{j\underline{k}\sigma}^+$  yields a zero result:  $\left\{c_{j\underline{k}\sigma}^+\right\}^2 = \frac{1}{2}\{c_{j\underline{k}\sigma}^+, c_{j\underline{k}\sigma}^+\} = 0$ , and consequently the number of electrons in each state is 0 or 1.

Below, a short review of the theory for a single-band model will be presented, which is actually based on a summary given by Walker [59].

Expressed in Fermion operators, the Hamiltonian (2.27) for a single band becomes

$$H = \sum_{\underline{k}\sigma} \epsilon(\underline{k}) c_{\underline{k}\sigma}^+ c_{\underline{k}\sigma} + \frac{1}{2} \sum_{\underline{q}} \sum_{\underline{k}, \underline{k}'} V(\underline{q}') c_{\underline{k}+\underline{q}, \sigma}^+ c_{\underline{k}, -\underline{q}, \sigma'}^+ c_{\underline{k}, \sigma} c_{\underline{k}', \sigma'} \quad (2.35)$$

$\epsilon(\underline{k})$  is the energy of the Bloch eigenstate of  $H_0$  with wave vector  $\underline{k}$ . The matrix element  $\langle \underline{k}+\underline{q}, \sigma, \underline{k}, -\underline{q}, \sigma' | H_c | \underline{k}, \sigma, \underline{k}', \sigma' \rangle$ , which depends in fact on the vectors  $\underline{k}$ ,  $\underline{k}'$  and  $\underline{q}'$  (cf. [54]), has been approximated by  $V(\underline{q}')$ .

In the ground state the majority of the electrons is supposed to be in  $\downarrow$  states. The spin raising operator  $S_{\underline{k}}^+(\underline{q})$  is defined by

$$S_{\underline{k}}^+(\underline{q}) = c_{\underline{k}+\underline{q}, \uparrow}^+ c_{\underline{k}, \downarrow}^+ \quad (2.36)$$

and creates an electron-hole excitation by inducing a transition from a  $\downarrow$  state to a  $\uparrow$  state. The energies of these Stoner excitations are derived from the equation of motion

$$i\hbar \frac{d}{dt} S_{\underline{k}}^+(\underline{q}) = [S_{\underline{k}}^+(\underline{q}), H]. \quad (2.37)$$

From the equations (2.34), (2.35), (2.36) and (2.37) one obtains the following linearized equation for  $S_{\underline{k}}^+(\underline{q})$ , where  $n_r$  denotes  $c_r^+ c_r$ :

$$\begin{aligned} i\hbar \frac{d}{dt} S_{\underline{k}}^+(\underline{q}) &= \{\epsilon(\underline{k}) - \epsilon(\underline{k}+\underline{q})\} S_{\underline{k}}^+(\underline{q}) + \\ &\sum_{\underline{q}'} V(\underline{q}') (n_{\underline{k}+\underline{q}+\underline{q}', \uparrow} - n_{\underline{k}+\underline{q}, \downarrow}) S_{\underline{k}}^+(\underline{q}) + \\ &(n_{\underline{k}, \uparrow} - n_{\underline{k}+\underline{q}, \downarrow}) \sum_{\underline{q}'} V(\underline{q}') S_{\underline{k}+\underline{q}}^+(\underline{q}). \end{aligned} \quad (2.38)$$

After the introduction of renormalized energies  $E(\underline{k}\sigma)$

$$E(\underline{k}\sigma) = \epsilon(\underline{k}) - \sum_{\underline{q}'} V(\underline{q}') n_{\underline{k}+\underline{q}',\sigma}$$

(2.38) may be written as

$$i\hbar \frac{d}{dt} S_{\underline{k}}^+(\underline{q}) = \{E(\underline{k}+) - E(\underline{k}+\underline{q}+)\} S_{\underline{k}}^+(\underline{q}) + (n_{\underline{k}+} - n_{\underline{k}+\underline{q}+}) \sum_{\underline{q}'} V(\underline{q}') S_{\underline{k}+\underline{q}}^+(\underline{q}), \quad (2.39)$$

where  $S_{\underline{k}}^+(\underline{q})$  contains the factor  $\exp\{i\omega(\underline{q})t\}$ .

At this stage one may continue in two different ways. If the last term in the right-hand side of (2.39), which describes the interaction between Stoner excitations, may be neglected, the excitation created by  $S_{\underline{k}}^+(\underline{q})$  is stable and has the energy

$$\hbar\omega(\underline{q}) = E(\underline{k}+\underline{q}+) - E(\underline{k}+). \quad (2.40)$$

Inclusion of the interaction term leads to a change in energy and a finite lifetime of the excitations. For a specific  $\underline{q}$  the energy (2.40) is a function of  $\underline{k}$ ; therefore the Stoner excitations occupy a continuum in  $(\omega, \underline{q})$  space, the boundaries of which are determined by the shape of the  $\uparrow$  and  $\downarrow$  band (cf. figure 2.5). Owing to the interaction term, there are solutions of (2.39) that correspond to collective excitations. Changing from individual spin raising operators  $S_{\underline{k}}^+(\underline{q})$  to the operator  $\sum_{\underline{k}} A_{\underline{k}} S_{\underline{k}}^+(\underline{q})$  yields the following integral equation for the  $A_{\underline{k}}$ 's

$$\{E(\underline{k}+\underline{q}+) - E(\underline{k}+) - \hbar\omega(\underline{q})\} A_{\underline{k}} = \sum_{\underline{q}'} \left[ V(\underline{q}') (n_{\underline{k}-\underline{q}'+} - n_{\underline{k}+\underline{q}-\underline{q}'+}) A_{\underline{k}-\underline{q}'} \right]. \quad (2.41)$$

The eigenvalues  $\hbar\omega(\underline{q})$  are found from

$$1 + V(\underline{q}) \sum_{\underline{k}} \frac{n_{\underline{k}+\underline{q}+} - n_{\underline{k}+}}{E(\underline{k}+\underline{q}+) - E(\underline{k}+) - \hbar\omega(\underline{q})} = 0 \quad (2.42)$$

and it can be shown that there exists a magnon-like solution  $\hbar\omega(\underline{q})$  of (2.42) which is quadratic for small values of  $\underline{q}$

$$\hbar\omega(\underline{q}) = Dq^2 + O(q^4). \quad (2.43)$$

The constant  $D$  is related to the electronic band structure [60].

Figure 2.5 shows some results of a calculation on magnetic excitations in nickel by Thompson and Myers [61].

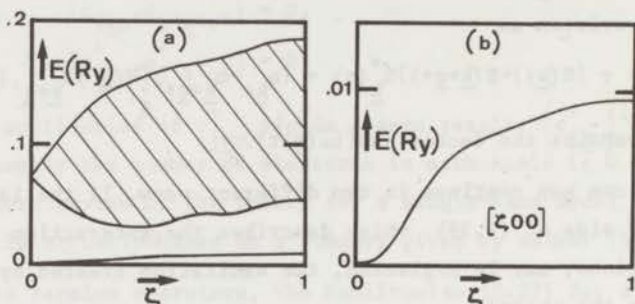


Figure 2.5.

Magnetic excitations in nickel along  $[100]$  [61].

(a) Continuum of Stoner excitations and magnon dispersion relation for a single-band model.

(b) Magnon dispersion relation on enlarged scale (0.01 Ry corresponds to  $\nu = 32.9$  THz).



## CHAPTER III

### THEORY OF THERMAL NEUTRON SCATTERING IN FERROMAGNETIC NICKEL

#### 3.1. Introduction

In the present chapter the two dominant interactions between the neutron and the scattering sample will be discussed. These are, first, the strong interaction between the neutron and the atomic nuclei and, secondly, the electromagnetic interaction between the magnetic moments of the neutron and the electrons. In general there exists also an interaction between the magnetic moments of the neutron and the nuclei, but this interaction is negligible, certainly for nickel, because the three dominant stable isotopes  $^{58}\text{Ni}$ ,  $^{60}\text{Ni}$  and  $^{62}\text{Ni}$  have a nuclear spin equal to zero (cf. table 3.1). There are actually still two other electromagnetic interactions, viz. the interaction due to the movement of the neutron in the electrostatic field of the nuclei [62] and the relativistic neutron-electron interaction [63], but these may be neglected in comparison with the two main interactions mentioned above.

The theory of thermal neutron scattering has been extensively reviewed in the literature [64-66], and in this chapter only a brief summary will be given of the theory relevant to a ferromagnetic metal. In section 3.2. the basic cross section formulae will be discussed. The derivation of the elastic and inelastic cross sections is sketched in sections 3.3. and 3.4, respectively. In the presentation of the inelastic scattering theory we consider processes that involve one of the elementary excitations introduced in the previous chapter.

#### 3.2. Nuclear and magnetic scattering

If the interaction between the neutron and the specimen can be described by a potential  $V(\mathbf{r})$ , the scattering cross section can be calculated as follows. The state of the incident neutron will be defined by its wave vector  $\underline{k}_0$  and its spin quantum number  $s_0$ , the state of the scattered neutron correspondingly by  $\underline{k}$  and  $s$ . In the first Born approximation the differential cross section for scattering into the solid-angle element  $d\Omega$  is given by [67]:

$$\frac{d\sigma}{d\Omega} = \frac{k}{k_0} \left( \frac{m_n}{2\pi\hbar^2} \right)^2 |\langle A_s k | V(\underline{r}) | A_0 s_0 k_0 \rangle|^2 =$$

$$\frac{k}{k_0} \left( \frac{m_n}{2\pi\hbar^2} \right)^2 |\langle A_s | \int d\underline{r} \exp(i\underline{Q} \cdot \underline{r}) V(\underline{r}) | A_0 s_0 \rangle|^2, \quad (3.1)$$

where  $A_0$  and  $A$  denote the complete sets of quantum numbers that characterize the initial and final state of the scattering specimen,  $\underline{Q} = \underline{k}_0 - \underline{k}$  is the neutron scattering vector and  $m_n$  the neutron mass. For a comparison with experiment it is necessary to average (3.1) over all possible initial states  $|A_0 s_0\rangle$ , each weighted according to its probability  $P(A_0)P(s_0)$ , and to sum over all final states  $|A_s\rangle$  that are allowed by the conservation law for the total energy:

$$E(A) - E(A_0) = \frac{\hbar^2}{2m_n} (k_0^2 - k^2) = \hbar\omega.$$

Here  $E(A_0)$  and  $E(A)$  denote the energy of the specimen before and after scattering and  $\hbar\omega$  the energy loss of the neutron. Energy conservation is taken into account by including the following delta function, expressed in integral representation, in the summation over the final states:

$$\delta[E(A) - E(A_0) - \hbar\omega] = \frac{1}{2\pi\hbar} \int_{-\infty}^{+\infty} dt \exp\left[ it \left\{ \frac{E(A) - E(A_0)}{\hbar} - \omega \right\} \right].$$

In (3.1),  $V(\underline{r})$  should be regarded as an operator and is expressed in Heisenberg representation  $V(\underline{r}, t)$  according to the definition

$$O(\underline{r}, t) = \exp\left(\frac{iHt}{\hbar}\right) O(\underline{r}) \exp\left(\frac{-iHt}{\hbar}\right),$$

where  $H$  is the Hamiltonian of the scattering system and  $O(\underline{r})$  any operator acting on the system. After substitution in (3.1) one obtains the following expression for the double differential cross section

$$\frac{d^2\sigma}{d\Omega dE} = \frac{k}{k_0} \left( \frac{m_n}{2\pi\hbar^2} \right)^2 \frac{1}{2\pi\hbar} \int_{-\infty}^{+\infty} dt \exp(-i\omega t) \times$$

$$\langle \int d\underline{r} \int d\underline{r}' \exp(-i\underline{Q} \cdot \underline{r}) V^*(\underline{r}, 0) V(\underline{r}', t) \exp(i\underline{Q} \cdot \underline{r}') \rangle_T, \quad (3.2)$$

where  $E$  denotes the energy of the scattered neutron. The integrations are over the volume of the specimen and  $\langle \dots \rangle_T$  stands for  $\sum P(A_0)P(s_0) \langle A_0 s_0 | \dots | A_0 s_0 \rangle$ . Before the latter summation can be performed, the properties of the

scattering system and the explicit form of  $V(\underline{r})$  must be specified.

To treat the nuclear scattering by a lattice of  $N$  nuclei with spin zero at positions  $\underline{R}_Z$ , the interaction potential  $V_n(\underline{r})$  is usually approximated by the Fermi pseudo-potential

$$V_n(\underline{r}) = \frac{2\pi\hbar^2}{m_n} \sum_Z b_Z \delta(\underline{r}-\underline{R}_Z), \quad (3.3)$$

where the short-range potential of the nucleus is described by a delta function. The scattering length  $b_Z$ , as defined in (3.3), may be complex and has different values for the various isotopes of a particular element (cf. table 3.1). The imaginary part of  $b_Z$  is only important for nuclei with a large absorption cross section, and may be neglected for the Ni isotopes. After substitution of (3.3) into (3.2) and integration over  $\underline{r}$  and  $\underline{r}'$  one obtains for the scattering cross section

$$\frac{d^2\sigma_n}{d\Omega dE} = \frac{k}{k_0} \frac{1}{2\pi\hbar} \int_{-\infty}^{+\infty} dt \exp(-i\omega t) \times \langle \sum_{ZZ'} b_Z^* b_{Z'} \exp(-i\mathbf{Q}\cdot\underline{R}_Z(0)) \exp(i\mathbf{Q}\cdot\underline{R}_{Z'}(t)) \rangle_T. \quad (3.4)$$

Table 3.1.

Nuclear scattering lengths of nickel isotopes |71|\*

Isotope	$b(10^{-12} \text{ cm})$	abundance(%)	spin
$^{58}\text{Ni}$	1.47	67.8	0
$^{60}\text{Ni}$	0.28	26.2	0
$^{61}\text{Ni}$	?	1.2	3/2
$^{62}\text{Ni}$	-0.85	3.7	0
$^{64}\text{Ni}$	?	1.1	0

\* ) For natural nickel one has:

$$\langle b \rangle = 1.03 \times 10^{-12} \text{ cm}$$

$$\langle b \rangle^2 = 1.06 \times 10^{-24} \text{ cm}^2$$

$$\langle b^2 \rangle = 1.43 \times 10^{-24} \text{ cm}^2$$

The calculation of the magnetic scattering proceeds in a similar way, by substituting for the magnetic interaction potential  $V_m(\mathbf{r})$  the energy of the magnetic moment  $\underline{\mu}$  of the neutron in the magnetic field  $\underline{H}$  generated by the electrons. For a single electron with spin  $\underline{\sigma}$  and velocity  $\underline{v}$  the field  $\underline{H}(\mathbf{r})$  at a distance  $\underline{r}$  from the electron position is equal to [66]

$$\underline{H}(\mathbf{r}) = -2\mu_B \text{curl} \left[ \frac{\underline{\sigma} \times \underline{r}}{|\underline{r}|^3} \right] - \frac{e}{c} \frac{\underline{v} \times \underline{r}}{|\underline{r}|^3},$$

where  $\mu_B$  is the Bohr magneton,  $-e$  the electron charge and  $c$  the light velocity. The magnetic moment of the neutron may be expressed in units of the nuclear magneton  $\mu_N$  by

$$\underline{\mu} = 2\gamma\mu_N \underline{s}, \quad \gamma = -1.913.$$

Hence the magnetic interaction potential becomes

$$V_m(\mathbf{r}) = -\underline{\mu} \cdot \underline{H}(\mathbf{r}) = 2\gamma\mu_N \left[ 2\mu_B \underline{s} \cdot \text{curl} \left[ \frac{\underline{\sigma} \times \underline{r}}{|\underline{r}|^3} \right] + \frac{e}{c} \frac{\underline{s} \cdot \underline{v} \times \underline{r}}{|\underline{r}|^3} \right], \quad (3.5)$$

where the first term in the right-hand side represents the dipole-dipole interaction between the spins  $\underline{s}$  and  $\underline{\sigma}$ , and the second term the interaction between  $\underline{s}$  and the orbital magnetic moment of the electron.

In the description of the scattering by the 3d electrons in nickel the last term in (3.5) may be neglected in first approximation, because the net magnetic moment is for 91% due to the electron spins [68]. To account for the itinerant character of the unpaired electrons the spin-density distribution  $\underline{S}(\mathbf{r})$  is introduced by means of the Fermion operators (cf. (2.34)) and electron eigenfunctions (2.29)

$$\underline{S}(\mathbf{r}) = \sum_{\underline{k}\underline{k}'} \sum_{\underline{j}\underline{j}'} \sum_{\sigma\sigma'} \Psi_{\underline{j}\underline{k}\sigma}^*(\mathbf{r}) c_{\underline{j}\underline{k}\sigma}^+ c_{\underline{j}'\underline{k}'\sigma'}(\mathbf{r}) c_{\underline{j}'\underline{k}'\sigma'} \quad (3.6)$$

Without going through the complete derivation, which can be found in textbooks [65,66], we give the final result obtained from the general expression (3.2) for the magnetic scattering cross section for unpolarized neutrons

$$\frac{d^2\sigma_m}{d\Omega dE} = \frac{k}{k_0} \left( \frac{\gamma e^2}{m_e c^2} \right)^2 \frac{1}{2\pi\hbar} \int_{-\infty}^{+\infty} dt \exp(-i\omega t) \sum_{\alpha\beta} (\delta_{\alpha\beta} - e^\alpha e^\beta) \times \\ \langle \int d\underline{r} \int d\underline{r}' S^\alpha(\underline{r}, 0) \exp\{-i\underline{Q} \cdot \underline{r}(0)\} \exp\{i\underline{Q} \cdot \underline{r}'(t)\} S^\beta(\underline{r}', t) \rangle_T \quad (3.7)$$

Here  $\underline{e} = \underline{Q}/|Q|$  is the unit scattering vector, and  $\alpha$  and  $\beta$  denote the Cartesian coordinate directions. Since the spin density distribution in nickel is concentrated in the vicinity of the lattice sites  $|69,70|$ , one may assign an effective spin  $\underline{S}_L$  to the atom at position  $\underline{R}_L$  and introduce a magnetic form factor  $F_L(Q)$

$$\underline{S}_L = \int d\underline{r} \underline{S}(\underline{r}) \quad (3.8a)$$

$$\underline{S}_L F_L(Q) = \int d\underline{r} \underline{S}(\underline{r}) \exp\{-i\underline{Q} \cdot (\underline{r} - \underline{R}_L)\} \quad (3.8b)$$

The integrations in (3.8) are over the primitive unit cell, which contains only one atom. Substitution in (3.7) yields

$$\frac{d^2\sigma_m}{d\Omega dE} = \frac{k}{k_0} \left[ \frac{\gamma e^2}{m c^2} \right]^2 \frac{1}{2\pi\hbar} \int_{-\infty}^{+\infty} dt \exp(-i\omega t) \sum_{\alpha\beta} (\delta_{\alpha\beta} - e^\alpha e^\beta) \times \\ \langle \sum_{L'} F_L(Q) F_L(Q) S_L^\alpha(0) \exp\{-i\underline{Q} \cdot \underline{R}_L(0)\} \exp\{i\underline{Q} \cdot \underline{R}_L(t)\} S_L^\beta(t) \rangle_T \quad (3.9)$$

(3.4) and (3.9) are the basic expressions from which the nuclear and magnetic scattering cross sections will be derived below. Some characteristic differences between these two formulae may be noted:

- (a) The appearance of the form factor  $F_L(Q)$  in (3.9), which is related to the fact that the dimension of the spin density cloud around  $\underline{R}_L$  is of the same order of magnitude as the neutron wave length. On the other hand, the dimension of the nucleus is much smaller than the neutron wave length. Consequently the magnetic scattering is a decreasing function of  $|Q|$ , whereas the nuclear scattering is independent of the scattering vector.
- (b) Nuclear scattering depends on the correlation between the positions  $\underline{R}_L(0)$  and  $\underline{R}_L(t)$ , whereas magnetic scattering is related to fourfold correlations between spin components and position vectors. In the latter case the spin-spin and position-position correlations may be separated provided there is no spin-lattice interaction.
- (c) Magnetic scattering depends on the relative orientation of the electron spins (i.e. the magnetization direction) and the scattering vector, which provides a means to distinguish experimentally between magnetic and nuclear scattering.

### 3.3. Elastic scattering

For the calculation of the elastic and inelastic nuclear cross section equation (3.4) serves as starting point. The position vector  $\underline{R}_L(t)$  is decomposed as in (2.19), where the displacement  $\underline{u}_L(t)$  is given by (2.21). Since there is no correlation between the isotopes and the lattice sites the factor  $\langle \dots \rangle_T$  in (3.4) may be written as

$$\sum_{\underline{L}'} \sum_{\underline{L}} \langle b_{\underline{L}}^* b_{\underline{L}'} \rangle \exp\{i\underline{Q} \cdot (\underline{L}' - \underline{L})\} \langle \exp\{-i\underline{Q} \cdot \underline{u}_L(0)\} \exp\{i\underline{Q} \cdot \underline{u}_L(t)\} \rangle_T \quad (3.10)$$

Further simplification is possible by applying the following identities

- (a)  $\langle \exp(A) \rangle = \exp\{\frac{1}{2} \langle A^2 \rangle\}$  (see ref. [72])  
 (b)  $\langle \exp(A) \exp(B) \rangle = \exp\{\frac{1}{2} \langle (AB - BA) \rangle\} \langle \exp(A+B) \rangle$  (see ref. [73])

(a) holds if the operator A is a linear combination of the Bose operators a and  $a^+$ , while (b) holds if  $[A, B] = AB - BA$  is a number. Both conditions are fulfilled for the operators  $A = -i\underline{Q} \cdot \underline{u}_L(0)$  and  $B = i\underline{Q} \cdot \underline{u}_L(t)$ \*, and combination of (a) and (b) yields

$$\langle \exp(A) \exp(B) \rangle = \exp\{\frac{1}{2} \langle A^2 + B^2 + 2AB \rangle\}$$

Hence the correlation function in (3.10) becomes

$$\langle \exp\{-i\underline{Q} \cdot \underline{u}_L(0)\} \exp\{i\underline{Q} \cdot \underline{u}_L(t)\} \rangle_T = \exp\{-2W(\underline{Q})\} \exp[\langle \{ \underline{Q} \cdot \underline{u}_L(0) \} \{ \underline{Q} \cdot \underline{u}_L(t) \} \rangle_T]. \quad (3.11)$$

The factor  $\exp\{-2W(\underline{Q})\}$  is the Debye-Waller factor, where  $W(\underline{Q})$  is defined as

$$W(\underline{Q}) = \frac{1}{2} \langle \{ \underline{Q} \cdot \underline{u}_L(0) \}^2 \rangle_T$$

Next, (3.11) and (3.10) are substituted in (3.4), which yields

$$\frac{d^2 \sigma_n}{d\Omega dE} = \frac{k}{k_0} \frac{1}{2\pi\hbar} \int_{-\infty}^{+\infty} dt \exp(-i\omega t) \exp\{-2W(\underline{Q})\} \times \sum_{\underline{L}'} \sum_{\underline{L}} \langle b_{\underline{L}}^* b_{\underline{L}'} \rangle \exp\{i\underline{Q} \cdot (\underline{L}' - \underline{L})\} \exp[\langle \{ \underline{Q} \cdot \underline{u}_L(0) \} \{ \underline{Q} \cdot \underline{u}_L(t) \} \rangle_T] \quad (3.12)$$

\* According to (3.26)  $\underline{u}_L(t)$  is a linear function of the Bose operators  $a_j^+(\underline{q})$  and  $a_j(\underline{q})$ , and  $[A, B]$  may be expressed in the commutators (3.24).

The last exponential function in (3.12) may be expanded in a power series, in which the successive terms correspond to the partial cross sections for zero-phonon, one-phonon, ... scattering. Thus the elastic nuclear scattering cross section is given by

$$\left(\frac{d\sigma}{d\Omega}\right)_{el} = \exp\{-2W(Q)\} \sum_{\underline{l}} \sum_{\underline{l}'} \langle b_{\underline{l}}^* b_{\underline{l}'} \rangle \exp\{i\underline{Q} \cdot (\underline{l}' - \underline{l})\}. \quad (3.13)$$

Neglecting the imaginary part of the scattering lengths, one may rewrite  $\langle b_{\underline{l}} b_{\underline{l}'} \rangle$  as

$$\langle b_{\underline{l}} b_{\underline{l}'} \rangle = \langle b \rangle^2 + \delta_{\underline{l}\underline{l}'} (\langle b^2 \rangle - \langle b \rangle^2), \quad (3.14)$$

because the isotopes are distributed at random over the lattice.

The cross section (3.13) may accordingly be separated in a coherent and an incoherent part:

$$\left(\frac{d\sigma}{d\Omega}\right)_{coh}^{el} = \exp(-2W) \langle b \rangle^2 \left[ \sum_{\underline{l}} \exp(i\underline{Q} \cdot \underline{l}) \right]^2 \quad (3.15)$$

$$\left(\frac{d\sigma}{d\Omega}\right)_{inc}^{el} = \exp(-2W) N (\langle b^2 \rangle - \langle b \rangle^2) \quad (3.16)$$

The coherent scattering leads to Bragg reflections, which are due to the interference between the waves scattered from different nuclei. In a single crystal the partial waves are only in phase if  $\underline{Q}$  is equal to a reciprocal lattice vector  $\underline{\tau}$ , in which case (3.15) becomes

$$\left(\frac{d\sigma}{d\Omega}\right)_{coh}^{el} = N \frac{(2\pi)^3}{v_0} \langle b \rangle^2 \exp(-2W) \sum_{\underline{\tau}} \delta(\underline{Q} - \underline{\tau}), \quad (3.17)$$

where  $v_0$  is the volume of the unit cell of the crystal. The incoherent scattering, on the other hand, is isotropic and is (for Ni) due to the random distribution of the isotopes. For a general scatterer the disorder in nuclear spin orientation gives rise to an additional contribution to the incoherent cross section.

The elastic magnetic cross section may be derived in a similar way from the time-independent part of the spin-spin correlation function in (3.9). If the z-axis is taken as magnetization direction, the expectation values  $\langle S_{\underline{l}}^x \rangle_T$  and  $\langle S_{\underline{l}}^y \rangle_T$  are zero. Furthermore, it will be assumed that there is no spin-lattice

interaction, which implies that the spin-spin correlations may be separated from the position-position correlations. Hence the elastic magnetic cross section becomes

$$\left(\frac{d\sigma_m}{d\Omega}\right)^{el} = \left(\frac{\gamma e^2}{m_e c^2}\right)^2 \{1 - (e^z)^2\} F^2(Q) \langle S^z \rangle_T^2 \times \langle \sum_{\underline{L}} \sum_{\underline{L}'} \exp\{-i\underline{Q} \cdot \underline{R}_{\underline{L}}\} \exp\{i\underline{Q} \cdot \underline{R}_{\underline{L}'}\} \rangle_T, \quad (3.18)$$

as all atoms have the same effective spin and form factor. The position-position correlation function in (3.18) may be rewritten as follows

$$\langle \dots \rangle_T = \exp(-2W) \sum_{\underline{L}} \sum_{\underline{L}'} \exp\{i\underline{Q} \cdot (\underline{L}' - \underline{L})\} = N \frac{(2\pi)^3}{v_0} \exp(-2W) \sum_{\underline{I}} \delta(\underline{Q} - \underline{I})$$

and the final expression for the scattering cross section for unpolarized neutrons becomes

$$\left(\frac{d\sigma_m}{d\Omega}\right)^{el} = N \frac{(2\pi)^3}{v_0} \left(\frac{\gamma e^2}{m_e c^2}\right)^2 \{1 - (\underline{e} \cdot \underline{m})^2\} F^2(Q) \langle S^z \rangle_T^2 \exp(-2W) \sum_{\underline{I}} \delta(\underline{Q} - \underline{I}), \quad (3.19)$$

where  $e^z$  has been written as  $\underline{e} \cdot \underline{m}$ ,  $\underline{m}$  being the unit vector in the direction of the magnetization.

Hence the coherent Bragg reflection corresponding to a particular  $\underline{I}$  is the sum of a magnetic and a nuclear contribution in the ratio

$$\left(\frac{\gamma e^2}{m_e c^2}\right)^2 \{1 - (\underline{e} \cdot \underline{m})^2\} F^2(Q) \langle S^z \rangle_T^2 / \langle b \rangle^2.$$

For the integrated cross section for a particular Bragg reflection one obtains from (3.17) and (3.19)

$$\sigma_{n,coh} = N \langle b \rangle^2 \exp(-2W); \quad (3.20)$$

$$\sigma_m = N \left(\frac{\gamma e^2}{m_e c^2}\right)^2 \{1 - (\underline{e} \cdot \underline{m})^2\} F^2(Q) \langle S^z \rangle_T^2 \exp(-2W). \quad (3.21)$$

Some values for  $\sigma_m$  and  $\sigma_{n,coh}$  for nickel are listed in table 3.2. For the tabulated reflections  $\sigma_m$  amounts to at most 1% of  $\sigma_{n,coh}$  and decreases rapidly as function of  $Q$ . The elastic magnetic scattering is suppressed completely if the spins are oriented along the scattering vector ( $\underline{e} \cdot \underline{m} = 1$ ).



For a multidomain crystal with randomly oriented domains one should use  $\langle (\underline{e} \cdot \underline{m})^2 \rangle = 1/3$ . Furthermore, it may be seen from table 3.2 that the Debye-Waller factor  $\exp(-2W)$  leads to a reduction of the scattering cross sections for increasing scattering vector.

The observed incoherent scattering depends on the experimental set-up. If the detector surface, as seen from the specimen position, spans a solid angle  $\Omega$ , the incoherent scattering into this angle is proportional to  $\Omega$  according to (3.16) with  $\langle b^2 \rangle - \langle b \rangle^2 = 0.37$  barn for natural Ni (cf. table 3.1, 1 barn =  $10^{-24}$  cm<sup>2</sup>).

Table 3.2.

Elastic scattering cross sections for natural Ni.

$Q$	$ Q $ (Å <sup>-1</sup> )	$F(Q)^a$	$\exp(-2W)^b$	$\sigma_m$ ( $10^{-27}$ cm <sup>2</sup> ) <sup>c</sup>	$\sigma_n$ ( $10^{-27}$ cm <sup>2</sup> ) <sup>d</sup>
(1,1,1)	3.088	0.793(9)	0.952	9.58 ± 0.22	1010 ± 19
(2,0,0)	3.566	0.703(8)	0.936	7.41 ± 0.17	994 ± 19
(2,2,0)	5.043	0.447(5)	0.877	2.80 ± 0.06	930 ± 18
(4,0,0)	7.132	0.157(3)	0.769	0.31 ± 0.01	816 ± 15

<sup>a</sup>) ref. [70], uncertainties are given in parentheses in units of the last decimal.

<sup>b</sup>) calculated for  $T = 295$  K and a Debye temperature  $\Theta_D = 385$  K [2];  $2W = 51.62 \times 10^{-20} Q^2$  ( $Q$  in cm<sup>-1</sup>).

<sup>c</sup>) (3.21) with  $N = 1$ ,  $\langle S^z \rangle_T = 0.287$  [74],  $\{1 - (\underline{e} \cdot \underline{m})^2\} = 2/3$ .

<sup>d</sup>) (3.20) with  $N = 1$ ,  $\langle b \rangle = (1.03 \pm 0.01) \times 10^{-12}$  cm [71].

### 3.4. Inelastic scattering

Inelastic neutron scattering may be described in terms of creation or annihilation of elementary excitations in the scattering system, processes in which transfer of energy, momentum and angular momentum takes place between the neutron and the scatterer. The cross sections may accordingly be expressed in terms of expectation values for products of creation and annihilation operators, which will be discussed in section 3.4.1 for the phonons. A short description of the creation operators for Stoner excitations and magnons has been given in section 2.5.

The cross sections for energy gain and energy loss scattering are related to each other by the so-called detailed-balance condition. It can be shown that the energy transfer  $\hbar\omega$  between a neutron and a scattering sample at temperature  $T$  is governed by

$$\left(\frac{d^2\sigma}{d\Omega dE}\right)_{\underline{k}\rightarrow\underline{k}_0} = \frac{k^2}{k_0^2} \exp\left(\frac{\hbar\omega}{k_B T}\right) \left(\frac{d^2\sigma}{d\Omega dE}\right)_{\underline{k}\rightarrow\underline{k}_0} \quad (3.22)$$

if the following conditions are fulfilled:

- (a) The scattering system is in thermal equilibrium, which implies that the probability of the initial state  $|i\rangle = |A_0 s_{\underline{k}_0}\rangle$  is proportional to  $\exp(-E_i/k_B T)$ , where  $k_B$  is Boltzmann's constant.
- (b) The scattering process is reversible, i.e. the matrix element in (3.1) has the property  $\langle f|V(\underline{r})|i\rangle = \langle i|V(\underline{r})|f\rangle$ , where  $|f\rangle$  is the final state  $|A s_{\underline{k}}\rangle$ .

### 3.4.1. One-phonon scattering

For a proper description of the scattering of neutrons by lattice vibrations one has to use a quantum-mechanical approach [66]. In the occupation number representation the eigenstates of the vibrating lattice are defined by  $3N$  numbers  $n_j(\underline{q})$  which denote the number of phonons in the normal modes  $(j, \underline{q})$ . The effect of the phonon creation and annihilation operators  $a_j^+(\underline{q})$  and  $a_j(\underline{q})$  on the eigenstate  $|\dots, n_j(\underline{q}), \dots\rangle$  is defined by

$$\begin{aligned} a_j^+(\underline{q}) |\dots, n_j(\underline{q}), \dots\rangle &= \{n_j(\underline{q})+1\}^{\frac{1}{2}} |\dots, n_j(\underline{q})+1, \dots\rangle \\ a_j(\underline{q}) |\dots, n_j(\underline{q}), \dots\rangle &= \{n_j(\underline{q})\}^{\frac{1}{2}} |\dots, n_j(\underline{q})-1, \dots\rangle \end{aligned} \quad (3.23)$$

The operators satisfy the commutation rules ( $[A, B] = AB - BA$ )

$$\begin{aligned} [a_j^+(\underline{q}), a_j^+(\underline{q}')] &= 0 \\ [a_j(\underline{q}), a_j(\underline{q}')] &= 0 \\ [a_j(\underline{q}), a_j^+(\underline{q}')] &= \delta_{jj'} \delta_{\underline{q}\underline{q}'} \end{aligned} \quad (3.24)$$

It follows from (3.23) that the operator product  $a_j^+(\underline{q})a_j(\underline{q})$  is the phonon number operator with eigenvalue  $n_j(\underline{q})$ .

At temperature T the expectation value of  $n_j(\underline{q})$  is

$$\langle n_j(\underline{q}) \rangle_T = [\exp(\hbar\omega_j(\underline{q})/k_B T) - 1]^{-1}. \quad (3.25)$$

Furthermore it can be shown that the Hamiltonian for the vibrating lattice becomes

$$H = \sum_{j\underline{q}} \hbar\omega_j(\underline{q}) \{ a_j^\dagger(\underline{q}) a_j(\underline{q}) + \frac{1}{2} \}$$

with corresponding energy eigenvalues

$$E = \sum_{j\underline{q}} \hbar\omega_j(\underline{q}) \{ n_j(\underline{q}) + \frac{1}{2} \}.$$

Thus a change in the energy of the crystal may be described as a creation or annihilation of a discrete number of phonons.

In terms of creation and annihilation operators, the displacement operator  $\underline{u}_\underline{L}(t)$  in a Bravais lattice can be written as [66]

$$\underline{u}_\underline{L}(t) = \sum_{j\underline{q}} \underline{\xi}_j(\underline{q}) \left\{ \frac{\hbar}{2NM\omega_j(\underline{q})} \right\}^{\frac{1}{2}} \times \\ [a_j(\underline{q}) \exp\{i\underline{q} \cdot \underline{L} - i\omega_j(\underline{q})t\} + a_j^\dagger(\underline{q}) \exp\{-i\underline{q} \cdot \underline{L} + i\omega_j(\underline{q})t\}], \quad (3.26)$$

which is the quantum-mechanical analogue of (2.21). The one-phonon cross section may be derived from the second term in the series expansion of (3.12), which contains the correlation function

$$\langle \{ \underline{Q} \cdot \underline{u}_\underline{L}(0) \} \{ \underline{Q} \cdot \underline{u}_\underline{L}'(t) \} \rangle_T \quad (3.27)$$

Substitution of (3.26) in (3.27) yields the expression

$$\sum_{j\underline{q}} \{ \underline{Q} \cdot \underline{\xi}_j(\underline{q}) \}^2 \frac{\hbar}{2NM\omega_j(\underline{q})} [ \langle n_j(\underline{q}) + 1 \rangle_T \exp\{i\underline{q} \cdot (\underline{L} - \underline{L}')\} \exp\{i\omega_j(\underline{q})t\} + \\ \langle n_j(\underline{q}) \rangle_T \exp\{-i\underline{q} \cdot (\underline{L} - \underline{L}')\} \exp\{-i\omega_j(\underline{q})t\} ] \quad (3.28)$$

where we have used

$$\langle a_j(\underline{q}) a_j(\underline{q}') \rangle_T = \langle a_j^\dagger(\underline{q}) a_j^\dagger(\underline{q}') \rangle_T = 0 \\ \langle a_j(\underline{q}) a_j^\dagger(\underline{q}') \rangle_T = \delta_{jj'} \delta_{\underline{q}\underline{q}'} \langle n_j(\underline{q}) + 1 \rangle_T \\ \langle a_j^\dagger(\underline{q}) a_j(\underline{q}') \rangle_T = \delta_{jj'} \delta_{\underline{q}\underline{q}'} \langle n_j(\underline{q}) \rangle_T \quad (3.29)$$

Again, the average  $\langle b_{\underline{L}} b_{\underline{L}'} \rangle$  may be separated into a coherent and an incoherent part (cf. (3.14)), which results in a corresponding separation of the inelastic cross section. The final expression for the coherent one-phonon cross section may now be derived from (3.12), (3.27) and (3.28):

$$\begin{aligned} \left( \frac{d^2 \sigma_n}{d\Omega dE} \right)_{\text{coh}}^{-1} &= \frac{k}{k_0} \frac{1}{2\pi\hbar} \int_{-\infty}^{+\infty} dt \exp(-i\omega t) \exp\{-2W(Q)\} \times \\ &\langle b \rangle^2 \sum_{\underline{L}, \underline{L}'} \exp\{i\underline{Q} \cdot (\underline{L}' - \underline{L})\} \langle \{ \underline{Q} \cdot \underline{u}_{\underline{L}}(0) \} \{ \underline{Q} \cdot \underline{u}_{\underline{L}'}(t) \} \rangle_T = \\ &= \langle b \rangle^2 \frac{k}{k_0} \frac{(2\pi)^3}{v_0} \frac{\hbar}{2M} \exp\{-2W(Q)\} \sum_{\underline{j}, \underline{q}, \underline{\tau}} \left\{ \frac{\underline{Q} \cdot \underline{\xi}_{\underline{j}}(\underline{q})}{\omega_{\underline{j}}(\underline{q})} \right\}^2 \times \\ &\quad [ \langle n_{\underline{j}}(\underline{q}) + 1 \rangle_T \delta\{\hbar\omega - \hbar\omega_{\underline{j}}(\underline{q})\} \delta(Q - \underline{q} - \underline{\tau}) + \\ &\quad \langle n_{\underline{j}}(\underline{q}) \rangle_T \delta\{\hbar\omega + \hbar\omega_{\underline{j}}(\underline{q})\} \delta(Q + \underline{q} - \underline{\tau}) ]. \end{aligned} \quad (3.30)$$

The cross section consists of two terms; the first one represents the creation processes, the second one the annihilation processes. Both terms contain two delta functions which ensure that energy and momentum are conserved. This implies that an incident neutron with wave vector  $\underline{k}_0$  can be scattered into the solid angle element  $d\Omega$  by only a few phonons with the proper  $\underline{q}$  and  $\omega_{\underline{j}}(\underline{q})$ . Owing to these restrictions it is possible to determine the phonon dispersion relation by means of neutron scattering.

The magnetic interaction gives rise to an extra contribution to the inelastic phonon scattering, which is usually called magnetovibrational scattering. Assuming that the effective spins  $\underline{S}_{\underline{L}}$  are oriented along the unit vector  $\underline{m}$  and remain unchanged during the scattering process, one may simplify (3.9):

$$\begin{aligned} \sum_{\alpha\beta} (\delta_{\alpha\beta} - e^{\alpha} e^{\beta}) \langle \sum_{\underline{L}, \underline{L}'} F_{\underline{L}}(\underline{Q}) F_{\underline{L}'}(\underline{Q}) S_{\underline{L}}^{\alpha}(0) \exp\{-i\underline{Q} \cdot \underline{R}_{\underline{L}}(0)\} \exp\{i\underline{Q} \cdot \underline{R}_{\underline{L}'}(t)\} S_{\underline{L}'}^{\beta}(t) \rangle_T = \\ \{ 1 - (\underline{e} \cdot \underline{m})^2 \} \langle S^z \rangle_T^2 F^2(Q) \langle \exp\{-i\underline{Q} \cdot \underline{R}_{\underline{L}}(0)\} \exp\{i\underline{Q} \cdot \underline{R}_{\underline{L}}(t)\} \rangle_T. \end{aligned}$$

Obviously the magnetovibrational scattering is determined by the same space-time correlation function that appears in expression (3.4) for the nuclear scattering, and therefore the magnetic part of the one-phonon cross section becomes

$$\left(\frac{d^2\sigma_m}{d\Omega dE}\right)^{-1} = \frac{k}{k_0} \frac{1}{2\pi\hbar} \int_{-\infty}^{+\infty} dt \exp(-i\omega t) \exp\{-2W(Q)\} \left(\frac{\gamma e^2}{m_e c^2}\right)^2 \langle S^z \rangle_T^2 F^2(Q) \times$$

$$\{1 - (\underline{e} \cdot \underline{m})^2\} \sum_{\underline{l}, \underline{l}'} \exp\{i\underline{Q} \cdot (\underline{l}' - \underline{l})\} \langle \underline{Q} \cdot \underline{u}_{\underline{l}}(0) \rangle \langle \underline{Q} \cdot \underline{u}_{\underline{l}'}(t) \rangle_T. \quad (3.31)$$

If the incident neutrons are unpolarized there is no interference between nuclear and magnetic scattering and the cross sections (3.30) and (3.31) may be added to find the total one-phonon cross section. The ratio between the two contributions is the same as in the elastic cross section.

The incoherent one-phonon cross section does not contain a magnetic part. From (3.12) and (3.14) one may derive

$$\left(\frac{d^2\sigma_n}{d\Omega dE}\right)_{\text{inc}}^{-1} = (\langle b^2 \rangle - \langle b \rangle^2) \frac{k}{k_0} \frac{1}{2M} \exp\{-2W(Q)\} \sum_{\underline{j}, \underline{q}} \frac{(\underline{Q} \cdot \underline{\xi}_{\underline{j}}(\underline{q}))^2}{\omega_{\underline{j}}(\underline{q})} \times$$

$$[\langle n_{\underline{j}}(\underline{q}) + 1 \rangle_T \delta\{\omega - \omega_{\underline{j}}(\underline{q})\} + \langle n_{\underline{j}}(\underline{q}) \rangle_T \delta\{\omega + \omega_{\underline{j}}(\underline{q})\}]. \quad (3.32)$$

In contrast to the coherent cross section (3.30), (3.32) does not contain delta functions associated with momentum conservation. Therefore all normal modes contribute to the scattering into the element  $d\Omega$ , and the energy spectrum of the scattered neutrons is related to the phonon frequency distribution

$$g(\omega) = \frac{1}{3N} \sum_{\underline{j}, \underline{q}} \delta\{\omega - \omega_{\underline{j}}(\underline{q})\}.$$

### 3.4.2. Inelastic magnetic scattering

The cross section for scattering by electron-hole excitations and magnons may be derived from (3.6) and (3.7). As a first approximation the coupling between the electron spin system and the lattice is neglected, and the z-axis is chosen as magnetization direction. After introduction of the Fourier transform  $\underline{S}(\underline{q})$  of the spin density distribution (3.6)

$$\underline{S}(\underline{q}) = \int d\underline{r} \exp(-i\underline{q} \cdot \underline{r}) \underline{S}(\underline{r}),$$

(3.7) may be written more concisely

$$\frac{d^2\sigma_m}{d\Omega dE} = \frac{k}{k_0} \left( \frac{\gamma e^2}{m_e c^2} \right)^2 \frac{1}{2\pi\hbar} \int_{-\infty}^{+\infty} dt \exp(-i\omega t) \sum_{\alpha\beta} (\delta_{\alpha\beta} - \mathbf{e}^\alpha \mathbf{e}^\beta) \langle S^\alpha(\mathbf{Q}, 0) S^\beta(-\mathbf{Q}, t) \rangle_T. \quad (3.33)$$

For an electron system where the z-component of the total spin is a constant of motion, only the correlation functions  $\langle S^z S^z \rangle_T$ ,  $\langle S^+ S^- \rangle_T$  and  $\langle S^- S^+ \rangle_T$  are different from zero,  $S^+$  and  $S^-$  being defined by

$$S^\pm = S^x \pm iS^y.$$

The summation over  $\alpha$  and  $\beta$  in (3.33) yields

$$\sum_{\alpha\beta} (\delta_{\alpha\beta} - \mathbf{e}^\alpha \mathbf{e}^\beta) \langle S^\alpha(\mathbf{Q}, 0) S^\beta(-\mathbf{Q}, t) \rangle_T = \{1 - (\mathbf{e} \cdot \mathbf{m})^2\} \langle S^z(\mathbf{Q}, 0) S^z(-\mathbf{Q}, t) \rangle_T + \frac{1}{4} \{1 + (\mathbf{e} \cdot \mathbf{m})^2\} \langle S^+(\mathbf{Q}, 0) S^-(\mathbf{Q}, t) + S^-(\mathbf{Q}, 0) S^+(\mathbf{Q}, t) \rangle_T. \quad (3.34)$$

Hence the cross section consists of two contributions; scattering without spin flip is related to  $\langle S^z S^z \rangle_T$ , whereas spin-flip scattering is determined by the second correlation function, which can be separated in  $\langle S^+ S^- \rangle_T$  and  $\langle S^- S^+ \rangle_T$ . In contrast to the theory for neutron-phonon scattering, the inelastic magnetic cross section is usually not calculated directly by means of the Fermion creation and annihilation operators, but is derived from the imaginary part of the dynamic spin susceptibility  $\chi^{\alpha\beta}(\mathbf{Q}, \omega)$  [53], defined by

$$\chi^{\alpha\beta}(\mathbf{Q}, \omega) = (g\mu_B)^2 \frac{1}{\hbar} \int_{-\infty}^{+\infty} dt \exp(i\omega t) \langle [S^\alpha(\mathbf{Q}, t), S^\beta(-\mathbf{Q}, 0)] \rangle_T,$$

where  $g$  is the gyromagnetic ratio of the electron. It can be shown that the cross section for spin-flip scattering is proportional to the imaginary part of  $\chi^{+-}(\mathbf{Q}, \omega)$  [66]:

$$\frac{d^2\sigma_m}{d\Omega dE} = \frac{k}{k_0} \left( \frac{\gamma e^2}{m_e c^2} \right)^2 F^2(\mathbf{Q}) \frac{1}{4} \{1 + (\mathbf{e} \cdot \mathbf{m})^2\} \frac{N}{(g\mu_B)^2} \times \frac{1}{\pi} \frac{1}{1 - \exp(-\hbar\omega/k_B T)} \{ \text{Im} \chi^{+-}(\mathbf{Q}, \omega) - \text{Im} \chi^{+-}(\mathbf{Q}, -\omega) \}. \quad (3.35)$$

The scattering cross section of Stoner excitations may be calculated from the susceptibility  $\chi_0^{+-}(\mathbf{Q}, \omega)$  of non-interacting electrons

$$\chi_0^{+-}(\mathbf{Q}, \omega) = (g\mu_B)^2 \frac{1}{N} \sum_{\mathbf{k}} \frac{n_{\mathbf{k}+} - n_{\mathbf{k}+\mathbf{Q}+}}{E(\mathbf{k}+\mathbf{Q}+) - E(\mathbf{k}+) + \hbar\omega + i0^+} \quad (3.36)$$

Here  $\underline{k}$  denotes the electron wave vector and  $n_{\underline{k}\sigma}$  the occupation number of the state  $|\underline{k}\sigma\rangle$ :

$$n_{\underline{k}\sigma} = \langle n_{\underline{k}\sigma} \rangle_T = \left[ \exp \left( \frac{E(\underline{k}\sigma) - E_F}{k_B T} \right) + 1 \right]^{-1}, \quad (3.37)$$

where  $E_F$  is the Fermi energy. Making use of the relation

$$\frac{1}{x + i0^+} = \frac{1}{x} - i\pi\delta(x), \quad (3.38)$$

one obtains the following expression for the scattering cross section

$$\frac{d^2\sigma_m}{d\Omega dE} = \frac{1}{4} \frac{k}{k_o} \left( \frac{\gamma e^2}{m_e c^2} \right)^2 F^2(Q) \{1 + (\underline{e} \cdot \underline{m})^2\} \sum_{\sigma \neq \sigma'} \sum_{\underline{k}} n_{\underline{k}\sigma} (1 - n_{\underline{k}+Q\sigma'}) \times \delta\{E(\underline{k}+Q\sigma') - E(\underline{k}\sigma) - \hbar\omega\}. \quad (3.39)$$

In an energy-loss or energy-gain process described by (3.39) the electron is transferred from the state  $|\underline{k}\sigma\rangle$  to the state  $|\underline{k}+Q\sigma'\rangle$ , the neutron spin flips and the neutron energy and momentum change in accordance with the conservation laws. As shown by Elliott in a calculation on iron [75], the neutron scattering cross section for non-interacting electron-hole excitations is weak. Moreover, the neutrons are scattered over a wide angular range with a large spread in energy, which is connected with the fact that the excitations occupy a continuum in  $(Q, \omega)$ -space (cf. figure 2.5).

For a system of interacting electrons described by the Hamiltonian (2.35) the susceptibility is given by

$$\chi^{+-}(Q, \omega) = \frac{\chi_o^{+-}(Q, \omega)}{1 - V\chi_o^{+-}(Q, \omega)}, \quad (3.40)$$

where the matrix element  $V(\underline{q}')$  in (2.35) has been replaced by a constant  $V$ . From (3.40) one obtains

$$\text{Im}\chi^{+-}(Q, \omega) = \frac{\text{Im}\chi_o^{+-}(Q, \omega)}{\{1 - V\text{Re}\chi_o^{+-}(Q, \omega)\}^2 + \{V\text{Im}\chi_o^{+-}(Q, \omega)\}^2}, \quad (3.41)$$

where the real and imaginary parts of  $\chi_o^{+-}(Q, \omega)$  are defined by (3.36) and (3.38). Since  $\text{Im}\chi_o^{+-}(Q, \omega) = 0$  outside the continuum of Stoner excitations,

$\text{Im}\chi^{+-}(\underline{Q}, \omega)$  may be replaced by a  $\delta$ -function

$$\text{Im}\chi^{+-}(\underline{Q}, \omega) = \frac{\pi}{V} \delta\{1 - V\text{Re}\chi_0^{+-}(\underline{Q}, \omega)\}. \quad (3.42)$$

Hence the scattering by collective electron excitations leads to a well-defined energy transfer  $\hbar\omega$ , where  $\omega$  satisfies the condition

$$1 - V\text{Re}\chi_0^{+-}(\underline{Q}, \omega) = 0, \quad (3.43)$$

and it may be readily verified that this value of  $\omega$  is equal to the angular frequency of the magnon with wave vector  $\underline{q} = \underline{Q} - \underline{\tau}$ , defined in (2.42).

From (3.35) and (3.42) one may finally derive the following expression for the neutron-magnon cross section [66]:

$$\begin{aligned} \left(\frac{d^2\sigma_m}{d\Omega dE}\right)^{-1} &= \frac{k}{k_0} \left(\frac{2\pi}{v_0}\right)^3 \left(\frac{\gamma e^2}{m c^2}\right)^2 F^2(\underline{Q}) \frac{1}{4} [1 + (\underline{e}, \underline{m})^2] \langle S^z \rangle_T \times \\ &\sum_{\underline{q}, \underline{\tau}} [\langle n(\underline{q}) + 1 \rangle_T \delta\{\hbar\omega - \hbar\omega(\underline{q})\} \delta(\underline{Q} - \underline{q} - \underline{\tau}) + \\ &\langle n(\underline{q}) \rangle_T \delta\{\hbar\omega + \hbar\omega(\underline{q})\} \delta(\underline{Q} + \underline{q} - \underline{\tau})], \end{aligned} \quad (3.44)$$

where the magnon dispersion relation  $\omega(\underline{q})$  is given by (2.43) for small  $\underline{q}$ , and the occupation number  $\langle n(\underline{q}) \rangle_T$  is the same as for phonons (cf. (3.25)).

In a system of interacting electrons the scattering by the Stoner excitations becomes very weak [76, 77]. This is a consequence of the sum rule (cf. ref. [77], p. 876)

$$\int_{-\infty}^{+\infty} d\omega \text{Im}\chi^{+-}(\underline{Q}, \omega) = \frac{2\pi}{\hbar} \{\langle n_{\downarrow} \rangle - \langle n_{\uparrow} \rangle\}$$

which gives the relation between the integral over  $\text{Im}\chi^{+-}$  and the number of Bohr magnetons per atom. Hence the peak in the susceptibility at  $\omega = \omega(\underline{q})$  due to the magnons must be compensated by a decrease in the susceptibility of the Stoner excitations, which results in a decrease in the scattering by these modes.

Before concluding this section, a few remarks should be added with regard to the calculation of the cross sections. In the derivation of (3.39) and (3.44) from the dynamic susceptibility the vibration of the lattice is not taken into account and therefore the Debye-Waller factor does not appear in the cross section formulae. For a comparison of the relative magnitude of the magnon and phonon cross sections one may use (3.30), (3.31) and



(3.44) with  $\exp(-2W) = 1$ . As far as the  $Q$ -dependent factors are concerned, the magnon cross section varies as  $F^2(Q)$ , which is a rapidly decreasing function of  $Q$  (cf. table 3.2), whereas the nuclear part of the phonon cross section (3.30) increases as  $Q^2$ , and the magnetovibrational part (3.31) varies as  $Q^2 F^2(Q)$ .

It may be readily verified that the inelastic cross sections (3.30) and (3.44) obey the detailed-balance condition (3.22), because the ratio between energy loss and energy gain scattering is determined by  $\langle n(q)+1 \rangle_T / \langle n(q) \rangle_T = \exp(\hbar\omega/k_B T)$ . The same ratio is found for the scattering by Stoner modes when the Fermion occupation numbers (3.37) are substituted in (3.39).

In the derivation of the magnetic cross sections in this chapter the contribution due to the orbital magnetic moment of the electrons has been neglected. For the elastic cross section this contribution is small, and may be estimated by means of the known value of the magneto-mechanical ratio [68,70]. For the inelastic cross section of the Stoner modes the ratio between spin-spin and spin-orbit scattering depends on the energy and momentum transfer. Calculations on paramagnetic nickel by Lovesey and Windsor [78,79] show that for large energy transfer ( $\hbar\omega > 0.15$  eV) the orbital susceptibility  $\text{Im}\chi_L(Q, \omega)$  is comparable with or even larger than  $\text{Im}\chi_S(Q, \omega)$ . However, in the range  $\hbar\omega < 0.05$  eV, which is of interest for neutron scattering experiments,  $\text{Im}\chi_L$  is considerably smaller than  $\text{Im}\chi_S$ . In this energy range the scattering by magnons, which depends solely on  $\text{Im}\chi_S$ , is dominant in comparison with the scattering by Stoner modes. In natural nickel the neutron-magnon cross section is on the other hand small in comparison with the neutron-phonon cross section.

To give a comparison between the cross sections (3.30) and (3.44), we shall calculate the scattering cross sections for the magnon and the phonon observed in the experiment that is shown in figure 5.9.

At  $T = 295$  K the occupation number of a collective excitation with  $\nu = 3.63$  THz is given by  $\langle n(\nu) \rangle_{295} = 1.242$ . Moreover, the values  $k = 3.746 \text{ \AA}^{-1}$ ,  $k_0 = 4.612 \text{ \AA}^{-1}$  and  $\exp(-2W) = 1$  are used. The final values for the cross sections are  $46.3 \times 10^{-27} \text{ cm}^2$  for the phonon and  $26.2 \times 10^{-27} \text{ cm}^2$  for the magnon (cf. table 3.2 and figure 5.9).

### 3.4.3. Selection rules

Even without detailed knowledge of the cross sections it is possible to establish selection rules for the various scattering processes by means of (2.13). In an inelastic scattering process the transition between the initial state  $|\underline{k}_0 s_0\rangle$  and the final state  $|\underline{k} s\rangle$  of the neutron is induced by a time dependent perturbation  $H'(\underline{r}, t)$ , which may, for example, represent the interaction between the neutron and a phonon. It may be seen from (3.1) that the matrix element corresponding to this transition does not depend on  $\underline{k}$  and  $\underline{k}_0$ , but only on  $\underline{Q} = \underline{k}_0 - \underline{k}$ , and it is convenient to establish the selection rules on basis of the point group of the scattering vector. The procedure may be illustrated by means of the following example.

Consider a phonon with wave vector  $\underline{q}$  in a cubic crystal, its wave function transforming according to an irreducible representation  $\Gamma^\alpha$  of  $G_0(\underline{q})$ , and suppose that a scattering experiment is performed at  $\underline{Q} = \underline{q} + \underline{r}$ . The point group of  $\underline{Q}$ ,  $G_0(\underline{Q})$ , is a subgroup of  $G_0(\underline{q})$ , consisting of those elements of  $G_0(\underline{q})$  that leave  $\underline{Q}$  invariant. In contrast to  $G_0(\underline{q})$ ,  $G_0(\underline{Q})$  does not contain operations that transform  $\underline{Q}$  into  $\underline{Q} + \underline{r}$ . This is a consequence of the fact that  $\underline{Q}$  is determined by the experimental scattering configuration, i.e. an experiment performed in  $\underline{Q}$  is not equivalent to an experiment in  $\underline{Q} + \underline{r}$ . The compatibility relations between  $\Gamma^\alpha$  of  $G_0(\underline{q})$  and the irreducible representations of  $G_0(\underline{Q})$  may be determined by means of the subduction procedure described in section 2.2. If the spin functions  $|s_0\rangle$  and  $|s\rangle$  of the neutron transform as  $\Gamma^i$  and  $\Gamma^f$  of  $G_0(\underline{Q})$ , and if  $\Gamma^\alpha$  is compatible with  $\Gamma^p$  of  $G_0(\underline{Q})$ , then neutron-phonon scattering is allowed by symmetry if (2.13) holds, the summation in (2.13) being restricted to the elements  $T$  of  $G_0(\underline{Q})$ . It should be emphasized that the neutron spin functions transform according to double-valued representations.

If  $\underline{Q}$  is parallel with a mirror plane of the reciprocal lattice,  $G_0(\underline{Q}) = C_s$  and the neutron states transform according to the two complex conjugate representations  $\Gamma^3$  and  $\Gamma^4$  of  $C_s$  (see table A.5). In a coherent neutron-phonon scattering process the neutron spin does not flip, which implies that  $\chi_f^*(T)\chi_i(T) = 1$  for the elements  $T$  of  $G_0(\underline{Q})$ . Substitution of this result in (2.13) shows that only the phonons transforming as  $\Gamma^1$  of  $C_s$  (+ in BSW notation, cf. table 2.3) can contribute to the scattering.

If  $\underline{Q}$  is parallel with one of the symmetry directions  $\Delta$ ,  $\Lambda$  or  $\Sigma$  the neutron states transform according to the two rows of the double-valued representations  $\Delta_6$ ,  $\Lambda_6$  or  $\Sigma_5$ , respectively, and the selection rule (2.13) does not allow a distinction between processes with and without spin flip. However, a more sophisticated selection rule may be formulated for states that transform as the rows of an 1-dimensional representation. In the case of neutron scattering, the two different processes may be distinguished if the pure spin states  $|\uparrow\rangle$  and  $|\downarrow\rangle$  are chosen as basis for the representations mentioned above. Scattering of a neutron with spin  $s_0 = \uparrow$  without spin flip by an excitation with wave function  $\Psi(\underline{r})$  is allowed by symmetry if  $\Psi(\underline{r})|\uparrow\rangle$  contains a part that transforms as  $|\uparrow\rangle$ . The extension of this selection rule to other processes is straightforward. To apply the rule in practice it is convenient to use the tables of coupling coefficients in [27]. In the case of neutron-phonon scattering with  $\underline{Q}$  along one of the three high-symmetry directions, it is found that only the phonons transforming as  $\Delta_1, \Lambda_1$  and  $\Sigma_1$  (i.e. the longitudinal phonons) may give rise to neutron scattering.

Similar selection rules may be applied to the scattering by excitations with a lower symmetry. In the present report we are mainly concerned with excitations transforming as irreducible representations of the magnetic point group  $G_0^M(\underline{q})$  or the pseudo-magnetic point group  $G_0^{+M}(\underline{q})$  (see section 2.2 for the definition of these groups), and the selection rules are in that case based on the corresponding point groups of the scattering vector,  $G_0^M(\underline{Q})$  or  $G_0^{+M}(\underline{Q})$ . As an illustration of magnetic selection rules we consider the case  $\underline{M} // [01\bar{1}]$  and  $\underline{Q}$  in the  $(01\bar{1})$  plane, with  $G_0^M(\underline{Q}) = C_s$  (see table A.5). The neutron states  $|\uparrow\rangle$  and  $|\downarrow\rangle$  transform according to  $\Gamma^3$  and  $\Gamma^4$ , respectively. Consequently,  $\Gamma^1$  excitations (e.g. electron-hole excitations with spin 0) may lead to neutron scattering without spin flip, whereas spin-flip scattering can only be induced by an excitation transforming as  $\Gamma^2$  (a magnon or Stoner excitation). A detailed discussion of a number of different configurations for  $\underline{M}$  and  $\underline{Q}$  is given in section 6.6 and appendix B.

## CHAPTER IV

## EXPERIMENTAL TECHNIQUES

4.1. Introduction

As shown in chapter III, the coherent one-phonon and one-magnon cross sections (3.30) and (3.44) are zero except for those combinations of  $\underline{k}_0$ ,  $\underline{k}$ ,  $\underline{q}$  and  $\omega(\underline{q})$  that obey the conservation laws for energy and momentum

$$\underline{Q} = \underline{k}_0 - \underline{k} = \pm \underline{q} + \underline{\tau} \quad (4.1)$$

$$\hbar\omega = \frac{\hbar^2}{2m_n} (k_0^2 - k^2) = \pm \hbar\omega(\underline{q}) \quad (4.2)$$

The scattering conditions (4.1) and (4.2) refer to a process in which an excitation with wave vector  $\underline{q}$  and energy  $\hbar\omega(\underline{q})$  is created or annihilated. From the neutron wave vectors  $\underline{k}_0$  and  $\underline{k}$  for which a maximum in the cross section is observed one may derive both  $\underline{q}$  and  $\omega(\underline{q})$  for the excitation involved in the scattering process. By means of a series of measurements for different  $\underline{q}$ 's one may in principle determine the dispersion relation  $\omega(\underline{q})$  of the excitation throughout the Brillouin zone. For the investigation of the nickel crystals two different neutron spectrometers have been used: a time-of-flight spectrometer and a triple-axis spectrometer. A short description of these instruments, which are equipped with different analyzer systems, is given in sections 4.2 and 4.3, respectively.

As in other experimental techniques, a compromise between transmitted intensity and resolving power should be sought by means of an appropriate choice for the disposable parameters of the set-up. In the present experiments the scattering cross section is relatively small and therefore the collimation angles for the neutron beams have to be rather large. The relation between the instrumental parameters and the "resolution ellipsoid" in  $(\omega, \underline{Q})$ -space is considered in section 4.4.

4.2. Time-of-flight spectrometer

In figure 4.1. the spectrometer is shown schematically. A monochromatic beam is selected from thermal neutron spectrum of the reactor by means of Bragg reflection at the (0002) planes of a zinc crystal. At the fixed scattering angle  $2\theta_M = 35^\circ$ , which is defined by a 30' collimator placed in front of the monochromator and a 22 x 45 mm<sup>2</sup> diaphragm at the exit of the

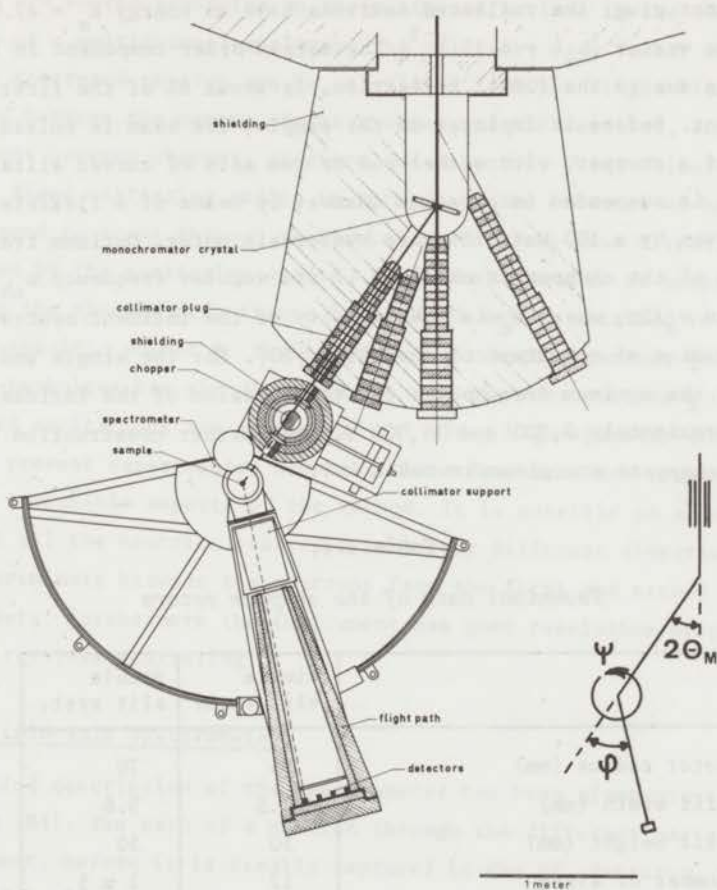


Figure 4.1.

Mechanical part of the time-of-flight spectrometer. The angular positions  $\psi$  and  $\phi$  of the sample table and the flight path may be varied in steps of  $2.16^\circ$  by means of step motors. The rotor with the double slit system is shown; the vacuum chamber is surrounded by a shielding drum and mounted on a translation table, which allows accurate adjustment of the rotor position and complete removal of the chopper and its shielding from the beam path.

collimator plug, the reflected neutrons have an energy  $E_0 = 37.0$  meV and wave vector  $|k_0| = 4.22 \text{ \AA}^{-1}$ . The second order component in the beam, which is due to the (0004) reflection, is about 8% of the first order component. Before it impinges on the sample, the beam is pulsed by means of a chopper, with either one or two sets of curved slits. The chopper is suspended in a vacuum chamber by means of a flexible shaft and driven by a 100 Watt, 3 phase hysteresis motor. Optimum transmission of the chopper is obtained if its angular frequency  $\omega_{ch}$  is equal to  $v_0/2\rho$ , where  $v_0$  is the velocity of the incident neutrons and  $\rho$  the radius of curvature of the slits  $|80|$ . For the single and double chopper the optimum frequencies for transmission of the incident beam are approximately 9,300 and 15,300 r.p.m. Further construction details of the choppers are given in table 4.1.

Table 4.1.

*Technical data of the chopper rotors*

	single slit syst.	double slit syst.
rotor radius (mm)	55	70
slit width (mm)	2.5	5.6
slit height (mm)	50	50
number of slits	12	2 x 5
thickness of steel plates (mm)	1.3	1.1
radius of curvature, $\rho$ (cm)	136	83
max. speed (r.p.m.)	20,000	16,000

The scattered neutrons may be detected simultaneously at four different scattering angles by detectors placed in a shielded flight path at a distance of 191 cm from the sample. The detectors have a sensitive volume of  $2.5 \times 2.5 \times 10 \text{ cm}^3$  filled with  $^3\text{He}$  to a pressure of 6 atm. and may be mounted vertically at 23 alternative positions. There is no additional collimation for the scattered beam, and hence the opening angle of a detector is determined by the size of its front surface ( $10 \times 2.5 \text{ cm}^2$ ) and the dimensions of the sample. After amplification and discrimination the detector

pulses are stored according to their time of arrival in the 1024-words memory of a multichannel analyzer. The velocity, wave vector and energy of the scattered neutron can be calculated from the flight time of the neutron between the centre of the chopper and the detector, and the known distances between chopper, specimen and detector. Observations are carried out at fixed scattering angles in periods of the order of 48 hours, and correspond to scans through reciprocal space along four directions determined by the scattering angles. In general a number of peaks will appear in the spectra (cf. figure 5.1), which may be ascribed to scattering in specific points  $Q$ . Besides the long counting period, the time-of-flight technique has the disadvantage that the wave vectors  $q$  of the observed excitations are in general not along high-symmetry directions. In the present experiments, however, these drawbacks are compensated by the favourable aspects of the method. It is possible to accept and analyze all the neutrons scattered into four different directions, and to discriminate between the neutrons from the first and second order components. Furthermore the instrument has good resolution properties for energy-loss scattering.

#### 4.3. Triple-axis spectrometer

A detailed description of the spectrometer has been given previously by Bergsma [81]. The path of a neutron through the different parts of the instrument, before it is finally captured in the  $BF_3$  detector, is sketched in figure 4.2.

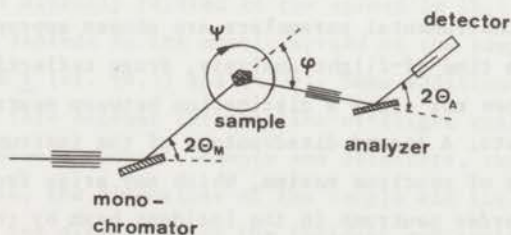


Figure 4.2.

*Scheme of the triple-axis spectrometer.*

In comparison with the time-of-flight spectrometer, the triple-axis spectrometer is a more versatile instrument. This is due to the fact that there are four independent angular variables,  $2\theta_M$ ,  $\psi$ ,  $\phi$  and  $2\theta_A$ , which may be adjusted by means of three rotation axes.  $\psi$  denotes the angular position of the sample, while  $2\theta_M$ ,  $\phi$  and  $2\theta_A$  are the scattering angles for the neutron at the monochromator, the sample and the analyzer crystal, respectively. Collimators are placed in front of the monochromator and analyzer, while 2 : 1 reduction gears ensure that the monochromator and analyzer crystals are kept in Bragg reflection position when the angles  $2\theta_M$  and  $2\theta_A$  are changed. The wave vector  $\underline{k}_0$  is determined by the value of  $2\theta_M$ , while the analyzing system is open for those neutrons that are scattered through the second collimator and have a wave vector  $\underline{k}$  satisfying the Bragg reflection condition for the chosen angle  $2\theta_A$ .

By means of the four disposable parameters arbitrary scans through  $(\omega, Q)$ -space can be performed, a complete scan consisting of a series of subsequent counting periods of about 10 minutes at fixed values for the angular positions. In practice the spectrometer is operated in constant- $Q$  or constant- $\omega$  configurations. The former mode of operation corresponds to an  $\omega$ -scan at a fixed point  $Q$  in reciprocal space and involves variations in  $2\theta_M$ ,  $\psi$ , and  $\phi$ . In the latter mode the energy transfer  $\hbar\omega$  is kept constant while  $\psi$  and  $\phi$  are usually varied in such a way that a series of wave vectors  $\underline{q}^{(i)}$  along a symmetry direction is scanned. In figure 4.3. both operation modes are shown in reciprocal space and compared with a time-of-flight scan.

Application of the procedures described above results in the observation of a single excitation with a predetermined wave vector or frequency, if the instrumental parameters are chosen appropriately.

In contrast to a time-of-flight analysis, Bragg reflection by the analyzer crystal does not allow a distinction between neutrons with wave vectors  $\underline{k}$ ,  $2\underline{k}$ , etc. A second disadvantage of the instrument is the possible occurrence of spurious maxima, which may arise from Bragg reflection of higher order neutrons in the incident beam by the sample, followed by incoherent scattering of these neutrons into the detector by the analyzer crystal.



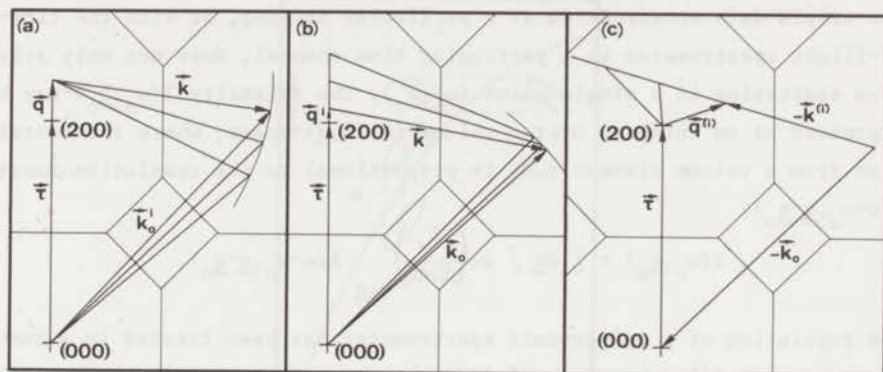


Figure 4.3.

Different scans in  $(\omega, Q)$ -space. (a): triple-axis, constant- $Q$  scan; (b): triple-axis, constant- $\omega$  scan; (c): time-of-flight scan.

#### 4.4. Resolution

There exists a strong correlation between the luminosity and the resolution of the spectrometers. For the triple-axis spectrometer these properties are determined by the collimation of the neutron beam, both in horizontal and vertical direction, and the distribution of the mosaic blocks in the three crystals, which corresponds to a spread in the direction of the reciprocal lattice vectors  $\underline{\tau}$ . Consequently there will be a spread both in length and direction for the wave vectors  $\underline{k}_0$  and  $\underline{k}$  of the neutrons that reach the sample and are accepted by the analyzer system. The spread in the energy transfer to the sample is directly related to the spread in  $|\underline{k}_0|$  and  $|\underline{k}|$ , while the spread in  $q$  depends on the mosaic spread of the sample and the spread in  $\underline{k}_0$  and  $\underline{k}$  (cf. (4.1) and (4.2)). Some additional factors should be taken into account for the time-of-flight spectrometer, viz. the distances between chopper, sample and detectors, the width  $\Delta t$  of the neutron pulse, the dimensions of the sample and its orientation with respect to the directions of the incident and scattered neutrons (if the sample is not axially symmetric), the detector thickness and the width of the time channels.

As a result of these instrumental factors, the intensity observed with the triple-axis spectrometer at a particular setting, or with the time-of-flight spectrometer in a particular time channel, does not only arise from scattering in a single point  $(\omega_0, \underline{q}_0)$ . The intensity  $I(\omega_0, \underline{q}_0)$  may be expressed as an integral over a volume in  $(\omega, \underline{q})$ -space, where the contribution from a volume element  $d\omega d\underline{q}$  is proportional to the resolution function  $R(\omega - \omega_0, \underline{q} - \underline{q}_0)$ :

$$I(\omega_0, \underline{q}_0) = \int d\underline{q} \int d\omega \left( \frac{d^2\sigma}{d\Omega dE} \right)_{\omega, \underline{q}} R(\omega - \omega_0, \underline{q} - \underline{q}_0).$$

The resolution of a triple-axis spectrometer has been treated in a number of papers [82-84], whereas a similar treatment for a hybrid time-of-flight spectrometer as described in section 4.2 may be found in [85]. A review of the various methods to calculate and to measure the resolution function has been given by Bjerrum Møller and Nielsen [86].

For both instruments the resolution may in first approximation be described by a Gaussian function

$$R(\omega - \omega_0, \underline{q} - \underline{q}_0) = R_0 \exp\left(-\sum_{k=1}^4 \sum_{l=1}^4 M_{kl} X_k X_l\right),$$

where  $X_1, X_2$  and  $X_3$  denote the three components of  $\underline{q} - \underline{q}_0$ ,  $X_4 = \omega - \omega_0$ , and  $R_0$  and  $M_{kl}$  are complicated functions of the instrumental parameters of the spectrometer under consideration. The surfaces in  $(\omega, \underline{q})$ -space with constant  $R(\omega - \omega_0, \underline{q} - \underline{q}_0)$  are ellipsoids, and the one for which  $R(\omega - \omega_0, \underline{q} - \underline{q}_0) = \frac{1}{2}R_0$  is usually referred to as "the resolution ellipsoid".

To determine a point  $\omega_0(\underline{q}_0)$  of the dispersion relation of an excitation by means of a spectrometer scan, the centre of the resolution ellipsoid is moved through the point  $(\omega_0, \underline{q}_0)$  of the dispersion surface in  $(\omega, \underline{q})$ -space. Obviously, the height and width of the peak in the spectrum of scattered neutrons is related to the orientation of the ellipsoid with respect to the dispersion surface. Sharply defined peaks are expected when the shortest axis of the ellipsoid is approximately normal to the dispersion surface, a situation which is illustrated for two dimensions in figure 4.4. These "focusing" effects are of interest for the selection of an optimum experimental configuration for the determination of a specific branch of a dispersion relation. To avoid a complete calculation of the resolution ellipsoid, graphical methods have been developed for a triple-axis spectrometer [87,88], to determine the focusing configuration.

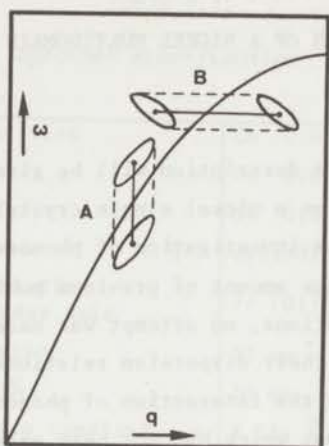


Figure 4.4.

*Focusing effects in inelastic neutron scattering.*

*A: constant- $Q$  scan in focused configuration;*

*B: constant- $\omega$  scan in defocused configuration.*

CHAPTER V

INVESTIGATION OF A NICKEL MULTIDOMAIN SINGLE CRYSTAL

5.1. Introduction

In the present chapter a description will be given of a number of introductory experiments on a nickel single crystal. The measurements were partly aimed at the investigation of phonons and magnons, but in view of the impressive amount of previous publications [1-11] on these well-known excitations, no attempt was made to repeat the complete determination of their dispersion relations. The central subject of this chapter is the interaction of phonons and magnons with an elementary excitation, which has not been observed previously. To collect information on this excitation and on its interaction with the known excitations, a search was made for perturbations in the phonon and magnon dispersion relations. The discovery of the excitation, which, for reasons to be explained later, will be denoted as a mixed excitation, is described in section 5.2. In sections 5.3 and 5.4 a summary will be given of detailed measurements by means of the triple-axis spectrometer on the mixed excitation, phonons and magnons. A discussion of the experimental results will be presented in section 5.5.

All experiments reported in this chapter were carried out at room temperature on a large single crystal that was borrowed from S.C.K., Mol, Belgium by courtesy of Dr. S. Hautecler. Actually, the experiments described in [1] and [3] were carried out on the same crystal<sup>\*)</sup>. Some of its properties are listed in table 5.1. Since no external magnetic field was applied, the crystal may be assumed to consist of a large number of domains with various magnetization directions.

-----  
<sup>\*)</sup>This is a specimen with the natural isotopic composition.

Table 5.1.

Specimen specification

impurities	Cu 0.01%
	Fe 0.05%
	Si 0.01%
shape	cylindrical
orientation cylinder axis	// $[01\bar{1}]$
diameter	30 mm
length	70 mm
lattice constant, a	3.524 Å

5.2. Time-of-flight measurements

The first experimental evidence for the existence of an additional elementary excitation in nickel was obtained from three time-of-flight runs, which will be discussed below. The chopper rotor with the single slit system was operated at a speed of  $9775 \pm 10$  r.p.m. To increase the counting rate at the expense of angular resolution, the four detectors were placed side by side to form a  $10 \times 10 \text{ cm}^2$  sensitive area, and the pulses from the detectors were added.

The experiments were carried out with  $\underline{k}_0$  and  $\underline{k}$  parallel either to the  $(01\bar{1})$  plane or to the  $(001)$  plane. As discussed in section 2.3, the phonons with wave vectors  $\underline{q}$  in a mirror plane of the reciprocal lattice have polarization vectors  $\underline{\epsilon}_j$  either in or perpendicular to this plane (cf. table 2.3). The factor  $(\underline{Q} \cdot \underline{\epsilon}_j)^2$  in the neutron-phonon cross section (3.30) ensures that only the phonons with  $\underline{\epsilon}_j$  in the scattering plane (i.e. the phonons transforming as representation +) will be observable. To compare the frequencies of the observed phonons with the results in [2], the phonon frequencies and corresponding polarization vectors in the  $(01\bar{1})$  and  $(001)$  planes were calculated from the set of interatomic force constants determined by Birgeneau et al. (see table 2.1).

Figure 5.1. shows a part of the time-of-flight spectrum obtained in the  $(001)$  plane. In inset (a) the experimental configuration in  $\underline{Q}$ -space

is given. The calculated phonon dispersion relation along the path of  $\underline{k}$  is plotted in inset (b); the dotted line in (b) indicates the energy change of the neutron,  $|\underline{k}_0^2 - \underline{k}^2| \hbar^2 / 2m_n$ , expressed in THz (1 THz = 4.135 meV). Phonons are expected to be observed at the intersection points of the dotted line and the phonon branches with even symmetry (+). The frequencies corresponding to the observed three maxima in the time-of-flight spectrum are plotted in (b), the corresponding scattering vectors  $\underline{Q}$  and calculated polarization vectors  $\underline{\xi}$  in (a).

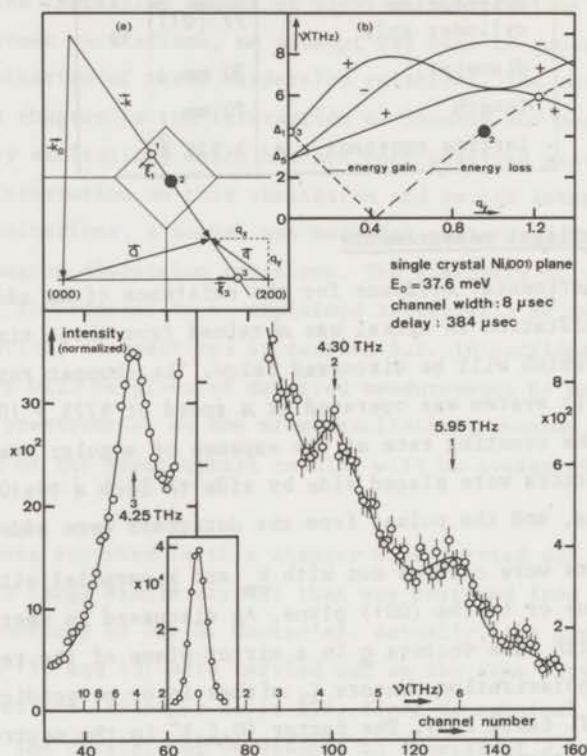


Figure 5.1.

Time-of-flight experiment in the (001) plane. The dominant peak at  $v = 0$  is due to incoherent elastic scattering. Maximum 2 corresponds to the mixed excitation. In inset (a) the experimental configuration in  $\underline{Q}$ -space is shown, in inset (b) the calculated phonon dispersion relation and neutron-energy transfer curve. The frequencies, wave vectors and polarization vectors (for phonons) of the observed excitations are indicated in (a) and (b). The normalization procedure is described in the text.

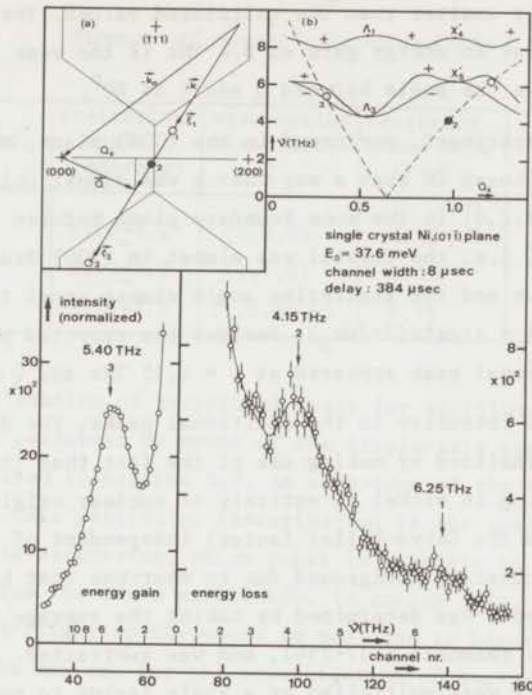


Figure 5.2.

*Time-of-flight experiment in the  $(0\bar{1}\bar{1})$  plane. The lay-out is the same as in figure 5.1, with omission of the incoherent elastic peak.*

It is obvious that the maxima 1 and 3 are due to phonon scattering. The longitudinal ( $\Delta_1$ ) phonon is observed in energy gain under nearly optimum conditions:  $Q/\xi_3$ . On the other hand, the + phonon at  $\nu = 3.20$  THz is unobservable, because the calculated angle between  $Q$  and  $\xi$  is  $70^\circ$ . Maximum 2 cannot be explained by phonon scattering and indicates that some other excitation with a frequency  $\nu = 4.30$  THz must have given rise to neutron scattering at  $Q \approx (1,1,0)$ .

The existence of this excitation was confirmed by a subsequent measurement in the  $(0\bar{1}\bar{1})$  plane. The experiment shown in figure 5.2. was intended to observe the excitation with a reduced wave vector  $(1,0,0)$ , which is equivalent to  $(1,1,0)$  in an f.c.c. lattice. As may be seen from the spectrum, an additional maximum is indeed observed close to  $(1,0,0)$  at approximately the same frequency:  $\nu = 4.15$  THz. The maxima

1 and 3 are again due to scattering by phonons; the observed frequencies are slightly smaller than the calculated values. The expected second phonon peak in energy gain at 8.4 THz is too weak to be observable, because the angle between  $\underline{Q}$  and  $\underline{\xi}$  is  $80^\circ$ .

For the third experiment, performed in the (001) plane, the configuration was chosen in such a way that  $\underline{k}$  was almost coincident with the line  $[1, \tau, 0]$  in the zone boundary plane between the (000) and (200) zones, i.e. the crystal was almost in (200) Bragg reflection position and the scattering angle almost equal to  $\arcsin(\lambda_0/2d_{200}) = \arcsin(2\pi/ak_0)$ . Besides the expected phonon peaks, an additional peak appeared at  $\nu = 4.15$  THz and  $\underline{Q} = (1, 0.46, 0)$ .

To determine the intensity in the additional peaks, the different spectra were normalized by making use of the fact that the incoherent elastic scattering in nickel is entirely of nuclear origin and therefore (apart from the Debye-Waller factor) independent of the scattering angle. The constant background due to neutrons that have not passed through the chopper was determined by taking the average intensity in the last 40 time channels (217-256), and was subtracted. Next, the corrected spectra were multiplied by a scale factor to normalize the total number of counts in the elastic incoherent peak to the value  $199.1 \times 10^3$ , which corresponds to an intensity of roughly  $4 \times 10^4$  counts in the central channel of the peak. The remaining background is largely due to inelastic incoherent phonon scattering from the specimen. For a final correction, this contribution was determined by means of separate time-of-flight measurements on a polycrystalline nickel sample at scattering angles  $26.2^\circ$  and  $28.9^\circ$ , where coherent elastic scattering was known to be absent and coherent inelastic scattering was weak. After normalization of the background spectrum and subsequent subtraction from the other three spectra, the integrated intensity in the additional peak could be determined. A summary of the results is given in table 5.2. By means of the known value for the incoherent elastic scattering cross section in nickel ( $\langle b^2 \rangle - \langle b \rangle^2 = 0.37$  barn/ster.atom) one may estimate the scattering cross section of the mixed mode. The normalized integrated intensity of 2650 counts, for example, corresponds to a scattering cross section of 4.9 mbarn/ster.atom.



Table 5.2.

Summary of time-of-flight results

run nr.	scattering angle (degrees)	wave vector mixed mode $\underline{Q}$	frequency mixed mode (THz)	integrated intensity (normalized)
2	21.0 $\pm$ 1.2	(1,0,0)	4.15	2650 $\pm$ 450
1	36.2 $\pm$ 1.2	(1,1,0)	4.30	2210 $\pm$ 370
3	25.6 $\pm$ 1.2	(1,0.46,0)	4.15	950 $\pm$ 580

A further exploration of reciprocal space for additional scattering processes was performed by means of the triple-axis spectrometer, and will be described in section 5.3. An advantage of the time-of-flight technique for this particular investigation is the good resolution for energy loss scattering, which makes it possible to distinguish the phonons from the mixed excitation. In energy gain, the resolution of the time-of-flight spectrometer is poor and it becomes impossible to separate the maxima. For the investigation of energy gain processes the use of the triple-axis spectrometer is therefore indispensable.

### 5.3. Triple-axis spectrometer measurements

#### 5.3.1. Scattering by phonons and mixed modes

In order to collect additional data on the mixed excitation in other parts of the Brillouin zone, a series of constant- $\underline{Q}$  experiments along the [100] and  $[\bar{1}11]$  directions was performed by means of the triple-axis spectrometer. The crystal was mounted with the (01 $\bar{1}$ ) plane horizontal. Zinc (0002) crystals were used as monochromator and analyzer in combination with collimators of 20' (in front of the monochromator) and 30' (in front of the analyzer). The analyzer position was kept constant during each scan to realize a constant analyzer reflectivity and detector efficiency. To vary the energy transfer, the energy of the incident neutrons was changed. The irregular variations in the intensity of the incident beam as a function of neutron energy, which are connected with the detailed shape of the neutron spectrum in the reactor and the variation of the monochromator reflectivity, were eliminated by determining

the counting time by means of a monitor detector in the incident beam. Thus, the remaining variation in the counting time is only due to the efficiency of the monitor, which is a slowly varying function of the neutron energy. A possible source of spurious maxima in the recorded spectra is eliminated in this way.

The measurements were carried out both in energy loss and energy gain, in scattering configurations for which  $Q/q$ . In this case only scattering by longitudinal phonons and magnons should be observable. In most scans the frequency interval between 2 and 8 THz was investigated to detect possible additional scattering. For the determination of the frequencies of the longitudinal phonons one usually covers an interval of about 3 THz, in which case additional scattering processes may easily remain undetected.

The main part of the raw data for  $q = (\zeta, 0, 0)$  has been summarized in figures 5.3 and 5.4. Some scans in the outer part of the Brillouin zone have been omitted, because the scattering patterns change very gradually in this region. A number of scans, extended up to 10 THz, which were performed for  $\zeta \geq 0.7$  to cover the range of the longitudinal phonons, have been omitted too. In general the frequencies of the  $\Delta_1$  phonons are in good agreement with the results of Birgeneau et al. [2], as may be seen from table 5.3. Scattering by magnons could be seen in the scans at  $\zeta = 0.1$ , but the observed maxima were very broad, due to the large gradient of the magnon dispersion relation.

table 5.3.

Frequencies (in THz) of  $\Delta_1$  phonons,  $Q = (2\zeta, 0, 0)$

$\zeta$	present results		previous results [2]
	$E_o > E$	$E_o < E$	$E_o > E$
0.2	3.22	3.19	3.12 $\pm$ 0.09
0.3	4.51	4.50	4.42 $\pm$ 0.11
0.4	5.65	5.65	5.58 $\pm$ 0.12
0.5	6.66	6.66	6.54 $\pm$ 0.13
0.6	7.47	7.46	7.34 $\pm$ 0.12
0.7	7.99	8.18	7.94 $\pm$ 0.14
0.8	8.00	8.34	8.34 $\pm$ 0.13
0.9	8.36	8.55	8.56 $\pm$ 0.18
1.0	8.54	8.57	8.55 $\pm$ 0.13

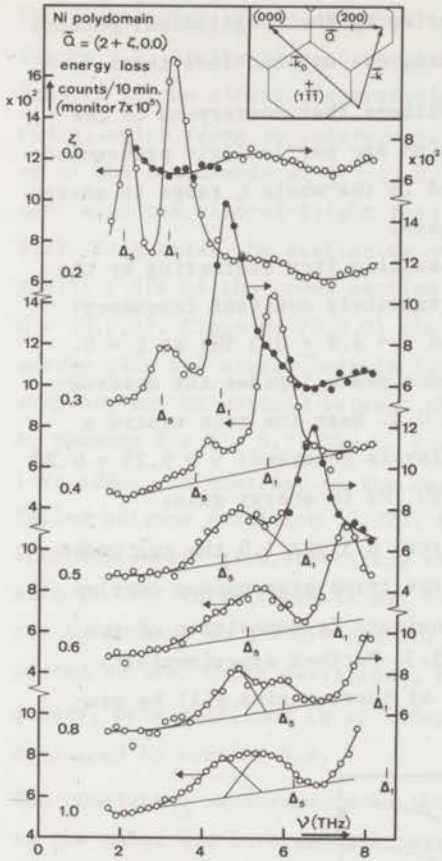


Figure 5.3.

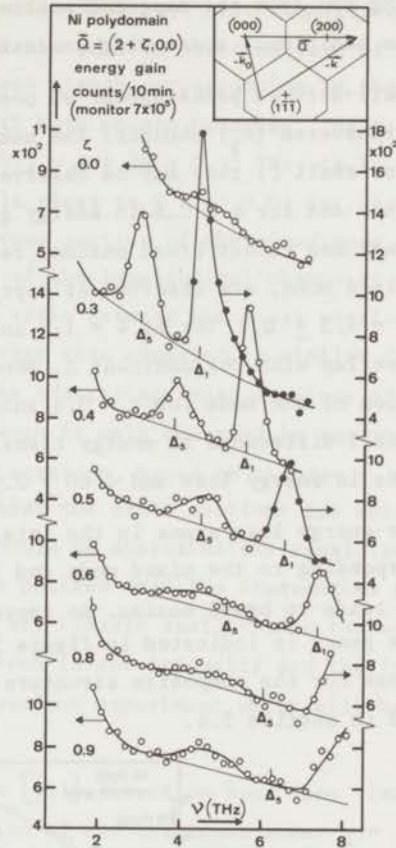


Figure 5.4.

Results of constant- $Q$  scans between 2 and 8 THz along the  $[100]$  direction, performed in energy loss (figure 5.3) and in energy gain (figure 5.4.). The frequencies indicated by  $\Delta_1$  and  $\Delta_5$  refer to the results of Birgeneau et al. [2]. Filled circles are used to distinguish overlapping spectra and arrows indicate the appropriate scale. The energy loss scan at  $\tau = 1.0$  represents the average of six separate scans. An approximate decomposition of the double peaks at  $\tau = 0.8$  and  $1.0$  has been indicated.

Turning now from the expected scattering by the longitudinal phonons to the additional scattering processes, one may conclude that:

- (a) Well-defined peaks appear at positions that correspond to the transverse ( $\Delta_5$ ) phonons. The maxima are particularly pronounced for small  $\zeta$ ; they may be observed in the whole  $\zeta$  range in energy loss and for  $\zeta \leq 0.5$  in energy gain.
- (b) Weak and rather broad maxima, resulting from scattering by the mixed mode, are observed at approximately constant frequency:  $\nu = 4.3 \pm 0.2$  THz at  $\zeta = 1.0$  and  $\nu = 4.9 \pm 0.3$  THz at  $\zeta = 0$ . Overlap with the dominant  $\Delta_1$  phonon peaks impedes the observation of the mode for  $\zeta = 0.4$  and  $0.5$ . Near the zone centre a small difference in energy transfer is observed:  $\nu = 5.25 \pm 0.20$  THz in energy loss and  $4.60 \pm 0.20$  THz in energy gain.

In the energy loss scans in the interval  $0.5 \leq \zeta \leq 1.0$  the two peaks corresponding to the mixed mode and the transverse phonon overlap, which leads to broad maxima. An approximate decomposition of two double peaks is indicated in figure 5.3. Further experimental evidence for the composite structure of these maxima will be presented in section 5.4.

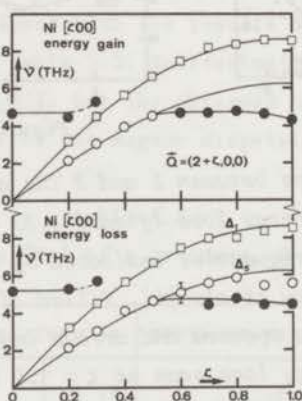


Figure 5.5.

Observed longitudinal phonons ( $\square$ ), transverse phonons ( $\circ$ ) and mixed excitations ( $\bullet$ ) along the  $[100]$  direction. The drawn curves  $\Delta_1$  and  $\Delta_5$  represent the results of Birgeneau et al. [2].

The frequencies of the observed excitations have been summarized in figure 5.5. In the present context the most interesting part of the results is the almost dispersionless branch corresponding to the mixed modes, which seems to interact with both phonon branches. The frequency of the mixed mode at  $\underline{Q} = (3,0,0)$ ,  $\nu = 4.35 \pm 0.15$  THz, is in agreement with the time-of-flight result close to  $\underline{Q} = (1,0,0)$  (cf. table 5.2). In general the scattering cross section of the mixed mode is small:  $\approx 1/6$  of the cross section of the longitudinal phonon at  $\underline{Q} = (3,0,0)$ . Close to  $(3,0,0)$  the ratio between the cross sections for energy gain and energy loss is larger than expected. A similar discrepancy may be noticed between the scattering cross sections of the  $\Delta_5$  phonons for  $\zeta \geq 0.7$ . The  $\Delta_5$  branch is only observed in energy loss scans, in contrast to the expectation, based on the detailed-balance condition (3.22), that the cross sections for energy loss and energy gain scattering should be approximately equal (see also (7.4)). Furthermore, it may be noticed that the frequencies of the  $\Delta_5$  phonons at  $\zeta = 0.9$  and  $1.0$  are clearly smaller than the expected values. These deviations, both in the intensity and the frequency, were confirmed in an independent experiment which will be discussed in section 5.4.

The constant- $Q$  measurements in the  $[\bar{1}11]$  direction have been limited to the outer and intermediate region of the Brillouin zone:  $\underline{q} = (\bar{\zeta}, \zeta, \zeta)$  with  $0.23 \leq \zeta \leq 0.5$  (cf. figure 5.6.). The average frequency of the longitudinal ( $\Lambda_1$ ) phonon at  $\zeta = 0.23$  is found to be 6.37 THz, which is in reasonable agreement with the value  $6.23 \pm 0.10$  THz derived from the results in [2] by interpolation. The additional scattering at  $\nu \approx 5$  THz is in some respects similar to that observed in the  $[\zeta 00]$  direction. The maxima recorded in energy loss close to the zone boundary are composed of contributions from the mixed mode and  $\Lambda_3$  phonons, whereas a weak single peak, due to the mixed mode, is observed in energy gain. In figure 5.7, where the observed frequencies have been plotted, one may notice some differences in comparison with figure 5.5. Owing to the large separation of the  $\Lambda_1$  and  $\Lambda_3$  branches and to the fact that the  $\Lambda_3$  branch is situated below the branch of the mixed modes, the latter may be observed in the intermediate region of the zone ( $0.2 < \zeta < 0.4$ ), where the average frequency  $\nu = 4.8 \pm 0.2$  THz is found. The results obtained in energy loss close to  $\zeta = 0.5$

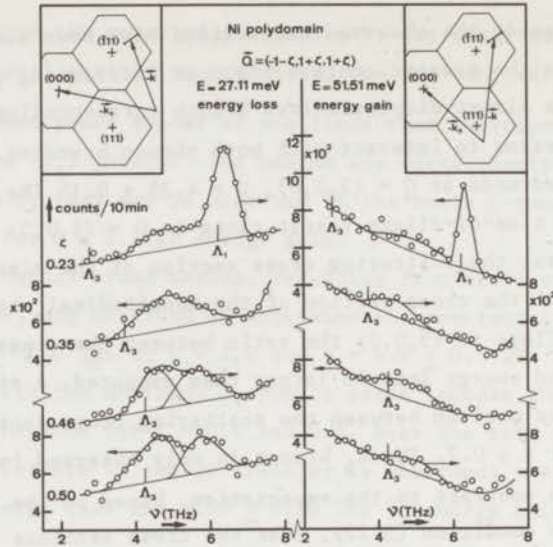


Figure 5.6.

Results of constant- $Q$  scans along the  $[\bar{1}11]$  direction in the outer part of the Brillouin zone. Energy gain and energy loss scans were performed at the same values of  $\zeta$ . An approximate decomposition of double peaks observed in energy loss has been indicated. Frequencies indicated by  $\Lambda_1$  and  $\Lambda_3$  refer to the results of Birgeneau et al. [2].

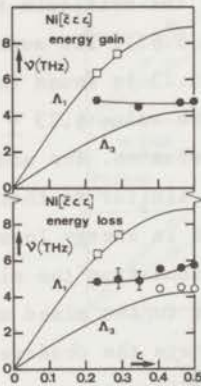


Figure 5.7.

Observed longitudinal phonons ( $\square$ ), transverse phonons ( $\circ$ ) and mixed excitations ( $\bullet$ ) along the  $[\bar{1}11]$  direction. The drawn curves  $\Lambda_1$  and  $\Lambda_3$  represent the results of Birgeneau et al. [2]. This figure contains more data than those presented in figure 5.6.

are indicative for an interference between the  $\Lambda_3$  phonons and the mixed mode, which leads to a change in the frequency of the mixed mode and, in addition, lifts the restrictions imposed by cubic symmetry on the neutron scattering by the  $\Lambda_3$  phonons.

### 5.3.2. Scattering by magnons

As mentioned earlier, the magnon dispersion relation in nickel has been determined previously by different research groups. Therefore, the present investigation of the magnons has been restricted to the relatively small frequency interval between 3 and 6 THz, close to the crossing of the magnon dispersion relation and the flat branch of mixed modes.  $Q$  was chosen along the  $[100]$  direction.

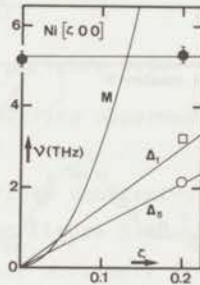


Figure 5.8.

Detail of the dispersion relations close to the zone centre. The data points are taken from figure 5.5, energy loss.  $M$  represents the magnon dispersion relation  $h\nu = Dq^2$  for  $D = 400 \text{ meV}\text{\AA}^2$  [7], the initial slope of the phonon branches  $\Delta_1$  and  $\Delta_5$  has been calculated from the elastic constants  $c_{11} = 2.46 \times 10^{12}$  and  $c_{44} = 1.22 \times 10^{12} \text{ dyne/cm}^2$ .

Figure 5.8 shows the  $(\nu, q)$  region of interest and the dispersion relations for phonons, magnons and mixed modes. The aim of the measurements was to investigate whether there is an interaction between the magnons and the mixed modes. If this interaction exists, one may expect a perturbation of the magnon dispersion relation near the crossing at  $\nu = 5.25$  THz (the frequency of the mixed mode in energy loss).

In view of the large gradient of the magnon dispersion relation,

constant- $\nu$  scans are clearly more favourable for the investigation of magnons than constant- $Q$  scans. To increase the intensity the collimation was relaxed: collimators of 40' and 60' were installed in front of the monochromator and analyzer crystals, respectively. A scattering configuration was chosen where focusing of neutron-magnon scattering is realized, namely energy loss scattering in the configuration shown in figure 4.2 with  $Q = (2-\tau, 0, 0)$ . Thus, the magnon peaks were well-defined in spite of the larger collimator opening angles. In order to obtain a reasonable statistical accuracy for the magnon scattering, counting times of about one hour at each spectrometer setting were required. However, in extended counting periods long-term variations in the background intensity may lead to spurious maxima, and the measurements were therefore carried out in 6 subsequent identical 8 minutes scans, the results of which were added.

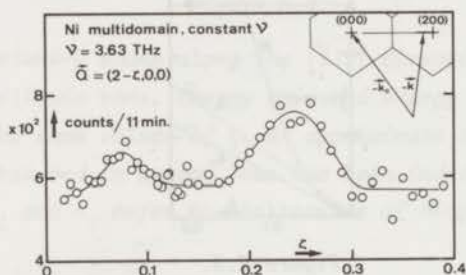


Figure 5.9.

Comparison of the scattering cross sections of a magnon ( $\tau = 0.076$ ) and a  $\Delta_1$  phonon ( $\tau = 0.246$ ) in a constant- $\nu$  scan.

The relative magnitude of neutron-magnon and neutron-phonon scattering is illustrated in figure 5.9. In this configuration with small  $|Q|$  the magnon scattering is favoured by the relatively large value of  $F(Q)^2$ , whereas the scattering by the longitudinal phonons is depressed by the relatively small value of the polarization factor  $(\xi \cdot Q)^2 = Q^2$ . In constant- $\nu$  scans for  $\nu < 3$  THz there is an overlap of the two maxima and the observation of the magnon peak is hampered by the dominating phonon peak.



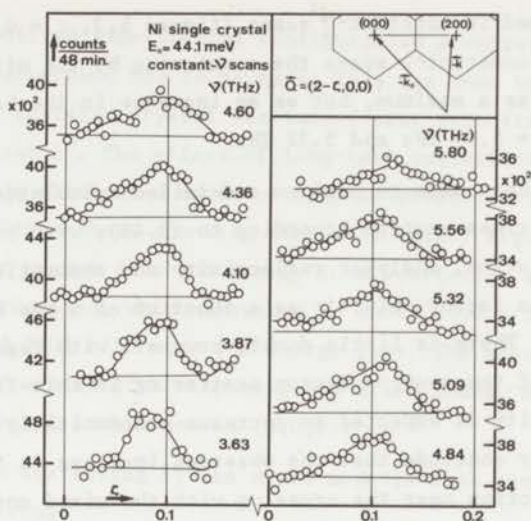


Figure 5.10.

*Neutron-magnon scattering observed in constant- $\nu$  scans.*

The complete set of energy-loss constant- $\nu$  scans between  $\nu = 3.63$  THz and 5.80 THz is collected in figure 5.10. The maxima observed between  $\nu = 4.10$  THz and 5.56 THz are obviously distorted; they are broader and higher than one would expect from interpolation between the scans at  $\nu = 3.87$  THz and 5.80 THz. This anomalous behaviour may be more clearly demonstrated by plotting the integrated intensity in the peaks as a function of frequency (see figure 5.11). It should be emphasized that the increase in intensity from neutron-magnon scattering observed here, is superposed on top of the intensity due to the mixed mode at  $\nu \approx 5$  THz,

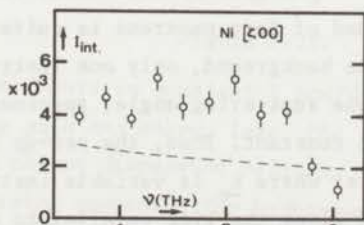


Figure 5.11.

*Integrated intensity in the magnon peaks as a function of frequency. The dotted line indicates the variation of the factor  $\langle n(\nu)+1 \rangle$  in the cross section, the scale factor being adjusted to the data point at  $\nu = 5.80$  THz.*

that was observed in constant- $Q$  scans (figure 5.3,  $\zeta = 0.0$  and  $0.2$ ). In the present constant- $\nu$  scans the scattering by the mixed mode is not observable as a maximum, but as an increase in the background in the scans at  $\nu = 5.09$  THz and  $5.32$  THz.

No attempt has been made to perform a detailed calculation of the neutron-magnon cross section according to (3.44), with proper corrections for resolution, analyzer reflectivity and absorption. Only the variation of the factor  $\langle n(\nu)+1 \rangle$  as a function of  $\nu$  has been indicated in figure 5.11. There is little doubt, however, with regard to the general trend of the neutron-magnon scattering in this frequency interval: the intensity is expected to decrease monotonically for increasing  $\nu$ . Hence one may conclude that the observed increase in the neutron-magnon cross section near the crossing with the mixed mode branch at  $\nu = 5$  THz is probably due to the interaction between the magnons and the mixed modes.

#### 5.4. Comparison of time-of-flight and triple-axis measurements

There is a clear difference between the neutron spectra observed in energy loss with the time-of-flight spectrometer close to  $Q = (1,0,0)$  (cf. figure 5.2) and with the triple-axis spectrometer at  $Q = (3,0,0)$  (cf. figure 5.3). However, agreement for the frequency of the mixed mode could be obtained by decomposition of the double maximum in the triple-axis scan into contributions from the mixed mode and  $\Delta_5$  phonons. In this section we shall present the results of a separate triple-axis experiment close to  $(1,0,0)$ , which was performed in order to make a comparison between the two experimental techniques for the same  $Q$ . A constant- $Q$  scan at  $Q = (1,0,0)$  would have to cover a range of small scattering angles, where the background of fast neutrons is quite large. To avoid the disturbing influence of the background, only one instrumental parameter,  $\theta_M$ , was varied, while the scattering angle, specimen orientation and analyzer setting were kept constant. Thus, the set-up becomes similar to a time-of-flight spectrometer where  $k_o$  is variable instead of  $k$ . In  $Q$ -space a scan is performed along the line parallel to  $k_o$  passing through  $(1,0,0)$ , as shown in figure 5.12. In order to compare the cross sections in  $(1,0,0)$  and  $(3,0,0)$  the value for  $k$  was chosen equal to the value used in the scan at  $(3,0,0)$ .

Even in the modified experimental configuration a correction for the fast-neutron background had to be made. This was done by repeating each scan while the analyzer crystal was turned away from its reflection position by about  $5^\circ$ . The effect of long-term variations in the background level was eliminated as accurately as possible by repeating each scan 5 times with a short counting time ( $\approx 10$  min.) Figure 5.12 shows the results for energy gain and energy loss scattering after subtraction of the background, which amounted to about 2200 n/50 min. for energy gain and 2900 n/50 min. for energy loss. The spectra show maxima that may be correlated with + phonons and mixed modes, and are in agreement with the results obtained in (3,0,0):

(a) Energy gain scattering by the mixed mode is weak compared with energy loss scattering.

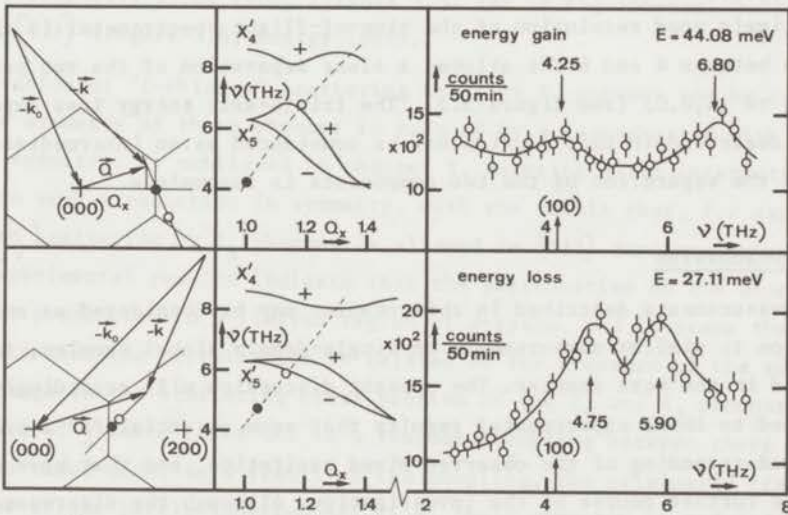


Figure 5.12.

Triple-axis experiments in constant- $\underline{k}$  configuration close to (1,0,0), performed in energy gain and energy loss. The figure contains the scanned path in  $\underline{Q}$ -space, the phonon dispersion relation and energy-transfer curve, and the observed spectra corrected for background. The low-frequency peak is due to the mixed mode close to (1,0,0). Frequencies and wave vectors corresponding to the observed peaks are indicated in the  $\nu$ - $Q_x$  graph and in  $\underline{Q}$ -space, respectively.

- (b) The scattering by the nearly transverse + phonon close to (1,0,0) is much stronger than expected; moreover, the phonon frequency is smaller than expected (5.90 THz instead of 6.25 THz).

It seems likely that the difference between the time-of-flight and triple-axis results may be explained as a resolution effect. Two different scattering processes should be distinguished. First, transverse phonons are observable in and close to (1,0,0) and (3,0,0) in  $Q$ -space, in spite of the fact that scattering by purely transverse phonons is forbidden in these points ( $\xi \cdot Q = 0$ ) and very weak in the direct neighbourhood. Secondly, scattering by the mixed excitation is observed, and it will depend on the experimental configuration whether the scattering by the mixed mode can be separated from the neutron-phonon scattering.

The resolution of the triple-axis spectrometer in the constant- $Q$  scan in (3,0,0) was obviously not sufficient to achieve this, whereas the relatively good resolution of the time-of-flight spectrometer in the range between 4 and 6 THz allowed a clear separation of the two peaks close to (1,0,0) (see figure 5.2). The triple-axis energy loss experiment described in this section may be considered as an intermediate case where the separation of the two components is incomplete.

### 5.5. Discussion

The measurements described in this chapter may be considered as an introduction to similar measurements on single-domain nickel samples, to be reported in the next chapter. The present discussion will accordingly be limited to those experimental results that seem essential for a preliminary understanding of the observed mixed excitation, and that have determined the further course of the investigation. Although the discrepancy between energy gain and energy loss scattering stands out as a challenging problem, the discussion on this issue will be postponed (see section 7.4). The main subject in this section will be the observation of "forbidden" scattering by  $\Delta_5$  and  $\Lambda_3$  phonons in relation to the existence of the mixed modes.

It has been stated in section 5.3.1 that in a scattering configuration where  $Q // q$  only scattering by longitudinal phonons and magnons should be observable. Actually, the scattering by transverse phonons is not strictly forbidden, because the observation is not restricted to a single point  $Q$ ,

but to a 4-dimensional region in  $(\omega, Q)$ -space defined by the resolution ellipsoid. Close to the zone centre the resolution ellipsoid allows the observation of phonons with a relatively large range of propagation directions  $\underline{q}/|q|$ . Since the polarization vector  $\underline{\xi}$  of the transverse phonons is not perpendicular to  $\underline{Q}$  if  $\underline{q}$  is not parallel with  $\underline{Q}$ , neutron scattering by transverse phonons will be observable for small values of  $\zeta$  (cf. figures 5.3 and 5.4).

However, the observation of transverse phonons in energy loss close to the zone boundaries cannot be explained by means of resolution arguments. The angular spread in the wave vector  $\underline{q}$  connected with the size of the resolution ellipsoid will decrease as  $\zeta$  increases and therefore the intensity of the transverse-phonon peaks is expected to decrease continuously with increasing  $\zeta$ . This is not the case, as may be seen from the scans in the interval  $0.4 \leq \zeta \leq 1.0$  along  $[100]$  (figure 5.3) and in the interval  $0.23 \leq \zeta \leq 0.50$  along  $[\bar{1}11]$  (figure 5.6, energy loss).

Observation of "forbidden" scattering by  $\Delta_5$  or  $\Lambda_3$  phonons may be expected if the symmetry of these phonons is reduced by a perturbation with non-cubic symmetry. As mentioned in chapter I, magnetoelastic interaction may lead to such a reduction in symmetry, with the result that, for example, neutron scattering by  $\Delta_5$  phonons is allowed in  $[111]$  domains. However, the experimental results indicate that the perturbation of the phonons is most pronounced in a limited region of  $\underline{q}$ -space, and it seems therefore probable that the perturbation is related to the presence of the mixed mode. The change in the scattering cross section of the  $\Delta_5$  and  $\Lambda_3$  phonons as a function of  $\underline{q}$  seems to be due to a resonant coupling between these phonons and the mixed mode. As a result of the coupling, the originally transverse phonons become partly longitudinal (i.e. their symmetry is reduced), and may therefore be observed in the present scattering configuration. According to this interpretation the scattering by the perturbed, partly longitudinal phonons should reach a maximum at the crossing (or the point of closest approach) of the dispersion relations of the phonons and the mixed modes. In the  $[100]$  direction the crossing occurs at  $\zeta = 0.55$ , whereas the closest approach in the  $[\bar{1}11]$  direction is at the zone boundary,  $\zeta = 0.50$ . From figure 5.6 it is seen that the intensity due to the perturbed  $\Lambda_3$  phonons is indeed largest near the zone boundary. Along the  $[100]$  direction the frequency difference between the  $\Delta_5$  phonons and the mixed modes is small

in a large range of  $\zeta$  ( $0.5 \ll \zeta \ll 1.0$ ) and therefore the variation in the scattering by the perturbed phonons is less pronounced than in the  $[111]$  direction.

One may conclude from the observed perturbation of the phonons, in particular from the change in the polarization vector, that the interaction with the additional mode leads to a lowering of the phonon symmetry. The most probable explanation for this effect seems that the mode has magnetic properties. This assumption is supported by the fact that also the magnons are perturbed near the crossing with the additional branch. The property of the new mode to interact both with magnons and phonons may be considered as an indication that the mode itself is a mixed excitation, in which electronic (i.e. magnetic) and vibrational properties are combined.

The increase in the neutron-magnon scattering in the frequency interval between 4.10 and 5.50 THz is probably a consequence of the mixed character of the excitation. Due to the interference between the mixed mode and the magnons, the latter will acquire some lattice-vibrational properties. Since the nuclear scattering near  $(2,0,0)$  is much larger than the magnetic scattering, the admixture of a vibrational component will lead to an increase in the cross section of the perturbed magnons.

Summarizing the preceding discussion, one arrives at the following preliminary description of the properties of the mixed excitation. The excitation is observable in different regions of  $Q$ -space and may be described by a specific dispersion relation. However, the variation in the frequency is small in the investigated parts of the reciprocal lattice, and in this respect the excitation shows some resemblance with a localized excitation or an optical phonon. From its interaction with the transverse phonons and the magnons one may probably conclude that the excitation is a mixed electronic-vibrational mode.

CHAPTER VI

INVESTIGATION OF NICKEL SINGLE-DOMAIN SINGLE CRYSTALS

6.1. A crucial experiment

From the triple-axis experiments on the multidomain nickel crystal some indications for the magnetic character of the mixed excitation could be deduced. Near the zone centre the mixed mode interacts with the magnons, and near the zone boundaries the interaction between this mode and the transverse phonons leads to a lowering of the symmetry of the phonons.

More direct evidence for the magnetic properties of the mixed excitation near the zone boundary was obtained by means of a time-of-flight experiment on a single domain. The same specimen that was used previously was mounted with the  $[01\bar{1}]$  direction vertical, magnetized in the horizontal plane along the  $[\bar{1}\bar{1}\bar{1}]$  direction in an external magnetic field of 9075 Oe, and the time-of-flight spectrometer was set to observe the mixed excitation in energy loss at  $\underline{Q} = (1,0,0)$ . The scattering configuration is therefore the same as in one of the previous time-of-flight experiments (cf. figure 5.2), and the spectrum recorded without external field shows indeed the additional peak centred at channel 99. Strikingly enough, this peak is strongly reduced when the crystal is magnetized along the  $[\bar{1}\bar{1}\bar{1}]$  direction, as shown in figure 6.1. The small bump that remains was also observed in the spectrum of polycrystalline nickel, and is probably due to incoherent one-phonon scattering. A numerical analysis according to the normalization procedure used in section 5.2 yields an integrated intensity in the "maximum" of  $-160 \pm 380$  for the  $[\bar{1}\bar{1}\bar{1}]$  domain relative to the polycrystalline specimen (cf. table 5.2 for the multidomain crystal).

The result of the present experiment confirms the assumption that the excitation is of magnetic origin. On the other hand, the total disappearance of the peak was not expected and in connection with this a number of questions arise. Since this experiment has been decisive for the further course of the investigation, a rather detailed discussion of the result is given below.

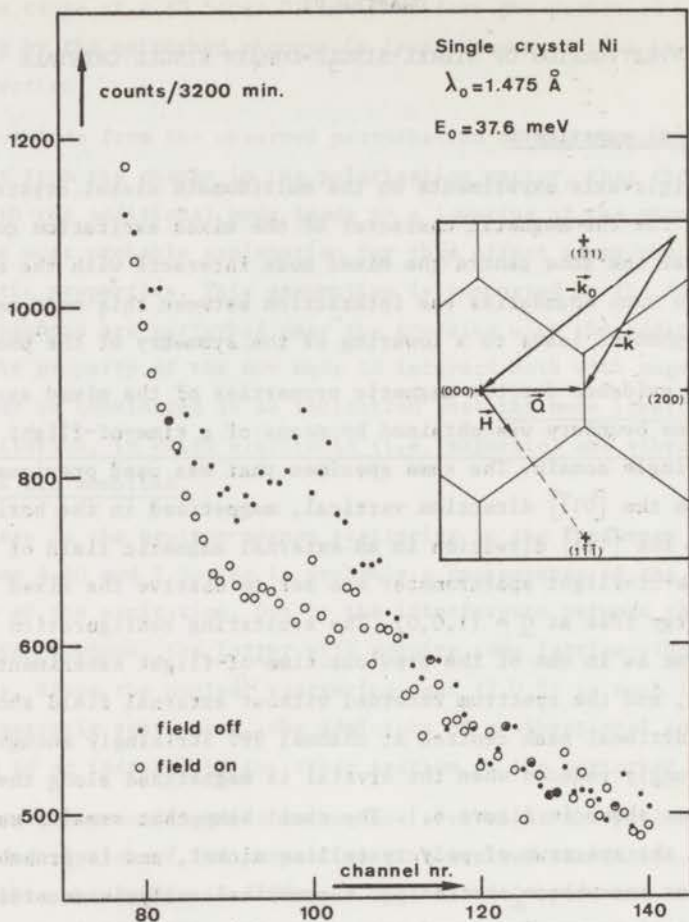


Figure 6.1.

Comparison of the scattering by the mixed excitation in a multidomain and a single domain. Channel nr. 100 corresponds to an energy transfer of 17.5 meV ( $\nu = 4.23 \text{ THz}$ ) at  $\underline{Q} = (1,0,0)$ .

A possible explanation for the disappearance of the additional peak might be that the energy of the excitation is changed to such an extent, that the peak is shifted out of the observation range of the spectrometer. However, a change in the magnetic field direction of  $10^\circ$ ,  $20^\circ$  and  $28^\circ$  in the horizontal plane, from  $[\bar{1}\bar{1}\bar{1}]$  towards  $[100]$ , leads to the conclusion that this explanation can be ruled out: the peak shows up with increasing intensity at the same position where it was observed without field. One may therefore



conclude that the scattering cross section depends on the magnetization direction. However, the influence of the magnetization cannot be ascribed to factors like  $\{1+(\underline{e}\cdot\underline{m})^2\}$  or  $\{1-(\underline{e}\cdot\underline{m})^2\}$ , present in the cross sections for magnon scattering (3.44) and magnetovibrational scattering (3.31), respectively. In the present configuration,  $\underline{M} // [\bar{1}\bar{1}\bar{1}]$  and  $\underline{Q} = (1,0,0)$ , the field dependent term  $(\underline{e}\cdot\underline{m})^2$  has the value 1/3 and the cross sections (3.31) and (3.44) are different from zero. Consequently, the scattering must be described by some other mechanism. A detailed discussion of the peculiar behaviour of the scattering cross section will be given in section 7.3.

Another conclusion from the present experiment is, that the additional scattering in (1,0,0) from the multidomain crystal is probably due to  $[\bar{1}10]$  or  $[\bar{1}00]$  domains, because all  $[\bar{1}11]$  domains are equivalent with respect to  $\underline{Q} = (1,0,0)$  and are therefore expected to yield the same zero result. At room temperature the  $[\bar{1}11]$  directions are the easy magnetization directions, but the magnetic anisotropy is known to be small  $|89,90|$  and therefore  $[\bar{1}10]$  and  $[\bar{1}00]$  domains are likely to be present in the multidomain crystal, especially as closure domains near the surface. Moreover, one should take into account that the neutron beam is strongly attenuated on its way through the large cylindrical sample: the transmission through 3 cm nickel is only 0.3%. Hence the bulk of the sample contributes only little to the observed scattering, and one observes mainly the surface layer of the crystal, where the path of the neutrons through the sample is short. In this way one may understand why the additional scattering is clearly observed in the multidomain crystal, but not in the  $[\bar{1}\bar{1}\bar{1}]$  single domain.

To this point the discussion has been limited to the scattering in one particular point in  $\underline{Q}$ -space. By consideration of continuity, however, the same arguments may be used for the triple-axis experiments along  $[\bar{1}00]$  and  $[\bar{1}\bar{1}\bar{1}]$  on the multidomain crystal. The results summarized in figures 5.3 - 5.7 should then be interpreted as a superposition of separate contributions, each being due to a particular domain type. On the basis of the time-of-flight experiment on the  $[\bar{1}\bar{1}\bar{1}]$  domain one might expect, for example, that the additional branch along  $[\bar{1}00]$  (cf. figure 5.5) is not observable in  $[\bar{1}\bar{1}\bar{1}]$  domains.

### 6.2. Choice of single domain samples

In order to start a more systematic investigation of the mixed excitation under different magnetic conditions, four new samples were prepared. Platelets with dimensions  $5 \times 25 \times 25 \text{ mm}^3$  were cut by means of spark erosion from a large single crystal, supplied by Metals Research, Cambridge. The long edges were oriented along directions of high symmetry, so that samples of the types  $[110]-[001]$ ,  $[110]-[\bar{1}10]$  and  $[110]-[\bar{1}11]$  were obtained (cf. table 6.1). During the measurements a particular sample was mounted in the

Table 6.1.

*Crystals used as single domain*

crystal nr.	orientation
1, 2	$[110]-[001]$
3	$[110]-[\bar{1}11]$
4	$[110]-[\bar{1}10]$

25 mm gap of a C-shaped permanent magnet giving a field strength of  $3050 \pm 30 \text{ Oe}$ , which is sufficient to reach magnetic saturation at room temperature, even for the hard magnetization direction  $[001]$ . The field direction could be chosen either horizontally i.e. in the scattering plane, or vertically.

Although it was concluded in section 6.1 that the scattering cross section of the mixed mode with  $\underline{q} = (1,0,0)$  is a function of the magnetization direction, it is not evident that the mode actually has a magnetic moment. If the spin  $S^z$  of the mode is zero, it should be classified according to the irreducible representations of the pseudo-magnetic point group  $G_o^{+M}(\underline{q})$ . This will be the case if the mode corresponds to an electron excitation within the same spin band. If, on the other hand, the mode has a spin  $S^z$  equal to  $+1$  or  $-1$ , which is the case for electron transitions between states with different spin, it must transform as one of the irreducible representations of the unitary subgroup  $G_o^M(\underline{q})$  of the magnetic point group  $M(\underline{q})$  (these groups have been defined in section 2.2). The latter of these two possibilities was chosen as basis for the selection of the scattering configuration in the experiments described below. The measurements were restricted to the  $[100]$ ,  $[110]$  and  $[111]$  directions in single domains,

magnetized along one of these three high-symmetry directions.

Table 6.2.

Magnetic point group  $M(\underline{q})$  for symmetry directions in single domains<sup>\*</sup>)

$\underline{M} // [001]$			$\underline{M} // [110]$			$\underline{M} // [111]$		
point line	$\underline{q}$	$M(\underline{q})$	point line	$\underline{q}$	$M(\underline{q})$	point line	$\underline{q}$	$M(\underline{q})$
$X^1$	(1,0,0)	$D_{2h}(C_{2h})$	$X^1$	(1,0,0)	$C_{2h}(C_1)$	X	(0,1,0)	$C_{2h}(C_1)$
$X^2$	(0,0,1)	$D_{4h}(C_{4h})$	$X^2$	(0,0,1)	$D_{2h}(C_{2h})$			
$\Delta^1$	( $\tau$ ,0,0)	$C_{2v}(C_s)$	$\Delta^1$	( $\tau$ ,0,0)	$C_2(C_1)$	$\Delta$	(0, $\tau$ ,0)	$C_2(C_1)$
$\Delta^2$	(0,0, $\tau$ )	$D_4(C_4)$	$\Delta^2$	(0,0, $\tau$ )	$C_{2v}(C_s)$			
$\Lambda$	( $\tau$ , $\tau$ , $\tau$ )	$C_2(C_1)$	$\Lambda^1$	( $\tau$ , $\tau$ , $\tau$ )	$C_2(C_1)$	$\Lambda^1$	( $\tau$ , $\tau$ , $\tau$ )	$D_3(C_3)$
			$\Lambda^2$	( $\bar{\tau}$ , $\tau$ , $\tau$ )	$(C_s)$	$\Lambda^2$	( $\bar{\tau}$ , $\tau$ , $\tau$ )	$C_2(C_1)$
$\Sigma^1$	( $\tau$ , $\tau$ ,0)	$C_{2v}(C_s)$	$\Sigma^1$	( $\tau$ , $\tau$ ,0)	$D_2(C_2)$	$\Sigma^1$	( $\tau$ , $\tau$ ,0)	$C_2(C_1)$
$\Sigma^2$	(0, $\tau$ , $\tau$ )	$C_2(C_1)$	$\Sigma^2$	( $\bar{\tau}$ , $\tau$ ,0)	$C_{2v}(C_s)$	$\Sigma^2$	( $\bar{\tau}$ , $\tau$ ,0)	$C_s(C_1)$
			$\Sigma^3$	(0, $\tau$ , $\tau$ )	$(C_1)$			

<sup>\*</sup>) The notation for the symmetry lines and points has been introduced by Cracknell [36]. Distinction is made between nonequivalent directions, while the connection with the notation of Bouckaert et al. for the cubic crystal [44] is retained. The point group in parantheses is the unitary subgroup  $G_O^M(\underline{q})$  of  $M(\underline{q})$ . For  $\Lambda^2$  and  $\Sigma^3$  in the [110] domain there are no anti-unitary elements. The magnetic point group for  $\Delta^2$  in the [110] domain has been treated as an example in section 2.2.

In spite of this restriction, however, the number of magnetically nonequivalent combinations of  $\underline{M}$  and  $\underline{q}$  is large. This is due to the fact that vectors  $\underline{q}$  that are equivalent in a crystal with cubic symmetry, will become nonequivalent in a ferromagnetic single domain, which has a lower symmetry. The nonequivalent combinations of  $\underline{M}$  and  $\underline{q}$ , relevant to the present investigation, are listed in table 6.2; complete tables may be found in [36]. The measurements to be described in this chapter cover only a limited number of these combinations. The time-of-flight experiments were aimed

at the observation of the mixed mode in or close to the points (1,0,0) and (0,0,1) in different domains, whereas the experiments with the triple-axis spectrometer were limited to the directions  $\Delta^2 = (0,0,\zeta)$ ,  $\Sigma^2 = (\bar{\zeta},\zeta,0)$  and  $\Lambda^2 = (\bar{\zeta},\zeta,\zeta)$  in a [110] domain. The results are presented in sections 6.3 and 6.4, respectively.

### 6.3. Time-of-flight measurements on [001], [110] and [111] domains

The time-of-flight experiments on single domains were intended to confirm and to extend the experiment described in section 6.1. The first aim was to check the assumption that the scattering by the mixed mode at  $Q = (1,0,0)$  should be due to [001] or/and [110] domains. In addition, a search was made for scattering in points like (0,1,1) and (1,1,0), which are equivalent to the points (1,0,0) and (0,0,1) because they are connected by translations over a reciprocal lattice vector. A complete list of the various points X and the investigated cases is given in the tables 6.3, 6.4 and 6.5. Shortly before the experiments on single domains were started, the new rotor with the double slit system was put into operation. Due to the more efficient use of the incident beam, the measuring time could usually be kept within the practical limit of 48 hours, in spite of the small volume of the samples. Apart from a change in the delay time from 384  $\mu$ s to 0  $\mu$ s, which caused a shift of 48 channels in the spectra, and a slight change in the energy of the incident neutrons to  $E_0 = 36.4$  meV, the instrumental parameters were the same as before (cf. section 5.2).

Table 6.3.

Experimental results for points  $X^1$  and  $X^2$  in a [001] domain

	$X^2$	$X^1$	$X^2$	$X^1$
$M/[001]$	(0,0,1)* (0,0, $\bar{1}$ )	(1,0,0)* ( $\bar{1}$ ,0,0)* (0,1,0) (0, $\bar{1}$ ,0)	(1,1,0)* ( $\bar{1}$ , $\bar{1}$ ,0) (1, $\bar{1}$ ,0) ( $\bar{1}$ ,1,0)	(0,1,1)* (1,0,1) (0, $\bar{1}$ , $\bar{1}$ ) ( $\bar{1}$ ,0, $\bar{1}$ ) (0,1, $\bar{1}$ ) (1,0, $\bar{1}$ ) (0, $\bar{1}$ ,1) ( $\bar{1}$ ,0,1)
investigated	yes	yes	yes	yes
crystal nr.	2	1	1	1
orientation $\underline{M}$	hor.	vert.	vert.	hor.
mixed mode observed	yes	yes	no	no

\* ) Investigated points X.

Table 6.4.

Experimental results for points  $X^2$  in a  $[110]$  domain

	$X^2$	$X^1$	$X^2$	$X^1$
$\underline{M} // [110]$	$(0,0,1)^{**}$	$(1,0,0)$	$(1,1,0)$	$(0,1,1)$ $(1,0,1)$
	$(0,0,\bar{1})$	$(\bar{1},0,0)$	$(\bar{1},\bar{1},0)$	$(0,\bar{1},\bar{1})$ $(\bar{1},0,\bar{1})$
		$(0,1,0)$	$(1,\bar{1},0)^{**}$	$(0,1,\bar{1})$ $(1,0,\bar{1})$
		$(0,\bar{1},0)$	$(\bar{1},1,0)$	$(0,\bar{1},1)$ $(\bar{1},0,1)$
investigated	yes	no*	yes	no*
crystal nr.	1,2		3,4	
orientation $\underline{M}$	vert.		vert.	
mixed mode observed	yes		no	

\*) These cases have been investigated by means of a different set-up where the C-magnet with the sample was mounted in a cradle which could be rotated about a horizontal axis. The results have not been used, because it is not certain that the field was sufficiently strong to reach saturation.

\*\*\*) Investigated points X. Table 6.5.

Experimental results for points X in a  $[11\bar{1}]$  domain

	X	X	X
$\underline{M} // [11\bar{1}]$	$(1,0,0)$	$(0,1,1)^*$	$(0,1,\bar{1})^*$
	$(\bar{1},0,0)$	$(0,\bar{1},\bar{1})$	$(0,\bar{1},1)$
	$(0,1,0)$	$(1,0,1)$	$(1,0,\bar{1})$
	$(0,\bar{1},0)$	$(\bar{1},0,\bar{1})$	$(\bar{1},0,1)$
	$(0,0,1)^*$	$(1,1,0)$	$(1,\bar{1},0)$
	$(0,0,\bar{1})$	$(\bar{1},\bar{1},0)$	$(\bar{1},1,0)$
investigated	yes	yes	yes
crystal nr.	3	3	3
orientation $\underline{M}$	hor.	hor.	vert.
mixed mode observed	no	no	no

\*) Investigated points X

In most cases only one point X from each column in the three tables was investigated. As may be seen from the tables, four measurements were performed close to the points (0,0,1) and (1,0,0). The results are found to be in agreement with the preliminary conclusion in section 6.1: for a [111] domain the additional peak is absent or at most very weak, whereas scattering at about 4.0 THz is observed in [110] and [001] domains. In figure 6.2 the relevant part of the spectra has been plotted. The position of the additional maximum (channel 148) is in agreement with the previous measurements. To estimate the intensity in the maxima, the background was subtracted and the remaining spectra normalized to an integrated intensity of  $199.1 \times 10^3$  counts in the elastic incoherent peak. Next, the normalized spectrum for the [111] domain was subtracted from the three other spectra, and finally the integrated intensities in the maxima were determined (see table 6.6). The intensity in the point (0,0,1) for a [001] domain is found to be of the same magnitude as the intensity observed in the same point for the multidomain crystal.

Table 6.6.

Comparison of intensities in the 4 THz peaks

<u>M</u>	<u>Q</u>	integrated intensity
[001]	(0,0,1)	2150 $\pm$ 450
[001]	(1,0,0)	700 $\pm$ 280
[110]	(0,0,1)	1000 $\pm$ 290
[111]	(0,0,1)	0 *)
multi-domain	(0,0,1)	2650 $\pm$ 450 **)

\*) Spectrum used as reference.

\*\* ) Value taken from table 5.2.

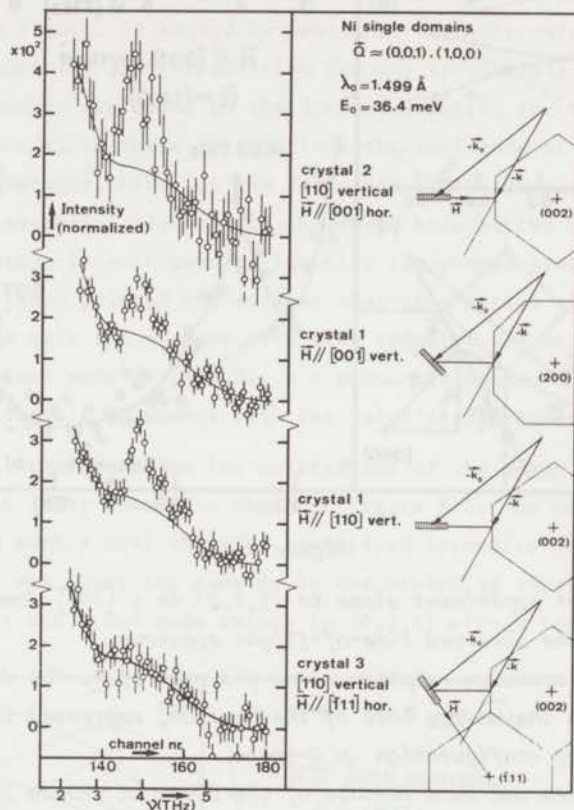


Figure 6.2.

Scattering by the mixed excitation in four different single domains. The normalization procedure is described in the text. The drawn curves in the spectra are identical and represent the "background" due to incoherent scattering.

In table 6.3 the points  $X^1$  (or  $X^2$ ) listed in different columns are equivalent because they are transformed into each other by one of the translations  $\underline{t} = (1,1,1)$ ,  $(\bar{1},1,1)$ , etc. Since the properties of an arbitrary excitation are invariant under these translations, the mixed mode has, for example, the same energy in the points  $X^1 = (0,1,1)$  and  $(1,0,0)$ . Moreover, its eigenfunction transforms according to the same irreducible representation of the same point group  $G_O^M(\underline{q})$  in both points. However, the scattering cross section of the mode is not necessarily the same in these points, because the selection rule for neutron scattering

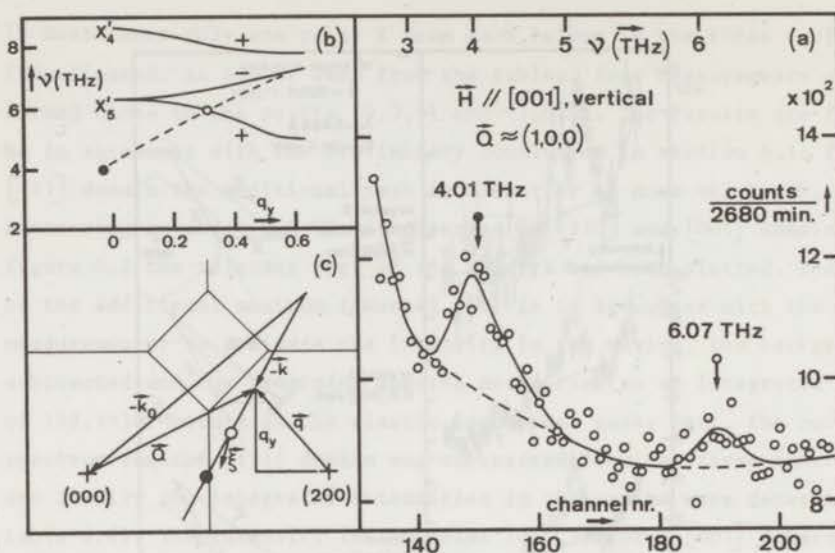


Figure 6.3.

Time-of-flight experiment close to  $(1,0,0)$  in a  $[001]$  domain.

(a) Part of the observed time-of-flight spectrum.

(b) Phonon dispersion relation along the path of  $\vec{k}$ . The dotted curve indicates the energy loss of the neutron, expressed in THz.

(c) Scattering configuration in  $\vec{Q}$ -space.

The frequencies and wave vectors of the observed phonon (o) and mixed mode (●) are plotted in (b) and (c). Moreover, the calculated polarization vector  $\vec{\xi}$  of the phonon is drawn in (c).

is based on the point group of the scattering vector  $\underline{Q}$ ,  $G_o^M(\underline{Q})$  (cf. section 3.4.3). Due to the fact that  $G_o^M(\underline{Q})$  does not contain elements that transform  $\underline{Q}$  into  $\underline{Q}+\underline{\tau}$ , the point groups  $G_o^M(\underline{Q}_1)$  and  $G_o^M(\underline{Q}_2)$  of the scattering vectors  $\underline{Q}_1$  and  $\underline{Q}_2 = \underline{Q}_1+\underline{\tau}$  are in general different.

As shown in the tables 6.3 and 6.4, different cross sections are observed for three pairs of equivalent wave vectors  $\underline{q}$ , corresponding to points  $X^1$  and  $X^2$  in a  $[001]$  domain and  $X^2$  in a  $[110]$  domain. For each pair the mixed mode is observed at  $\underline{Q} = (0,0,1)$  or  $(1,0,0)$ , but not at  $\underline{Q} = (1,\bar{1},0)$  or  $(0,1,1)$ . To illustrate this difference, the experimental results for the points  $X^1$  in a  $[001]$  domain have been summarized in figures 6.3 and 6.4. The experiment close to  $\underline{Q} = (1,0,0)$ , shown in figure 6.3, has been presented



earlier in less detail (cf. figure 6.2). The experimental configuration is given in the figure. It should be mentioned that the calculation of the phonon frequencies and the notation for the irreducible representations of the phonons are based on the dynamical matrix for the cubic crystal. In other words, in these calculations the influence of magnetic effects, like magnetostriction, on the frequency of the phonons is neglected. This is not an essential restriction, however, because the calculated phonon dispersion relation is only used to identify the phonon peaks in the observed spectra. It has been pointed out earlier that in a mirror plane of the reciprocal lattice only the phonons with even symmetry are observable. In addition to the mixed mode in  $(1,0,0)$ , a  $+$  phonon is observed at  $\nu = 6.1$  THz, which is in reasonable agreement with the calculated frequency  $\nu = 5.95$  THz.

The experimental configuration for observation of the mixed mode at  $\underline{Q} = (0,1,1)$  in a  $[001]$  domain is shown in figure 6.4. The measuring time was adjusted in such a way, that the integrated intensity in the elastic incoherent peak was about the same as in the preceding experiment. In spite of the fact that the mixed mode exists in  $(0,1,1)$  with a frequency of 4.0 THz

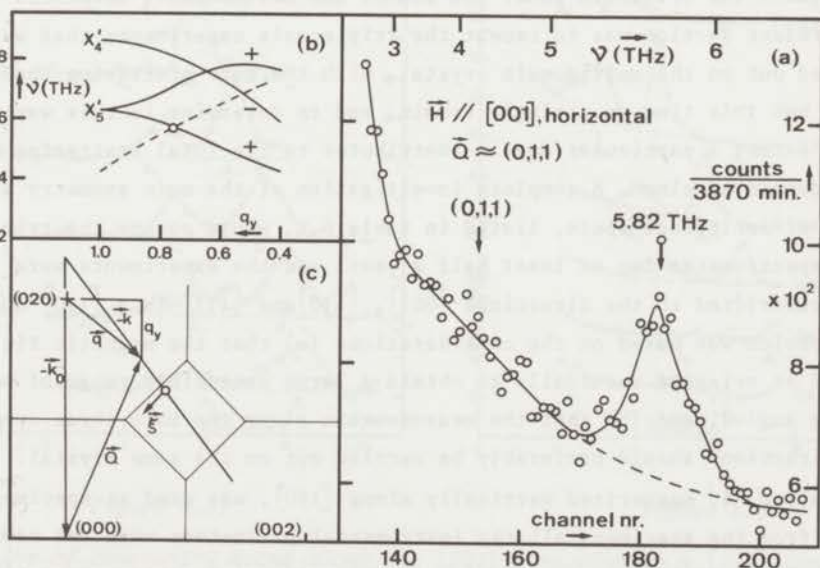


Figure 6.4.

Time-of-flight experiment close to  $(0,1,1)$  in a  $[001]$  domain. The layout in this figure is the same as in figure 6.3.

and that the neutron energy loss in (0,1,1) corresponds to this same frequency, no inelastic scattering by the mixed mode is observed. On the other hand, a maximum due to phonon scattering is appearing at the expected position (calculated frequency:  $\nu = 5.75$  THz).

By a comparison of cross sections for the same excitation in non-equivalent points  $\underline{Q}$ , i.e. points for which the point groups  $G_O^M(\underline{Q})$  are different, it is in general possible to obtain information on the symmetry properties of the excitation. This will be discussed in detail in section 6.6 for the pairs of points  $X^1$  and  $X^2$  that have been investigated by means of the present time-of-flight experiments.

#### 6.4. Triple-axis measurements on a $[110]$ domain

In this section the results of triple-axis experiments on a nickel  $[110]$  domain will be presented. Since the time-of-flight experiments in specific points in  $\underline{Q}$ -space have yielded evidence for the pronounced influence of the magnetization direction on the scattering cross section of the mixed excitation, one may expect the same or a similar influence to exist throughout the Brillouin zone. The aim of the measurements described in the present section was to repeat the triple-axis experiments that were carried out on the multidomain crystal, with the same scattering configuration, but this time on a single domain, and to determine in this way to which extent a particular domain contributes to the total scattering in a multidomain specimen. A complete investigation of the main symmetry directions of reciprocal space, listed in table 6.2, would occupy the triple-axis spectrometer for at least half a year, and the experiments were therefore restricted to the directions  $[001]$ ,  $[\bar{1}10]$  and  $[\bar{1}11]$  in a  $[110]$  domain. This choice was based on the considerations (a) that the magnetic field should be oriented vertically to obtain a large accessible range of scattering angles, and (b) that the measurements along the main three symmetry directions should preferably be carried out on the same crystal. Crystal nr. 4, magnetized vertically along  $[110]$ , was used as specimen. Apart from the specimen, all the instrumental parameters were the same as specified earlier in section 5.3.1. The constant- $Q$  scans were performed in the configuration  $\underline{Q} // \underline{q}$ , which is suitable for the observation of lattice vibrations that are purely or partly longitudinal.

The results of the measurements along the  $[001]$  direction, which were performed in energy loss and energy gain, are summarized in the figures 6.5 and 6.6, respectively. A comparison with the results for the multi-domain sample (figures 5.3 and 5.4) shows that the scattering by the mixed mode has disappeared except possibly in the energy loss scans for  $\zeta \geq 0.5$ . Although it is difficult to decompose the additional peaks at  $\nu = 5$  THz for  $\zeta = 0.7$  and  $0.8$  in figure 6.5, it seems probable that these maxima are in fact double peaks. Observation of the mixed mode in  $(0,0,3)$  may be expected on basis of the time-of-flight result in  $(0,0,1)$  for the

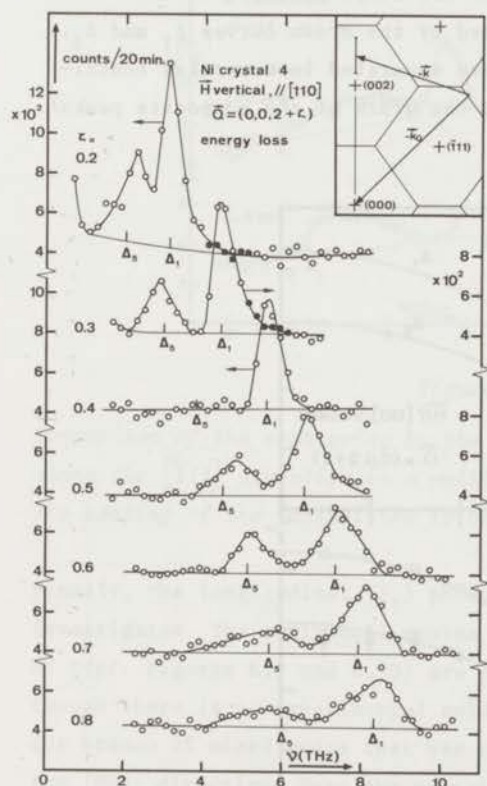


Figure 6.5.

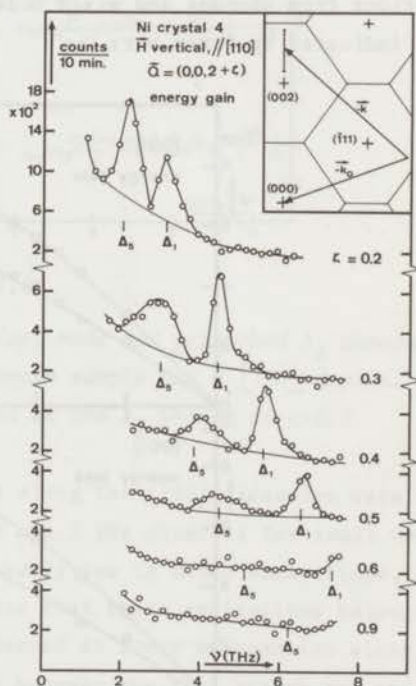


Figure 6.6.

Results of constant-Q scans along the  $[001]$  direction in a  $[110]$  domain, performed in energy loss (figure 6.5) and in energy gain (figure 6.6). The frequencies indicated by  $\Delta_1$  and  $\Delta_5$  refer to the results of Birgeneau et al. [2]. Filled circles are used to distinguish overlapping spectra; arrows indicate the corresponding scale.

[110] domain, shown in figure 6.2. In addition the  $\Delta_5$  phonons contribute to the scattering, which leads to broad maxima near the zone boundary. A striking difference between figures 5.3 and 6.5 is the absence of additional scattering at  $\zeta = 0.4$  for the [110] domain. This result supports the earlier conclusion in section 5.5 that the scattering by  $\Delta_5$  phonons in the outer part of the Brillouin zone has another origin than the scattering by these phonons close to the zone centre, which is due to the finite dimensions of the resolution ellipsoid.

In figure 6.7 the measured frequencies are compared with the data of Birgeneau et al., which are represented by the drawn curves  $\Delta_1$  and  $\Delta_5$ . The broad peaks for  $\zeta \geq 0.7$  have not been separated into partial contributions from phonons and mixed modes; the width of the composite peaks is indicated by error bars.

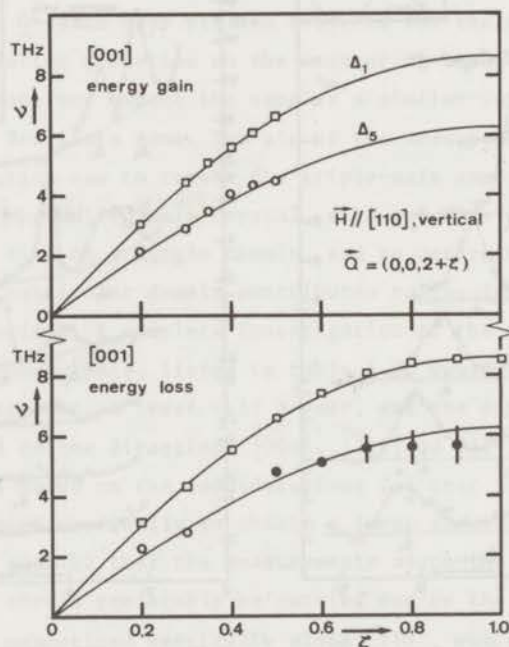


Figure 6.7.

Observed excitations along the [001] direction in a [110] domain.

□: longitudinal phonons,

○: transverse phonons,

●: broad peaks due to mixed modes and perturbed  $\Delta_5$  phonons.

The drawn curves  $\Delta_1$  and  $\Delta_5$  represent the results of Birgeneau et al. In the energy gain scans for  $\zeta \geq 0.6$  the longitudinal phonon was outside the scanned frequency interval (cf. figure 6.6).

Along the  $[\bar{1}11]$  direction only three constant- $Q$  scans were carried out in energy loss at  $\zeta = 0.3, 0.4$  and  $0.5$ . The results are in striking contrast with those obtained for the multidomain specimen, as may be seen from figure 6.8 where similar scans on both samples are compared. Apart from a weak maximum, which may be due to scattering by perturbed  $\Lambda_3$  phonons, no scattering from the mixed mode could be detected in the scans on the single domain.

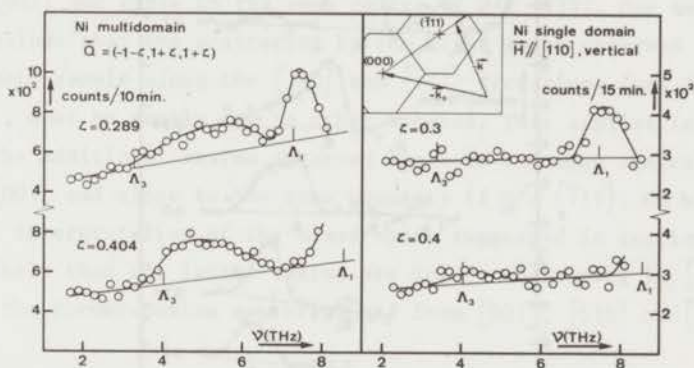


Figure 6.8.

Comparison of the scattering by the mixed mode and perturbed  $\Lambda_3$  phonons along the  $[\bar{1}11]$  direction in a multidomain sample and a  $[110]$  domain. The scaling of the intensities is based on the  $\Lambda_1$  phonon at  $\zeta=0.3$ .

Finally, the longitudinal ( $\Sigma_1$ ) phonons along the  $[\bar{1}10]$  direction were investigated. The additional maxima at  $\nu=6.7$  THz observed for small values of  $\zeta$  (cf. figures 6.9 and 6.10) are probably due to mixed excitations, although there is no experimental evidence that these excitations belong to the branch of mixed modes that was observed at lower frequencies along the  $[001]$  direction. Near the crossing between the flat branch and the  $\Sigma_1$  phonon branch at  $\zeta=0.3$  a resonance-like interference between the phonons and the mixed modes gives rise to an anomalous increase in the scattering by the mixed modes. The continuation of the flat branch on the other side of the crossing could not be observed. It should be emphasized that in figure 6.10 a mixed mode with a frequency  $\nu=4.0$  THz exists at  $\zeta = 1.0$ , which corresponds to the point  $(\bar{1}, 1, 0)$ . This mode has been observed in the

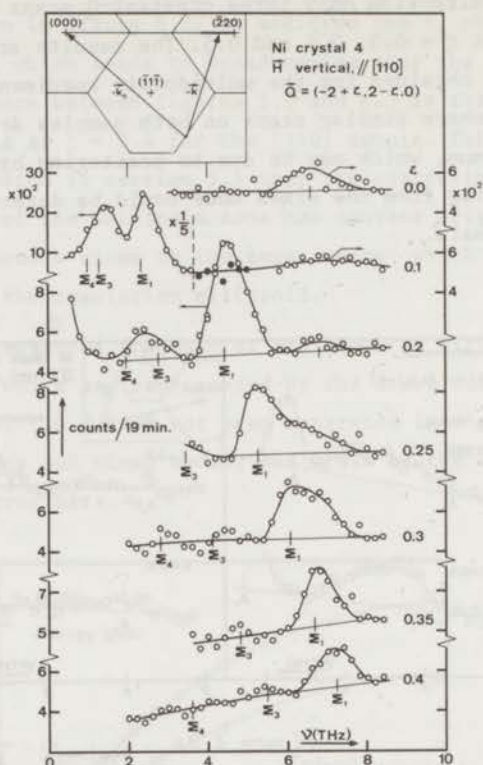


Figure 6.9.

Results of constant- $Q$  scans along the  $[\bar{1}10]$  direction in a  $[110]$  domain. The phonon frequencies indicated by  $\Sigma_1, \Sigma_3$  and  $\Sigma_4$  are taken from [2]. Filled circles have been used to distinguish overlapping spectra; arrows indicate the corresponding scale.

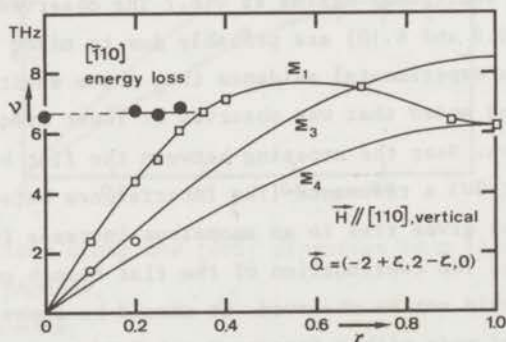


Figure 6.10.

Observed frequencies of longitudinal phonons ( $\square$ ), transverse phonons ( $\circ$ ) and mixed modes ( $\bullet$ ) along the  $[\bar{1}10]$  direction in a  $[110]$  domain. The drawn curves represent the results of Birgeneau et al. [2] on unmagnetized nickel.

time-of-flight experiment close to  $(0,0,1)$  but is not observable in the equivalent point  $(\bar{1},1,0)$  (see table 6.4). For the mixed mode with frequency 6.7 THz the conditions for neutron scattering are reversed. This mode is observable in  $(\bar{2},2,0)$  but not in the equivalent point  $(0,0,2)$ , which corresponds to  $\zeta = 0$  in figure 6.7.

If one reviews the results collected in constant- $Q$  scans on the  $[110]$  domain (see figures 6.5-6.10), it is striking that the mixed modes are only observable in small regions of  $Q$ -space: close to the zone boundary if  $Q// [001]$  and close to the zone centre if  $Q// [\bar{1}10]$ . One may therefore conclude that the scattering by the mixed modes observed for the multidomain sample along the  $[100]$  and  $[\bar{1}11]$  directions (see figures 5.3-5.7), must be partly due to other domains. This applies in particular to the additional maxima observed close to the zone centre  $(0,0,2)$  if  $Q// [001]$  and close to the zone boundary if  $Q// [\bar{1}11]$ . On basis of a possible interpretation of the mixed mode, suggested in section 7.3, it seems likely that the latter maxima are due to scattering in  $[\bar{1}11]$  domains, whereas the former maxima may originate from  $[001]$ ,  $[010]$  or  $[100]$  domains.

### 6.5. An experiment at liquid-nitrogen temperature

In view of the mixed magnetic-vibrational properties of the new excitation it is of interest to collect further information on the origin of the electronic component of the mode. Experiments at low temperatures offer the possibility to distinguish between collective electron excitations and single electron-hole excitations. The occupation numbers  $\langle n(\underline{q}) \rangle_T$  appearing in the cross section of the collective excitations (see (3.30), (3.32) and (3.44)) are governed by Bose-Einstein statistics (3.25), whereas the cross section (3.39) of electron-hole excitations depends on the occupation numbers  $\langle n_{k\sigma} \rangle_T$  of the initial and final electron states, which are determined by Fermi-Dirac statistics (3.37). Consequently, the cross section of collective excitations decreases when the temperature is reduced: for  $T \rightarrow 0$  the energy gain cross section tends to zero, while the energy loss cross section approaches a constant value. On the other hand, the cross section of a single electron excitation is determined by the energies of the initial and final electron states relative to the Fermi energy  $E_F$ . It will be shown below that the energy loss cross section increases for decreasing  $T$

if the electron states are close to the Fermi level and  $E_F$  does not change; under the same conditions the energy gain cross section decreases.

For a collective excitation with a frequency  $\nu = 4.0$  THz one obtains the following occupation numbers at  $T = 296$  K and  $T = 82$  K :

$\langle n(\nu) \rangle_{296} = 1.10$  and  $\langle n(\nu) \rangle_{82} = 0.11$ . Hence the energy gain cross section changes by a factor 10, while the energy loss cross section, which depends on  $\langle n(\nu)+1 \rangle_T$ , changes by a factor  $\approx 2$ . If one considers electron transitions between states situated 4.0 THz below  $E_F$  and at  $E_F$ , respectively, the following occupation numbers are of interest:

$\langle n_{\underline{k}\sigma} \rangle_{296} = 0.657$ ,  $\langle n_{\underline{k}\sigma} \rangle_{82} = 0.912$ ,  $\langle 1 - n_{\underline{k}+\underline{Q}\sigma} \rangle_T = 0.5$ . For the states chosen above the ratio between the cross sections becomes

$$\left( \frac{d^2\sigma}{d\Omega dE} \right)_{\text{loss},82} = 1.39 \times \left( \frac{d^2\sigma}{d\Omega dE} \right)_{\text{loss},296}$$

$$\left( \frac{d^2\sigma}{d\Omega dE} \right)_{\text{gain},82} = 0.26 \times \left( \frac{d^2\sigma}{d\Omega dE} \right)_{\text{gain},296}$$

It should be emphasized, however, that the cross section ratio is a function of the positions of the electron states relative to  $E_F$ .

The experiment was performed on crystal nr. 4, which was mounted in a cryostat with its  $[110]$  axis vertical, and magnetized along the  $[\bar{1}10]$  axis in a horizontal magnetic field of 9075 Oe. The time-of-flight spectrometer was set to observe the mixed mode as close to the point  $\underline{Q} = (0,0,1)$  as possible. As a result of the limitations to the accessible angular range for the incident and scattered beam the experiment could not be performed at the zone boundary; the experimental configuration is shown in figure 6.11. In the present measurement one has to apply a rather strong field, because the magnetic anisotropy constants increase as the temperature is reduced. At  $T = 80$  K a field of 3 kOe would not be sufficient to magnetize the crystal along the  $[\bar{1}10]$  direction, and a deviation of the magnetization direction towards a  $[111]$  direction would occur. Since this deviation would lead to a decrease in the scattering cross section (cf. figure 6.1), it would be impossible to draw any conclusion regarding the occupation number of the mode.

Measurements were carried out at room temperature,  $T = 296$  K, and at  $T = 82$  K; the observation times were adjusted in such a way that the accumulated intensities in the elastic incoherent peak were approximately equal. It may



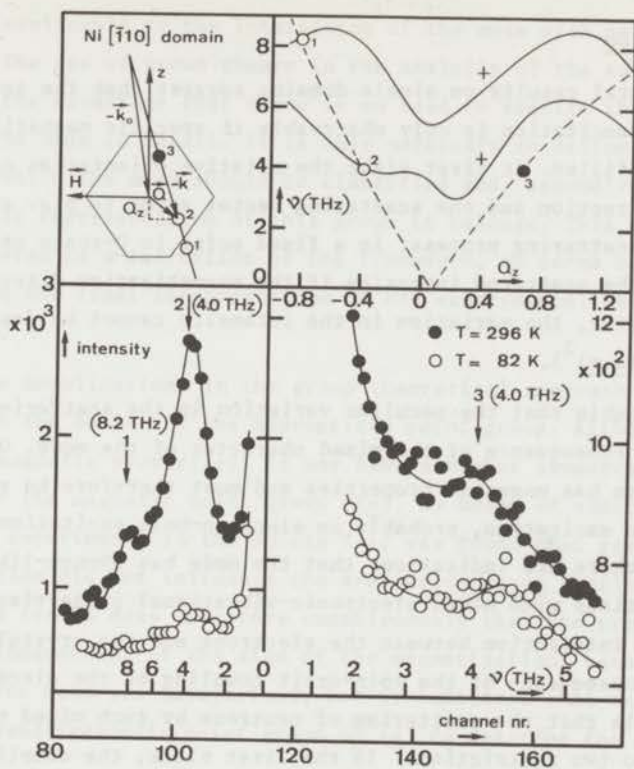


Figure 6.11.

Comparison of time-of-flight spectra at  $T = 296$  K and 82 K

be seen from figure 6.11 that the scattering by the mixed mode is very weak, which is due to the fact that the point of observation is rather unfavourable. Although the experimental accuracy is poor, it still seems possible to conclude that the scattering by the mixed mode does not change appreciably when the temperature is reduced, while the frequency increases by about 9% from 4.0 to 4.35 THz. A subsequent measurement was carried out at room temperature after removal of the crystal to check that the additional peak was due to scattering by the nickel specimen. It may be seen that the change in the annihilation cross section for the nearly longitudinal phonon with  $\nu = 4.0$  THz in figure 6.11 is indeed roughly a factor 10, as expected for a collective mode. On the other hand, the behaviour of the cross section for the mixed mode indicates that the thermal properties of this mode are consistent with those of a single electron excitation.

## 6.6. Discussion

The experimental results on single domains suggest that the scattering by the mixed excitation is only observable if specific magnetic conditions are fulfilled. At first sight the relative orientation of the magnetization direction and the scattering vector seems to play a dominant role in the scattering process: in a fixed point in  $Q$ -space one observes a change in the scattered intensity if the magnetization direction is changed. However, the variation in the intensity cannot be described by a factor  $\{1 + (\underline{e} \cdot \underline{m})^2\}$ .

It seems probable that the peculiar variation in the scattering cross section is a consequence of the mixed character of the mode. Obviously, the excitation has magnetic properties and must therefore be some kind of electronic excitation, probably an electron-hole excitation. On the other hand, there are indications that the mode has phonon-like properties. Excitations with mixed electronic-vibrational properties may exist, owing to the interaction between the electrons and the crystal lattice, which is a consequence of the spin-orbit coupling of the electrons. It seems probable that the scattering of neutrons by such mixed modes will be subject to two restrictions. In the first place, the coupling between the electrons and the lattice is restricted by selection rules that are connected with the symmetry of the electron states, the lattice vibrations and the electron-phonon interaction potential (cf. section 2.2). In this way the magnetization direction may favour or prevent the formation of a mixed excitation with specific symmetry properties. This aspect will be discussed in section 7.3. Once the magnetic selection rules permit the coupling between the electron states and a lattice vibration with a specific symmetry (i.e. a specific polarization vector  $\underline{\xi}$ ), the scattering of a neutron by the mixed mode is restricted by similar selection rules, based on the transformation properties of the mixed mode and the symmetry of the interaction potential between the neutron and the mode.

The aim of the present discussion is to arrive at a more detailed specification of the symmetry properties of the mixed mode, which could only be described in very general terms in section 5.5. It will be shown that the irreducible representation belonging to the mixed mode may be determined in some of the investigated single domains by means of the selection rules

that are applicable to the interaction of the mode with neutrons and phonons. The use of group theory in the analysis of the experimental data has the advantage that there is no need to specify the eigenfunction of the mode in detail. It is only necessary to define the point group in which the mode should be classified and, secondly, to which irreducible representation of this group it belongs. This analysis may be considered as a definition of the framework, in terms of symmetry, into which the final interpretation of the experimental results should be fitted.

One of the complications in the group-theoretical approach is the ambiguity in the choice of the appropriate point group. Although the mixed mode has magnetic properties, it may have a higher symmetry than that allowed by the magnetic point group  $M(\underline{q})$ . By means of additional time-of-flight experiments in the points X it was found that reversal of the magnetization did not influence the scattering cross section of the mixed mode. This result does not prove unambiguously that the properties of the mode are independent of the sign of the magnetization, because the incident neutron beam was unpolarized, but it indicates that one may possibly use the pseudo-magnetic point group  $G_0^{+M}(\underline{q})$  to describe the mixed mode.

Another uncertainty arises in connection with the application of the selection rules for neutron scattering. In the present experiments it was not possible to establish whether the scattering by the mixed mode is a process with or without spin flip. To distinguish between the two processes, an experimental set-up would be needed in which the incident beam is polarized and the polarization of the scattered neutrons is analyzed. In view of these uncertainties the following possibilities will be considered:

- (a) scattering with or without spin flip on basis of the unitary subgroup  $G_0^M(\underline{q})$  of the magnetic point group  $M(\underline{q})$ .
- (b) scattering without spin flip on basis of the pseudo-magnetic point group  $G_0^{+M}(\underline{q})$ .

It should be emphasized that excitations transforming according to irreducible representations of a pseudo-magnetic group cannot possess a magnetic moment. Consequently the neutron spin cannot flip during the scattering process.

To apply the selection rule (2.13) to inelastic neutron scattering in a point  $\underline{Q}$  in reciprocal space, one has to determine the corresponding subgroup  $G_{\underline{O}}^M(\underline{Q})$  or  $G_{\underline{O}}^{+M}(\underline{Q})$ , which consists of the elements of  $G_{\underline{O}}^M(\underline{q})$  or  $G_{\underline{O}}^{+M}(\underline{q})$  that leave  $\underline{Q}$  invariant. Suppose that the mixed mode transforms according to an irreducible representation of  $G_{\underline{O}}^M(\underline{q})$ . Since the selection rule is defined for the subgroup  $G_{\underline{O}}^M(\underline{Q})$ , the representation of the mode should be decomposed into irreducible representations of this subgroup by means of (2.5) and (2.6). After these preliminaries the selection rule may be applied, taking into account that the neutron states transform as double-valued representations and the mixed mode as a single-valued representation (cf. section 3.4.3). One may attempt to determine the irreducible representation of the mode in the point group  $G_{\underline{O}}^M(\underline{q})$  by a comparison of neutron scattering cross sections in two points  $\underline{Q}_1, \underline{Q}_1 = \underline{q} + \underline{r}_1$  and  $\underline{Q}_2 = \underline{q} + \underline{r}_2$ , with different point groups  $G_{\underline{O}}^M(\underline{Q})$ . The subdivision of the representation of the mode onto these point groups yields different irreducible representations, which implies that the cross sections in  $\underline{Q}_1$  and  $\underline{Q}_2$  are different. In appendix B a detailed group-theoretical analysis is given of the time-of-flight results in the various points X (cf. tables 6.3-6.5). For each case the absence of scattering in a specific point is interpreted as a consequence of interdiction by the selection rule.

An important conclusion from the analysis is that the scattering cross section of the mixed mode with  $\underline{q} = (0,0,1)$  or  $(1,0,0)$  cannot be explained by means of magnetic point groups, except for the mode with  $\underline{q} = (0,0,1)$  in the  $[001]$  domain. In the other three cases the experimental results can be described by means of pseudo-magnetic point groups, which indicates that the mixed mode has no magnetic moment for these combinations of  $\underline{M}$  and  $\underline{q}$ . The interpretation of the scattering results by means of selection rules is less reliable when the cross section is found to be zero in all investigated points  $\underline{Q}$ , which is the case for the points  $(1,0,0)$ ,  $(0,1,1)$  and  $(0,1,\bar{1})$  in the  $[111]$  domain. In table 6.7 a summary is given of the possible representations of the mixed mode.

Table 6.7.

Possible irreducible representations for the mixed modes with  $\underline{q} = (1,0,0)$  and  $(0,0,1)$ .

$\underline{M}$	$\underline{q}$	point group	possible rep. mixed mode	angular momentum (units $\hbar$ )	final selection <sup>*</sup> )
[001]	(0,0,1)	$G_o^M(\underline{q}) = C_{4h}$	$\Gamma^5$ $\Gamma^7$ $\Gamma^8$	$\begin{cases} 0 \\ +1 \\ -1 \end{cases}$	
[001]	(0,0,1)	$G_o^{+M}(\underline{q}) = D_{4h}$	$\Gamma^4, \Gamma^9$	0	$\Gamma^9$
[001]	(1,0,0)	$G_o^{+M}(\underline{q}) = D_{2h}$	$\Gamma^5, \Gamma^8$	0	$\Gamma^5, \Gamma^8$
[110]	(0,0,1)	$G_o^{+M}(\underline{q}) = D_{2h}$	$\Gamma^4, \Gamma^8$	0	$\Gamma^8$
[111]	(1,0,0)	$G_o^{+M}(\underline{q}) = C_{2h}$	$\Gamma^4(?)$	0	?

<sup>\*</sup>) This selection is based on the assumption that the mode transforms according to an odd representation (see page 100).

A similar procedure may be used to determine possible representations for the mixed mode with  $\nu = 6.7$  THz and  $\underline{q} = (0,0,0)$  in the  $[110]$  domain, which was observed by means of triple-axis experiments in  $\underline{Q}_2 = (\bar{2},2,0)$ , but could not be observed in  $\underline{Q}_1 = (0,0,2)$  (cf. figures 6.10 and 6.7, respectively). The point groups for  $\underline{Q}_1$  and  $\underline{Q}_2$  are identical to those for  $\underline{Q}_1 = (0,0,1)$  and  $\underline{Q}_2 = (1,\bar{1},0)$  in the  $[110]$  domain, and the analysis leads to the conclusion that the neutron scattering by this mode can only be explained by means of pseudo-magnetic point groups. By means of the subduction table B.4 and the table of observable excitations B.2, two possible representations are found:  $\Gamma^3$  and  $\Gamma^7$  of  $D_{2h}$ . From this result one may conclude that the modes with  $\underline{q} = (0,0,0)$ ,  $\nu = 6.7$  THz and  $\underline{q} = (0,0,1)$ ,  $\nu \approx 4$  THz in the  $[110]$  domain are essentially different. In other words, if the modes are considered as specific points  $(\nu, \underline{q})$  of a dispersion relation, they do not belong to the same branch. This may be proved by means of the compatibility relations for the excitations with  $\underline{q} = (0,0,\tau)$ , for which  $G_o^{+M}(\underline{q}) = C_{2v}$ , at the zone centre  $(0,0,0)$  and the zone boundary  $(0,0,1)$  where  $G_o^{+M}(\underline{q}) = D_{2h}$ . From table B.4 it is seen that the mixed mode in  $(0,0,1)$ , which transforms as  $\Gamma^4$  or  $\Gamma^8$  of  $D_{2h}$ , is compatible with

a  $\Gamma^2$  or  $\Gamma^1$  branch along  $[00\bar{z}]$ , whereas the mixed mode in  $(0,0,0)$ , which transforms as  $\Gamma^3$  or  $\Gamma^7$  of  $D_{2h}$ , is compatible with a  $\Gamma^3$  or  $\Gamma^4$  branch.

As a logical continuation of the analysis in appendix B one might finally attempt to explain the experimental data by means of point groups with still higher symmetry. It turns out that this approach fails, because the next group is  $G_o(\underline{q}) = D_{4h}$  for each of the cases in table 6.7. Consequently, the mixed mode would transform according to the same irreducible representation of  $D_{4h}$  in each domain, and the selection rule would allow neutron scattering in  $\underline{Q} = (1,0,0)$  and  $(0,0,1)$  irrespective of the magnetization direction, which is in contradiction with the experimental results.

The fact that the frequencies of the mixed modes with  $\underline{q} = (0,0,1)$  or  $(1,0,0)$  are approximately the same in different domains, suggests that one is observing the same excitation in each domain. The difference in the scattering cross sections may possibly be explained as a consequence of the modification of the transformation properties of the excitation by magnetic interactions. According to this argument one should preferably use a description for the excitation that is applicable to each of the domains, i.e. the one based on pseudo-magnetic point groups  $G_o^{+M}(\underline{q})$ . We shall therefore assume that the mixed mode has no magnetic moment, and that its magnetic properties are a result of magnetic interactions transferred via the spin-orbit coupling of the electrons.

A second selection from the possible representations in table 6.7 can be made if one takes into account that the mode has a vibrational component. Since the lattice vibrations with  $\underline{q} = (0,0,1)$  transform according to odd representations ( $\Gamma_{ii}^\alpha(I) = -1$ )\*, one may expect that the mixed mode also transforms as an odd representation. Hence the representations  $\Gamma^4$  of  $D_{4h}$ ,  $\Gamma^4$  of  $D_{2h}$  and  $\Gamma^4$  of  $C_{2h}$  should be excluded. This implies that the classification of the mixed mode in the  $[111]$  domain by means of selection rules has yielded an incorrect result. The failure of the procedure for this case is probably due to the fact that no positive scattering result is available for one of the points  $\underline{Q}$ , and is therefore not considered as a disqualification of the analysis for the other domains.

If the mixed mode with  $\underline{q} = (1,0,0)$  in the  $[111]$  domain is assumed to transform as the odd representation  $\Gamma^3$  of  $C_{2h}$ , neutron scattering in  $\underline{Q}_1 = (1,0,0)$  and  $\underline{Q}_2 = (0,1,1)$  is allowed by symmetry. Similarly, one might expect

\*) Subduction of  $X_4'$  and  $X_5'$  onto the groups listed in table 6.7 yields odd representations.

scattering in  $Q_3 = (0, 1, \bar{1})$  if the mode transforms as  $\Gamma^2$  of  $C_{2h}$  (cf. table B.4). In section 7.3 a possible explanation for the absence of scattering in these points will be suggested.

The second item of this discussion is the observation of "forbidden" neutron-phonon scattering, which may be related to the symmetry properties of the phonons. In a crystal with cubic symmetry the phonons with  $q$  along the symmetry directions  $\Delta$ ,  $\Lambda$  and  $\Sigma$  are purely transverse or longitudinal, and neutron scattering by the transverse phonons is forbidden if  $Q//q$ . The observation of phonon scattering near the zone boundary, at frequencies close to the transverse branches  $\Delta_5$  and  $\Lambda_3$  indicates that the symmetry of the phonons is reduced. As stated earlier in section 5.5, it seems probable that this reduction in symmetry is due to the interaction between the phonons and mixed modes, because the perturbation is most pronounced in those regions of the Brillouin zone where the frequencies of the phonons and the mixed modes are approximately equal. If this assumption is correct, the wave functions of the perturbed phonons should transform according to irreducible representations of  $G_o^M(q)$  or  $G_o^{+M}(q)$ , where the point group is related to the symmetry of the interaction between the mixed modes and the phonons. Since the main part of the experimental results on perturbed phonons has been collected in the  $[001]$  direction, the following analysis of the symmetry properties of phonons in single domains will be restricted to this direction. The point groups of interest may be found in table B.1, because the point groups of  $q = (0, 0, \zeta)$  and  $Q = (0, 0, 1)$  are identical (see the definition of the point group of the scattering vector  $Q$ , given in section 3.4.3).

To determine the conditions for neutron-phonon scattering in single domains one may use the procedure that was applied above to the scattering by the mixed mode. The representations of the phonons with  $q = (\zeta, 0, 0)$  and  $(0, 0, \zeta)$  are listed in table B.5 for different magnetization directions. It is seen that a reduction in symmetry results in a removal of the degeneracy of the  $\Delta_5$  phonons. If the phonons are described by means of the point group  $G_o^{+M}(q)$ , neutron scattering by the former  $\Delta_5$  phonons is still forbidden if  $q//Q$ , except in the  $[111]$  domain. This may easily be verified by a comparison of the representations in table B.5 with table B.2, where the observable excitations with spin 0 are listed. To explain the observation of forbidden neutron-phonon scattering in the  $[110]$  domain the phonons should therefore be treated on basis of the magnetic point group  $G_o^M(q)$ . In that case the

representation  $\Gamma^4$  of  $C_{2v}$  for one of the transverse phonon branches is reduced to  $\Gamma^1$  of  $C_s$  which allows a deviation of the polarization vector in the plane perpendicular to  $\underline{M}$  and neutron-phonon scattering.

This analysis for the phonons propagating along  $[001]$  in a  $[110]$  domain shows that the observed perturbation of the phonons cannot be explained by lattice deformations that are caused by magnetostriction, because these effects are invariant under magnetization reversal and result in a symmetry to be described with  $G_o^{+M}(\underline{q})$ . Hence, interaction with the mixed mode at  $\nu \approx 4$  THz appears to be the most probable origin of the perturbation of the phonons. Although the symmetry properties of the mixed mode are governed by the pseudo-magnetic point group, the interaction between the mode and the originally transverse phonons has a lower symmetry and must be treated by means of the magnetic point group.

The observed interference between the mixed modes and the phonons in the  $[110]$  domain offers a possibility to confirm the final selection from the possible representations for the mixed mode given in table 6.7. If the interaction potential is invariant under the operations of  $G_o^M(\underline{q})$ , interference between the phonons and mixed modes is only possible if both transform according to the same irreducible representation of  $G_o^M(\underline{q})$ . As the mixed mode has no magnetic moment in this case, the forbidden neutron-phonon scattering must be due to  $\Gamma^1$  phonons. Hence one may conclude that the mixed mode that gives rise to the observed interference with the phonons at  $\underline{q} \approx (0,0,0.5)$  in the  $[110]$  domain, transforms as  $\Gamma^1$  of  $G_o^M(\underline{q}) = C_s$  (i.e. it should be invariant under reflection in the (110) plane). The compatibility relations in  $\underline{q} = (0,0,1)$  require that the mixed mode has the same property,  $\chi(IC_{2a}) = 1$ , at the zone boundary, which implies that the mode with  $\underline{q} = (0,0,1)$  in the  $[110]$  domain transforms as  $\Gamma^8$  of  $D_{2h}$  (cf. table A.8).

In a similar way, the representation of the mixed mode with  $\underline{q} = (0,0,0)$  in the  $[110]$  domain may be determined unambiguously by means of the observed interference with the "longitudinal" phonons at  $\underline{q} \approx (0.3,-0.3,0)$ . The former  $\Sigma_1$  phonons transform as  $\Gamma^1$  both in the magnetic and the pseudo-magnetic point group, whereas the mixed mode with  $\underline{q} = (0,0,0)$  transforms as  $\Gamma^3$  or  $\Gamma^7$  of  $G_o^{+M}(\underline{q}) = D_{2h}$ . To establish the compatibility relations for the mixed mode branch in the  $[\bar{1}\bar{1}0]$  direction, for which  $G_o^{+M}(\underline{q}) = C_{2v}$ , the subduction table for the  $[110]$  domain in table B.4 may be used. It is



found that the representations  $\Gamma^3$  and  $\Gamma^7$  in  $(0,0,0)$  are compatible with the representations  $\Gamma^2$  and  $\Gamma^1$  along  $[\zeta\bar{\zeta}0]$ , of which only the latter can interfere with the  $\Gamma^1$  phonons. Further reduction to the magnetic point group  $G_O^M(\zeta, \bar{\zeta}, 0) = C_s$  does not change the interference condition, because  $\Gamma^2$  and  $\Gamma^1$  of  $C_{2v}$  are reduced to  $\Gamma^2$  and  $\Gamma^1$  of  $C_s$ , and hence one may conclude that the mixed mode with  $\underline{q} = (0,0,0)$  in the  $[110]$  domain transforms as  $\Gamma^7$  of  $D_{2h}$ . No conclusion can be drawn with respect to the symmetry of the interaction between this mode and the phonons.

As shown above, a detailed investigation of the phonon dispersion relation in single domains may be useful as an independent check on the determination of the irreducible representation for the mixed mode with  $\underline{q} = (0,0,1)$  or  $(1,0,0)$ . By means of measurements along the  $[\zeta 00]$  direction in a  $[001]$  domain one may distinguish between the two possible representations  $\Gamma^5$  and  $\Gamma^8$  given in table 6.7. If interference between the mixed mode and the originally transverse phonons is observed, the former should transform as  $\Gamma^1$  of  $G_O^M(\zeta, 0, 0) = C_s$ , a representation which is compatible with  $\Gamma^8$  of  $G_O^{+M}(1, 0, 0) = D_{2h}$ , but not with  $\Gamma^5$ .

The present discussion has been restricted to a classification of the mixed modes according to their transformation properties, in order to extract as much information from the experimental results as possible, without specifying the eigenfunctions of the modes in detail. In the next stage of the analysis, to be presented in chapter VII, an attempt will be made to construct physically realistic excitations, in which electronic and vibrational properties are combined in such a way that the mixed excitations have the transformation properties derived above.

## CHAPTER VII

### DISCUSSION AND CONCLUSION

#### 7.1. Introduction

The discussion presented in this concluding chapter may be considered as the third stage in the interpretation of the results, complementary to the preliminary discussion in section 5.5 and the group-theoretical analysis in section 6.6. In contrast to the analysis in section 6.6, where the symmetry properties of the mixed modes were determined in a straightforward way from the experimental results, the following interpretation is much more speculative. This applies in particular to section 7.3, where a possible interpretation of the mixed electronic-vibrational modes is suggested, and to section 7.4, where a tentative explanation is given for the discrepancy between energy gain and energy loss scattering by the mixed modes.

Although the final interpretation of the mixed modes is speculative, the existence of these additional modes in nickel could be established with more certainty. In general, spurious maxima occur quite frequently in neutron scattering experiments, and some possible sources of spurious scattering are mentioned in section 7.2. In the present investigation, however, it could be shown (by applying a magnetic field along symmetry directions) that the observed additional scattering was not due to spurious scattering processes.

The interaction between the mixed modes and the magnons, which has not been considered in section 6.6, is discussed in section 7.5. In addition, this final section contains a summary of the characteristic properties of the mixed modes, and a short speculation concerning the possible existence of similar modes in other metals.

#### 7.2. Observation of mixed modes and forbidden phonon scattering

Below we shall consider the experimental limitations for the observation of the mixed modes and perturbed phonons. In the outer region of the Brillouin zone the modes are in general not easily observed because their frequency is of the same order as the frequency of the transverse phonons. Moreover, the scattering cross section is small compared to that of the phonons, and observation of the mixed modes is therefore only possible in scattering configurations where scattering by the transverse phonons is weak or forbidden by symmetry.

From the experimental data it is obvious that even in the configurations that are most favourable for intensity reasons, i.e. energy loss, constant- $Q$  scans with  $Q$  along high-symmetry directions, the scattering by the mixed mode is not observed separately, but in combination with scattering from nearly transverse phonons which have been perturbed by interference with the mixed mode. Hence a second condition for the observation of the additional mode is that the instrumental resolution allows a separation of the two contributions, a condition which is in general not fulfilled in conventional phonon scans with a triple-axis spectrometer.

A complicating factor in the investigation of magnetic perturbations of phonons is the possible occurrence of spurious phonon peaks, even when the instrumental configuration has been chosen especially to eliminate the scattering by these phonons. One possible source of spurious neutron-phonon scattering are double scattering processes, in which the incident neutrons are scattered elastically in the sample (a Bragg reflection corresponding to a reciprocal lattice vector  $\tau_1$ ) prior to the inelastic scattering process [91]. The first reflection results in a secondary incident beam with a wave vector  $\underline{k}'_0 = \underline{k}_0 - \tau_1$  and hence there are two possible scattering vectors  $\underline{Q} = \underline{k}_0 - \underline{k}$  and  $\underline{Q}' = \underline{k}'_0 - \underline{k}$ , for which the selection rules for phonon scattering are different. A similar situation occurs when the sequence in the double process is reversed; in that case the inelastic process precedes the Bragg scattering, and there is a primary and a secondary scattered beam. Unexpected scattering by transverse phonons in  $\text{Ni}_{.55}\text{Pd}_{.45}$ , observed recently by Kamitakahara and Brockhouse [92], has been attributed to this type of multiple scattering.

A second source of spurious scattering, which is related to the instrumental resolution, is of importance for alkali metals, where the dispersion surfaces are highly anisotropic. The consequences of a rapid variation of the phonon frequencies and polarization vectors within the volume of the resolution ellipsoid have been considered by Copley for rubidium [93] and by Werner and Pynn for sodium [94]. Spurious phonon scattering may be particularly pronounced if the longitudinal and transverse phonons are nearly degenerate, which is the case in body-centred cubic crystals for  $\underline{q} \approx (0,0,1)$ . In nickel this effect is expected to be less important.

At the outset of the present experiments on the multidomain sample the conditions have been chosen in such a way that observation of the mixed mode

was relatively easy. The search for additional scattering processes close to the zone boundary by means of the time-of-flight spectrometer was aimed in particular at the frequency region around 5 THz, and special care was taken to suppress the scattering by transverse phonons. Furthermore, the instrumental resolution for energy loss processes was sufficient to separate the additional maximum from the weak maximum corresponding to the transverse phonon, which indicated that two distinct excitations contributed to the scattering.

In a later stage of the experiments a series of constant- $\underline{Q}$  scans was performed on the multidomain sample to check if the broad maximum observed in  $\underline{Q} = (3,0,0)$ , in particular the phonon contribution at  $\nu \approx 5.90$  THz, could be due to double scattering processes. No significant difference could be observed between three scans for which the final wave vector was chosen equal to 3.93, 4.28 and 4.66  $\text{\AA}^{-1}$ , respectively. This result indicates that double processes are not contributing to the scattering, because the Bragg scattering in such a process is expected to be very sensitive to a change in the neutron wave vectors  $\underline{k}_0$  and  $\underline{k}$ .

Positive indications for the magnetic origin of the additional mode and the unexpected scattering by transverse phonons were finally obtained from experiments on single domains. The variation in the scattering cross section of the mixed mode as a function of the magnetization direction (cf. figures 6.1 and 6.2) shows clearly that the mode has magnetic properties. Furthermore, it could be shown (by applying a magnetic field along the  $[110]$  direction) that the forbidden scattering by the  $\Lambda_3$  phonons, observed in the multidomain sample close to  $\underline{Q} = (-3/2, 3/2, 3/2)$ , is almost entirely due to a change in the phonon symmetry by a magnetic perturbation (cf. figure 6.8). It seems likely that the forbidden scattering by the  $\Delta_5$  phonons close to  $\underline{Q} = (0,0,3)$  may be influenced in a similar way by the magnetization direction. Experiments at  $\underline{Q} = (0,0,3)$  in other single domains, in addition to those in the  $[110]$  domain, have not been performed because of time limitation. There are other experimental results, however, which indicate that the scattering cross section of the  $X_5'$  phonons depends on the magnetization direction. In comparing the time-of-flight experiments presented in figures 5.1 and 6.4, which were performed on a multidomain sample and a  $[001]$  domain, respectively, one observes a pronounced increase in the scattering cross section of the + phonon with  $\nu \approx 5.9$  THz in the  $[001]$  domain. Since this + branch is compatible with the  $X_5'$  phonon in  $(0,1,1)$  one may expect similar changes in the cross

section of the  $X'_5$  phonons in (1,0,0) and (3,0,0).

The interference between the mixed modes and the phonons is strongest if their frequencies are approximately equal, and therefore the perturbation of the phonons is most pronounced in a few parts of the dispersion relation: the  $\Delta_5$ ,  $\Sigma_1$  and  $\Sigma_4$  branches close to the zone boundary point X, and the branch  $\Lambda_3$  close to the zone boundary point L (see figures 2.1 and 2.2). In connection with the present results, it seems likely that the anomalous frequency shifts observed by DeWit and Brockhouse in the  $\Lambda_3$  and  $\Sigma_1$  branches (denoted as  $T(\xi\xi\xi)$  and  $\Lambda(0\xi 1)$  in their paper [18]) are caused by the interaction between these phonons and the mixed modes.

Observation of additional scattering from a  $^{60}\text{Ni}$  crystal has been reported by Lowde and coworkers [9,77], who performed time-of-flight, energy gain scans in the (100) plane. An excess of scattering was observed close to the zone boundaries for small  $\omega$ , which was ascribed to longitudinal spin-spin correlations  $\langle S^z S^z \rangle_T$  (see eq. (3.34)). Although our data show that the energy gain scattering by the mixed modes is weak along the [001] direction, the observed excess might be due to these modes. Unfortunately, it is quite difficult to compare the results for  $^{60}\text{Ni}$  with our time-of-flight scans close to the zone boundary points X, because the former data are presented after averaging over different directions  $\underline{e} = \underline{Q}/Q$  in the (100) plane and integration over small intervals of 5 meV in  $\hbar\omega$  (which corresponds to a resolution of 1.21 THz).

### 7.3. A possible interpretation of the mixed modes

In the course of the present investigation the following properties of the additional modes could be established:

- (a) The modes have both magnetic and vibrational properties. It was found that the neutron scattering cross section depends on the magnetization direction, that the modes interact with the magnons, and finally that the interaction between the modes and the phonons has the symmetry of the magnetic or the pseudo-magnetic point group. From a comparison between the cross sections at  $T = 296$  K and 82 K it was concluded that the variation of the occupation number of the mode as a function of temperature is consistent with that of an electron-hole excitation. On the other hand, the magnitude of the cross section in energy loss experiments, which is of the same order as the neutron-phonon cross section, is too large to

be explained by magnetic scattering. Hence it seems probable that the main contribution to the scattering is due to the vibrational component of the modes.

- (b) The energy of the modes is almost independent of  $\underline{q}$  and very small in comparison with the electron energies.
- (c) In the  $[110]$  domain two different mixed modes were observed, which transform according to the irreducible representations  $\Gamma^7$  and  $\Gamma^8$  of  $D_{2h}$ , and have clearly different energies. Each of the modes is observable in a limited region of  $\underline{Q}$ -space.
- (d) The modes with  $\underline{q} = (0,0,1)$  and  $\underline{q} = (1,0,0)$ , observed in the  $[001]$  domain, transform according to irreducible representations that are not compatible ( $\Gamma^9$  of  $D_{4h}$  is compatible with  $\Gamma^7$  of  $D_{2h}$ ). Hence these modes have different transformation properties, although their energies are equal within the experimental accuracy.

The appearance of an additional branch in the excitation spectrum of a crystal can be explained in two ways: either it may be due to a mixing of other known elementary excitations, or it may be a truly new branch which is related to a degree of freedom not considered before. With regard to the first possibility, it is difficult to conceive how a combination of phonons and magnons might lead to a new branch without dispersion. The same difficulty is encountered if one tries to construct mixed excitations from single electron excitations and phonons, because the electron-hole excitations in the electron system occupy a continuum in  $(\underline{Q}, \omega)$ -space. Hence it seems that the mixed excitations should be explained by invoking a new degree of freedom.

Most of the experimental results can be understood qualitatively if it is assumed that the mixed modes are polar electron-hole excitations similar to the polar magnons considered by Slater [95] and Sokoloff [96]. As a result of the finite range of the interaction between the electrons, an electron-hole pair may form a bound state. Instead of moving in an uncorrelated way through the lattice, the electron and hole spend most of their time on nearest neighbour sites or, occasionally, on sites with a larger relative distance. These polar modes may in fact be considered as an impurity in the periodic charge distribution of the electrons, and the calculation of their eigenfunctions and energies may be performed in a similar way as for a mass defect or a magnetic impurity in the lattice.

By identifying the observed modes with polar electron-hole excitations, one may understand the results (c) and (d) listed above. If the hole is supposed to be localized at one particular lattice site, while the electron spends its time on the nearest neighbour sites, there are 12 polar modes, which transform as the irreducible representations of the point group  $G_0$  of the considered set of 13 lattice sites. Inclusion of more distant lattice sites leads to an increase in the number of possible modes. Each of the polar modes has a constant energy, except in those regions of  $(Q, \omega)$ -space where interference with other excitations is strong.

For a theoretical treatment of the polar modes in a metal, it is convenient to start from a description of the 3d electrons by means of Wannier functions  $w_{j\sigma}(\underline{r}-\underline{L})$  localized on the lattice sites  $\underline{L}$ . The relation between the Wannier functions and the Bloch functions (2.29) is given by

$$w_{j\sigma}(\underline{r}-\underline{L}) = N^{-\frac{1}{2}} \sum_{\underline{k}} \exp(-i\underline{k}\cdot\underline{L}) \psi_{j\underline{k}\sigma}(\underline{r}), \quad (7.1)$$

where the summation is over all the Bloch functions of the band characterized by the indices  $j$  and  $\sigma$ , with  $\underline{k}$  covering the first Brillouin zone. The main argument for applying Wannier functions to describe the polar modes is that the condition on which the description in terms of Bloch functions is based, viz. the translational periodicity of the lattice, is no longer fulfilled in this case.

To explain the small energy of the modes, the admixture of a vibrational component, and the observation of the modes by means of neutron scattering, the description of the polar modes given by Sokoloff [96] has to be modified. The modes considered by Sokoloff are polar magnons with a spin quantum number  $S^z = 1$ , which correspond to electron transitions between Wannier states with different spin. Their energies are of the same order of magnitude as the exchange splitting  $\Delta E_d$  between the 3d bands, which is about  $0.35 \text{ eV} = 0.026 \text{ Ry}$  for Ni [97] (corresponding to a frequency  $\nu \approx 85 \text{ THz}$ ). In figure 2.5, where a value  $\Delta E_d = 0.07 \text{ Ry}$  has been used, the branches of the polar magnons would be expected in the energy interval between 0.01 and 0.07 Ry. The neutron scattering cross section of polar magnons is related to the correlation functions  $\langle S^+ S^- \rangle_T$  and  $\langle S^- S^+ \rangle_T$  in (3.34) and is

found to be extremely small except in the region of  $(Q, \omega)$ -space where the flat branches corresponding to the polar modes cross the magnon dispersion relation. Hence Sokoloff concludes that outside this region the polar magnons are not observable by means of neutrons.

The excitations observed in the present experiments have in some respects quite different properties. In the first place they do not possess a magnetic moment (i.e.  $S^z = 0$ ), and the electron transition which leads to the formation of the mixed excitation must therefore connect Wannier states with the same spin. In terms of Wannier functions, the states  $w_{j\downarrow}(\underline{r}-\underline{L})$  are all occupied, whereas the number of holes in the upper states  $w_{j\uparrow}(\underline{r}-\underline{L})$  is determined by the condition that the average number of unoccupied  $\uparrow$  states per lattice site should be  $\approx 0.6$ . A polar electron excitation with  $S^z = 0$  may be visualized as a transition of an electron from the state  $w_{j\uparrow}(\underline{r}-\underline{L})$  to an unoccupied state  $w_{j\uparrow}(\underline{r}-\underline{L}')$  localized at a nearest neighbour site of  $\underline{L}$ , which results in final electron configurations  $(3d)^9$  and  $(3d)^{10}$  at the sites  $\underline{L}$  and  $\underline{L}'$ , respectively. Since the excitation must be compatible with the symmetry of the lattice, the transferred electron is distributed over the 12 nearest neighbour sites of  $\underline{L}$ , in such a way that the eigenfunction of the final state transforms as an irreducible representation of the point group of the 13 lattice sites considered in this example. This means that the electron performs a hopping motion between equivalent lattice sites. Obviously, the same arguments may be used in the case where a hole is distributed over the nearest neighbour sites of  $\underline{L}'$ . On a local scale, these polar excitations are very similar to the polar model proposed by Van Vleck [10] to describe the electronic and magnetic properties of nickel. In this model it is assumed that 60% of the Ni atoms is in the  $(3d)^9$  configuration and 40% in the  $(3d)^{10}$  configuration, these two configurations being continuously redistributed over the lattice sites. The redistribution may be realised by a hopping of holes from atom to atom.

It seems possible that the mixed excitations observed in the present scattering experiments are polar modes, similar to the one described above. In a neutron scattering (energy loss) process a polar excitation may be created from the ground state where the charge distribution has the periodicity of the crystal lattice. It is quite difficult to estimate the



energy difference between the ground state and the excited state, because it may be expected that the perturbation in the charge distribution due to the hopping 3d holes will be compensated to a large extent by the 4s electrons (cf. ref. [101]). Moreover, the electronic excitation is mixed with a perturbation of the lattice, which means that a part of the energy transferred to the specimen is absorbed by the lattice (see section 7.5).

The admixture of a vibrational component to the electron-hole excitation is of importance for the observation of the excitations by means of neutrons. In Sokoloff's description of polar magnons the interaction between these electronic excitations and the lattice is neglected. For excitations with frequencies much larger than the phonon frequencies this approximation is justified, because the lattice is unable to adapt itself to the rapid oscillation of the electron between the different lattice sites. If, however, like it seems to be the case here, the frequency of the polar mode is within the phonon frequency band, a strong coupling with the lattice is expected. When a localized, polar electron excitation with a low frequency  $\omega_1$  is created, the atoms in the perturbed region start to oscillate about their equilibrium positions  $\underline{r}$  with the same frequency  $\omega_1$  and polarization vectors  $\underline{\xi}_1$ . The directions of the polarization vectors are directly related to the transformation properties of the polar excitation, and may be determined by means of projection operators if the irreducible representation belonging to the polar electron excitation is known. The coupling between the electronic mode and the lattice is equally important in a scattering process. It may be expected that it is possible to induce electron transitions between Wannier states by creating a local disturbance in the lattice periodicity. Hence, creation of mixed electronic-vibrational modes with low frequencies may occur in neutron scattering processes where a number of atoms in a relatively small region of the crystal lattice is displaced from their equilibrium positions. In such a situation, a redistribution of the electrons over the vibrating atoms may even result in a state which has a lower energy. If this is the case, the creation of a mixed mode requires less energy than the creation of a purely vibrational mode (see section 7.5).

The neutron scattering cross section of a mixed excitation may be calculated by means of the general expression (3.2), where both nuclear and magnetic

interactions should be taken into account. If one considers the inelastic scattering by a single localized excitation, the integrations over  $\underline{r}$  and  $\underline{r}'$  in (3.2) may be restricted to the perturbed region of the crystal. Decomposition of the correlation function  $\langle \dots \rangle_T$  in (3.2) into a nuclear and a magnetic part, as applied in the derivation of (3.18) and (3.31), is not possible in this case, because the instantaneous positions of the oscillating electron and atoms are correlated. For nickel the situation is more favourable, because the magnetic scattering by the electron is small in comparison with the nuclear scattering, and may be neglected in first approximation. Hence the main contribution to the cross section of a mixed mode in nickel is given by eq. (3.12), where the summation over  $\underline{l}$  and  $\underline{l}'$  is restricted to the lattice sites in the perturbed region.

It may seem odd that the observed cross sections, which clearly depend on the magnetization direction, should be mainly due to interaction with the nuclei. This paradox may be explained by the fact that the distribution of the electron over the lattice sites and the atomic displacement vectors  $\underline{u}_l(t)$  are governed by the magnetization direction, as will be shown for the simplified case considered below.

#### Symmetry properties of polar excitations

In order to show that the experimental results can be interpreted, at least qualitatively, in terms of scattering by polar electron excitations, we shall consider a very simple model, which involves only 13 lattice sites. It will be assumed that the electron-hole excitation consists of a hole localized at site  $\underline{1}$  and an electron distributed over the nearest neighbour sites  $\underline{2}, \dots, \underline{13}$  (see figure 7.1). Furthermore, we assume that the Wannier functions  $w_{j\uparrow}(\underline{r}-\underline{l})$ , belonging to the states occupied by the electron, are characterized by the same indices  $j\uparrow$  for each  $\underline{l}$ , and spherically symmetric. Under these conditions, the eigenfunction of a localized electron-hole excitation is a vector  $\underline{\psi}$  with 13 components  $\psi_{\underline{l}}$ , where the subscript refers to the lattice sites. If  $\underline{\psi}$  is normalized by

$$\sum_{\underline{l}=1}^{13} \psi_{\underline{l}}^* \psi_{\underline{l}} = 1,$$

the probability to find the electron at site  $\underline{l}$  is equal to  $\psi_{\underline{l}}^* \psi_{\underline{l}}$ . Moreover, each  $\underline{\psi}$  transforms according to an irreducible representation of the point group of the set of 13 lattice sites.

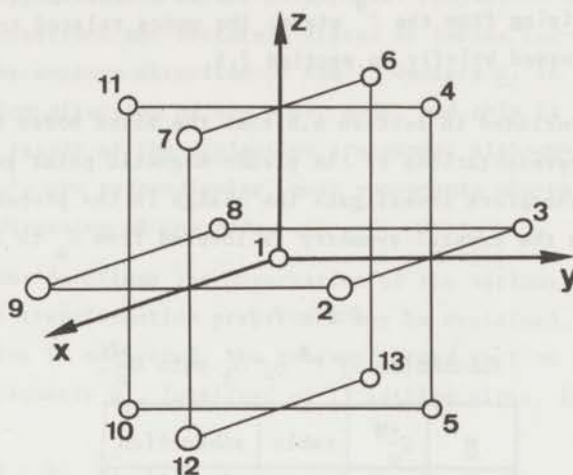


Figure 7.1.

*Lattice sites involved in a nearest-neighbour polar mode.*

The number of polar modes and their eigenvectors may be determined by means of the decomposition formulae (2.5) and (2.6), and the projection operators (2.7). Both in the paramagnetic and ferromagnetic phase there are 12 polar modes and 1 "acoustic" mode, the latter consisting of an electron and hole at site 1. In the paramagnetic (cubic) phase the modes transform as the irreducible representations of  $G_o = O_h$ . The decomposition yields

$$\Gamma = 2\Gamma^1 \oplus \Gamma^3 \oplus \Gamma^5 \oplus \Gamma^9 \oplus \Gamma^{10} \quad (7.2)$$

where  $\Gamma^5$ ,  $\Gamma^9$  and  $\Gamma^{10}$  are three-dimensional,  $\Gamma^3$  two-dimensional and  $\Gamma^1$  one-dimensional (cf. table A.15).

In a ferromagnetic single domain a number of degeneracies is removed, and the electron distribution over the lattice sites is changed as a result of spin-orbit interaction. Since the observed modes have almost equal frequencies, they should probably be interpreted as nearly degenerate modes that originate from the same degenerate mode in the cubic phase. It has been concluded earlier (cf. section 6.6) that the mixed modes must transform as odd representations, if the point group contains I. Consequently, the mixed modes

can only originate from the three-fold degenerate states  $\Gamma^9$  or  $\Gamma^{10}$  in the cubic phase. In the following interpretation we shall consider the mixed modes arising from the  $\Gamma^9$  state; the modes related to the  $\Gamma^{10}$  state are discussed briefly in section 7.5.

It has been concluded in section 6.6 that the mixed modes transform as irreducible representations of the pseudo-magnetic point groups  $G_o^{+M}(\underline{q})$ , and we shall therefore investigate the change in the properties of the  $\Gamma^9$  states when the crystal symmetry is lowered from  $G_o$  to  $G_o^{+M}$ .

Table 7.1.

Subduction of  $\Gamma^9$  of  $O_h$  onto  $G_o^{+M}$ .

$\underline{M}$	$G_o^{+M}$	table	subduction
[001]	$D_{4h}$	A.12	$\Gamma^9 \oplus \Gamma^{10}$
[110]	$D_{2h}$	A.8	$\Gamma^6 \oplus \Gamma^7 \oplus \Gamma^8$
[111]	$D_{3d}$	A.14	$\Gamma^5 \oplus \Gamma^6$

In table 7.1 the subduction of the representation  $\Gamma^9$  of  $O_h$  onto the subgroups  $G_o^{+M}$  is given for the domains of interest. The eigenvectors  $\underline{\psi}$  of these polar modes may be constructed by means of projection operators and are given in appendix C, table C.1. It is found that the probability distribution of the electron is strongly influenced by the magnetization direction. Let us consider the  $\Gamma^9$  mode in the [001] domain as an example: the electron is found with equal probability 1/8 at the sites 4,5,6,7,10,11,12,13, and performs an oscillation along the magnetization direction. By comparing the vector components  $\psi_z$  and the relative positions of the sites in figure 7.1 it is seen that the three polar electronic modes correspond to electron oscillations in mutually perpendicular directions, one direction being parallel to  $\underline{M}$ . These directions will be denoted as the polarization directions of the modes.

For the interpretation of the scattering cross section it is necessary to derive the symmetry properties of the displacements  $\underline{u}_l$  of the lattice sites, induced by the polar electron excitation. The oscillations of the 13 lattice sites in figure 7.1 may be described by means of a 39-dimensional vector  $\underline{u}$

with components  $u_l^x$ ,  $u_l^y$  and  $u_l^z$ , which transforms according to the same irreducible representation as the polar mode. Projection operators have been used to construct the vectors  $\underline{u}$  listed in tables C.2-C.4. One may expect that the average direction of the 13 vectors  $\underline{u}_l$  is parallel with the polarization direction of the polar mode, and this is indeed confirmed by the result of the projection procedure. Although some components of the  $\underline{u}_l$ 's are perpendicular, most components are parallel with the polarization direction of the mode.

After these considerations the observation of the various mixed modes with different transformation properties may be explained. If the magnetic scattering is neglected, the coherent cross section of a mixed mode with a frequency  $\omega_1$ , localized at 13 lattice sites, is given by

$$\frac{d^2\sigma_n}{d\Omega dE} = \frac{k}{k_0} \frac{1}{2\pi\hbar} \int_{-\infty}^{+\infty} dt \exp(-i\omega t) \exp\{-2W(Q)\} \times \\ \langle b \rangle^2 \sum_{l=1}^{13} \sum_{l'=1}^{13} \exp\{iQ \cdot (l' - l)\} \langle \{Q \cdot \underline{u}_l(0)\} \{Q \cdot \underline{u}_{l'}(t)\} \rangle_T, \quad (7.3)$$

where  $\underline{u}_l(t) = \underline{u}_l(0) \exp(i\omega_1 t)$ . Expression (7.3) may be written in a more concise way if the dynamic structure factor  $F(Q)$  of the mode is introduced:

$$F(Q) = \sum_{l=1}^{13} \{Q \cdot \underline{u}_l(0)\} \exp(-iQ \cdot l). \quad (7.4)$$

Substitution of (7.4) into (7.3) yields

$$\frac{d^2\sigma_n}{d\Omega dE} = \frac{k}{k_0} \exp\{-2W(Q)\} \langle b \rangle^2 \langle F^*(Q) F(Q) \rangle_T \delta(\hbar\omega - \hbar\omega_1). \quad (7.5)$$

The scattering cross section of a mixed mode in a point  $Q$  is directly related to its structure factor, which may be derived from the vectors  $\underline{u}_l$  tabulated in the tables C.2, C.3 and C.4. For each of the modes considered in appendix C the value of  $F(Q)$  was determined for those points  $Q$  that have been investigated in the present work (cf. tables C.5, C.6 and C.7). In each case the structure factor vanishes in a number of points  $Q$ . This is actually a consequence of the symmetry properties of the mode, and could have been predicted on basis of the selection rules for neutron scattering. Some of the observed modes may be identified unambiguously by

means of the structure factor tables. The excitations observed at  $\underline{Q} = (0,0,1)$  and  $\underline{Q} = (1,0,0)$  in the  $[001]$  domain are the mixed modes transforming as  $\Gamma^9$  and  $(\Gamma^{10})_1$  of  $D_{4h}$ , respectively. The modes observed at  $\underline{Q} = (0,0,1)$  and  $(\bar{2},2,0)$  in the  $[110]$  domain correspond to the modes transforming as  $\Gamma^8$  and  $\Gamma^7$  of  $D_{2h}$ , respectively. This interpretation is in agreement with the final selection of representations given in table 6.7, where the mixed modes were considered as excitations with a wave vector  $\underline{q}$ . The correspondence between the selected representations of  $G_{\underline{0}}^{+M}(\underline{q})$  in table 6.7 and the representations of  $G_{\underline{0}}^{+M}$  in table 7.1 is evident for  $\underline{q} = (0,0,1)$  in the  $[001]$  and  $[110]$  domains, because  $G_{\underline{0}}^{+M}(\underline{q})$  and  $G_{\underline{0}}^{+M}$  are identical. Moreover, it can be shown that the polar mode transforming as  $(\Gamma^{10})_1$  of  $D_{4h}$ , transforms as  $\Gamma^8$  of  $G_{\underline{0}}^{+M}(\underline{q}) = D_{2h}$  if it is interpreted as an excitation with wave vector  $\underline{q}$ .

In the time-of-flight experiments performed close to the points  $\underline{Q} = (1,1,0)$ ,  $(0,1,1)$  and  $(1,\bar{1},0)$ , the scattering by the mixed modes was too weak to be detected (cf. tables 6.3, 6.4 and 6.5). For one (in some points: two) of the three mixed modes, scattering in these points is forbidden by symmetry, but the remaining mode(s) should have been observable according to the structure factor tables C.5 - C.7. Consider, for example, the experiment at  $\underline{Q} = (0,1,1)$  in the  $[001]$  domain, shown in figure 6.4, where scattering by the  $(\Gamma^{10})_1$  mode is forbidden. Since no scattering from the other two modes was observed, it seems probable that their structure factors in  $\underline{Q} = (0,1,1)$  are very small. If one assumes, as a first approximation, that the structure factors of these other modes are zero, some additional relations between the displacement vectors of nonequivalent atoms may be derived. It should be emphasized, however, that the derivation of these relations, which is given below for different modes, is based on a very simple model. In reality, the number of lattice sites involved in the mode is expected to be of the order of 1000 (see section 7.4).

Let us consider a relatively simple case: the  $\Gamma^9$  mode in the  $[001]$  domain. The displacement vectors  $\underline{u}_i$  are characterized by four amplitudes, denoted by a, b, c and d in table C.2, where the latter three refer to displacements along the z direction. From the fact that the mode was not observed in  $\underline{Q} = (0,1,1)$ , one may conclude that  $F(0,1,1) = b-4c \approx 0$ . This means that the oscillations of the atoms 1,2,3,8 and 9 are in phase, the

amplitudes for the atoms 2,3,8 and 9 being 1/4 of the amplitude for atom 1. Hence one obtains the following values for  $F(\underline{Q})$  in  $\underline{Q} = (0,0,1)$  and  $(0,0,2)$ :  $F(0,0,1) = 8c-8d$ ,  $F(0,0,2) = 8c+8d$ . As the scattering by the mode in  $(0,0,1)$  is rather large, it seems likely that  $c$  and  $d$  have opposite signs, i.e. the atoms in alternate layers move in opposite directions. The vibration of the atoms is therefore very similar to a longitudinal lattice vibration with wave vector  $\underline{q} = (0,0,1)$ . It may be expected that the scattering by the  $\Gamma^9$  mode is weak in  $(0,0,2)$ , because  $F(0,0,2)$  is small if  $c$  and  $d$  have opposite signs. The scattering cross section of the  $\Gamma^9$  mode in  $\underline{Q} = (\frac{1}{2}, \frac{1}{2}, \frac{1}{2})$  is determined by  $F(\underline{Q}) = \frac{1}{2}(b+8a)$ , where  $b$  denotes the displacement of atom 1 along the  $z$  axis and  $a$  the displacements of eight atoms perpendicular to the  $z$  axis. On basis of the vibration pattern of the atoms along the  $z$  direction, which was suggested above, it seems likely that a positive displacement  $u_1^z$  is accompanied by positive displacements  $u_7^x$  and  $u_4^y$ , and negative displacements  $u_6^x$  and  $u_{11}^y$  (see figure 7.1). In other words, the amplitudes  $a$  and  $b$  for  $\Gamma^9$  in table C.2 have opposite signs. Consequently, a small cross section in  $(\frac{1}{2}, \frac{1}{2}, \frac{1}{2})$  may be expected if  $|a|$  is small in comparison with  $|b|$ .

A similar discussion may be given for the  $(\Gamma^{10})_1$  mode in the  $[001]$  domain, which was observed in  $\underline{Q} = (1,0,0)$ , but not in  $(1,1,0)$  (cf. table 6.3). According to table C.2 the vibration pattern of the atoms is determined by six independent parameters, of which  $a$ ,  $b$ ,  $c$  and  $d$  refer to displacements along the  $x$  direction. If it is assumed that the effect of the spin-orbit coupling on the displacements is small, one may reduce the number of parameters by using the approximations  $b = d$  and  $e = -f$ , which leads to the result  $F(1,0,0) = a+4c-8d$ ,  $F(1,1,0) = a-4c$ . From the intensities in  $(1,0,0)$  and  $(1,1,0)$  one may finally conclude that  $a = 4c$ , and that  $c$  and  $d$  have opposite signs, which corresponds to a vibration pattern similar to a longitudinal lattice vibration with  $\underline{q} = (1,0,0)$ . In the same way it may be shown that the  $(\Gamma^{10})_2$  mode resembles a localized longitudinal vibration with  $\underline{q} = (0,1,0)$ . Hence the three mixed modes in the  $[001]$  domain are very similar, and it is therefore not surprising that their frequencies are found to be equal within the experimental accuracy.

Next, we consider the mixed modes in the  $[110]$  domain, for which the structure factors are listed in table C.6. If one compares the displacement vectors in the tables C.2 and C.3, it is seen that the vibration pattern of the  $\Gamma^8$  mode

in the  $[110]$  domain is similar to that of the  $\Gamma^9$  mode in the  $[001]$  domain. This similarity is confirmed by the fact that the frequencies of the modes are approximately equal. If the effects of the spin-orbit coupling are assumed to be small, one may reduce the number of parameters for the  $\Gamma^8$  mode by taking  $a \approx 0$  and  $d \approx e$ . After these simplifications one obtains  $F(-3/2, 3/2, 3/2) = (3/2)_x(c+8b)$  and since the  $\Gamma^8$  mode was not observed in  $Q = (-3/2, 3/2, 3/2)$  (cf. figure 6.8) one may conclude that  $c+8b \approx 0$ . This means that the amplitude of atom 1 along the z axis is about 8 times larger than the amplitudes of the atoms 4,5,6,7,10,11,12 and 13 perpendicular to the z axis.

The vibration pattern of the  $\Gamma^7$  mode in the  $[110]$  domain may be expected to be essentially different, because this mode is observable at the zone centre  $(\bar{2}, 2, 0)$ , and because it has a larger frequency than the modes considered above ( $\approx 6.7$  THz instead of  $\approx 4$  THz). The mode could not be observed in  $(\bar{1}, 1, 0)$ , and one may therefore conclude that  $a+2b+2c \approx 4d+4e$  (cf. table C.6). A large cross section in  $(\bar{2}, 2, 0)$  is expected if a, b, c, d and e have the same sign, which corresponds to a vibration pattern similar to a longitudinal vibration with  $q = (0, 0, 0)$  and  $\xi = 2^{-1/2}(\bar{1}, 1, 0)$ . Since the  $\Gamma^7$  mode was not observable in  $Q = (-3/2, 3/2, 3/2)$ , it seems probable that  $a+2b+4f \approx 2c$ .

It has been found experimentally that the three mixed modes in the  $[110]$  domain are not observable in  $(-3/2, 3/2, 3/2)$ . The three mixed modes in the  $[001]$  domain are very similar to the  $\Gamma^8$  mode in the  $[110]$  domain, and one may therefore expect that these modes are not observable in the zone boundary points L, either. Consequently, the mixed mode observed in  $(3/2, 3/2, 3/2)$  for the multidomain sample (cf. figure 5.7) should probably be ascribed to  $[111]$  domains. It seems likely that this mode corresponds to the  $\Gamma^5$  mode in the  $[111]$  domain. Inspection of table C.4 shows that the displacement vectors  $u_L$  for the  $\Gamma^5$  mode are mainly along the  $[111]$  direction. The components of  $u$  along the  $[111]$  direction are equal for the atoms 2,4,7,8,10 and 13, and the same applies to the displacement components along  $[111]$  for the atoms 3,5,6,9,11 and 12. A large cross section of the  $\Gamma^5$  mode in  $Q = (3/2, 3/2, 3/2)$  may be expected if these two sets of atoms vibrate in opposite directions. If this is the case, the mode resembles a longitudinal vibration with  $q = (\frac{1}{2}, \frac{1}{2}, \frac{1}{2})$ . From the absence of scattering in  $Q = (0, 0, 1)$  and  $(0, 1, 1)$  (see table 6.5 and figures 6.1 and 6.2) one may conclude that



the structure factors in these points, which are given in table C.7, are small. This may be explained if it is assumed that the displacements perpendicular to  $[111]$  are small, and that the absolute values of the displacements along  $[111]$  are approximately equal. In that case one has  $b = d \approx -c \approx -e$ ,  $F(0,0,1) = a$  and  $F(0,1,1) = 2a$ , which implies that only atom 1 contributes to the scattering. If no simplifying assumptions are made for the amplitudes, the small values of the two structure factors may be interpreted in terms of the following relations:  $\frac{1}{2}a = b+c \approx d+e$ .

We shall not proceed to a discussion of the  $\Gamma^6$  mode in the  $[110]$  domain and the  $\Gamma^6$  modes in the  $[111]$  domain, because these modes have not been observed in the present scattering experiments. An investigation of the  $\Gamma^6$  mode in the  $|110|$  domain should preferably be performed along the  $[110]$  direction; the two modes  $(\Gamma^6)_1$  and  $(\Gamma^6)_2$  in the  $[111]$  domain are expected to be observable along  $[11\bar{2}]$  and  $[\bar{1}10]$ , respectively.

Although the general behaviour of the scattering cross section can be explained by means of (7.3), difficulties are encountered when a quantitative comparison is made between the cross sections for energy loss in  $\underline{Q} = (1,0,0)$  and  $(3,0,0)$ . Since these scattering vectors differ by a reciprocal lattice vector  $\underline{\tau}$ , for which  $\exp(i\underline{\tau} \cdot \underline{L}) = 1$  (see (2.2)), the phase factors  $\exp\{i\underline{Q} \cdot (\underline{L}' - \underline{L})\}$  are equal for the two considered scattering vectors, and hence one would expect the cross section to be proportional to  $Q^2 \exp\{-2W(\underline{Q})\}$ . According to the values listed in table 7.2 the scattering cross section in  $(3,0,0)$  should be a factor 8 larger than in  $(1,0,0)$ . A rough estimate of the intensities in these points yields 190 n/10 min. in  $(3,0,0)$  (figure 5.3,  $\tau = 1.0$ ) and 160 n/10 min. in  $(1,0,0)$  (figure 5.12). For the determination of the latter value the background in figure 5.12 was assumed to be 1100 n/50 min. at  $\nu = 4.5$  THz. Thus one obtains the ratio  $I(3,0,0)/I(1,0,0) \approx 1.2$  between the observed intensities, which is in disagreement with the expected ratio.

This discrepancy may possibly be interpreted as an indication that the theory of inelastic scattering, summarized in section 3.4, does not give a proper quantitative description of the scattering close to the zone boundaries. It has been pointed out in section 5.3.1 that the scattering cross section of the mixed mode for energy loss processes close to the zone boundaries is much larger than one would expect on basis of the detailed-balance condition

(3.22). It seems probable that these discrepancies between the experimental results and the scattering theory are related to each other. A possible explanation of the unexpected results is suggested in the next section, where the attention is focused on the detailed-balance condition.

Table 7.2.

Comparison of scattering cross sections in (1,0,0) and (3,0,0)

$\underline{Q}$	$ \underline{Q}  (\text{\AA}^{-1})$	$\exp(-2W)$	$Q^2 \exp(-2W)$	exp. value $I(\underline{Q})$
(1,0,0)	1.783	0.984	3.128	$\approx 16$ n/min.
(3,0,0)	5.349	0.863	24.69	$\approx 19$ n/min.

#### 7.4. The detailed-balance condition

As mentioned in section 3.4, the ratio between the cross sections for energy gain and energy loss scattering is determined by the detailed-balance condition (3.22), which is valid if (a) the scattering sample is in thermal equilibrium and (b) the scattering process is reversible. In the actual experimental configuration the final neutron wave vector in the energy loss scan is not equal to the initial wave vector in the energy gain scan, and (3.22) should be rewritten as

$$\left(\frac{d^2\sigma}{d\Omega dE}\right)_{\text{loss}} = \frac{(k/k_o)_{\text{loss}}}{(k/k_o)_{\text{gain}}} \exp\left(\frac{\hbar\omega}{k_B T}\right) \times \left(\frac{d^2\sigma}{d\Omega dE}\right)_{\text{gain}} \quad (7.6)$$

The calculation of the ratio between the two cross sections for  $\nu = 5.0$  THz,  $T = 298$  K,  $k_{\text{loss}} = 3.617 \text{\AA}^{-1}$  and  $k_{\text{gain}} = 4.986 \text{\AA}^{-1}$  yields

$$\left(\frac{d^2\sigma}{d\Omega dE}\right)_{\text{loss}} = 1.30 \times \left(\frac{d^2\sigma}{d\Omega dE}\right)_{\text{gain}} \quad (7.7)$$

A comparison between the experimental results in the figures 5.3 and 5.4 shows that the scattering by the mixed mode observed at  $\underline{Q} = (2,0,0)$  is in approximate agreement with (7.7). Close to  $\underline{Q} = (3,0,0)$ , however, the difference between energy loss and energy gain scattering is much larger than predicted by the detailed-balance condition. It may be seen

from figures 5.6 and 5.12 that similar discrepancies between the cross sections are found close to  $\underline{Q} = (1,0,0)$  and  $\underline{Q} = (-3/2, 3/2, 3/2)$ .

As the detailed-balance condition is directly related to two fundamental assumptions in the scattering theory, it is of interest to consider why the condition might be violated in the present scattering experiments. It seems very unlikely that the scattering sample would not be in thermal equilibrium, because the perturbations introduced by inelastic thermal neutron scattering are negligible in comparison with the thermal disorder already present. Hence the observed deviation from (7.6) should probably be interpreted as an indication that the neutron scattering by the mixed mode is not reversible. Below, we shall suggest a possible explanation, which is based on the interaction of the localized polar mode with the surrounding lattice.

The mixed polar modes introduced in the previous section are subject to interactions with other excitations, in particular with the phonons. The interaction with the transverse phonons near the zone boundaries is strong because the frequencies are approximately equal. This interaction has been discussed in connection with the observation of forbidden phonon scattering. Moreover, the interaction with longitudinal phonons has been observed in some experiments (cf. figure 6.9). As a result of the interaction between the mixed mode and the phonons, relaxation effects may be expected. If the polar mode is initially created as an excitation localized at, for example, 13 lattice sites, it is expected to spread out over more distant neighbours in the course of time, while it retains the same transformation properties. Several properties of the mixed mode may be affected by this relaxation: the phase differences between the vibrating atoms, the electron distribution, the displacements  $\underline{u}_l$ , and even the frequency. In general, the localized mode will acquire properties which are resembling those of a collective lattice vibration.

It seems possible that the violation of the detailed-balance condition may be explained if one assumes that the relaxation time is large in comparison with the time involved in the neutron scattering process. In that case the mixed mode created by a neutron has a more localized character than the relaxed modes which are observed in the energy gain experiments. In other words, the final state in the energy loss experiment is not identical to the initial

state in the energy gain experiment, which implies that condition (b) on page 40 does not hold.

The observation time may be estimated by means of the uncertainty relation  $\Delta E \approx \hbar/\Delta t$ . In the time-of-flight experiments the mixed mode was observed with a frequency width of the order 0.25 THz ( $\Delta E \approx 1$  meV), which corresponds to an observation time of approximately  $0.65 \times 10^{-12}$  s. On the other hand, the relaxation time is expected to be of the order  $1 \times 10^{-12}$  s, which is only slightly larger than the time involved in the scattering process. Still, it seems possible that a mixed mode, created in an energy loss process, does not reach its equilibrium state during the observation time. The distance covered by the neutron during this time ( $\approx 17 \text{ \AA}$ ) is about 5 times larger than the lattice constant ( $a = 3.524 \text{ \AA}$ ), and the set of lattice sites introduced in section 7.3 can therefore only be considered as a first approximation in the description of the experimental results.

The mixed modes observed in energy gain processes are in equilibrium with the surrounding lattice, and may be assumed to involve a large number of lattice sites. In this larger system the sites can be grouped into sets that oscillate with the same phase and amplitude, in a similar way as was done for the 13-site model. Since the number of lattice sites is larger, the number of independent parameters in the displacement vectors  $\underline{u}_l$  is larger, and one may expect that the scattering cross section of these modes does not show the pronounced maxima at the zone boundaries, that are characteristic for a localized mode where nearest neighbour sites oscillate in opposite phase. This is in agreement with the observation that the cross section for energy gain scattering is approximately independent of  $\underline{Q}$  (cf.  $\underline{Q} = (2,0,0)$  and  $\underline{Q} = (3,0,0)$  in figure 5.4).

Our assumption that the mixed modes created by a neutron are not in equilibrium with the lattice, is supported by the results of the constant- $\underline{Q}$  experiments along the  $[\bar{1}11]$  direction on the multidomain sample (cf. figure 5.7). Close to the zone boundary the energy transfer between the neutron and the mixed mode is clearly different in the energy gain and energy loss experiment; the energy required for the creation of the mode is larger than the energy released in the annihilation process.

### 7.5. Conclusion

This investigation grew out of earlier work on nickel alloys [20]. The polar modes observed in the present experiments on nickel show a remarkable similarity with the subject of that investigation: the magnetic impurity modes of a nearest-neighbour pair of iron atoms in Ni(Fe) [98]. The experiments on Ni(4%Fe) were aimed at a search for a possible impurity mode transforming as the odd representation  $\Gamma^6$  of  $D_{2h}$ . In view of the expected variation in the cross section of this mode as a function of  $Q$ , the measurements were concentrated near the zone boundary [20]. Obviously, this region in  $Q$ -space is also favourable for the observation of other excitations transforming as odd representations, such as polar electron-hole excitations.

In the interpretation given in section 7.3 the attention has been focused on the  $\Gamma^9$  polar mode in a nearest-neighbour model, and naturally the question arises whether one of the other polar modes could be the origin of the observed scattering. Inspection of the decomposition (7.2) shows that, besides  $\Gamma^9$ , only one other odd representation ( $\Gamma^{10}$ ) is present for the 13-site model. Subduction of  $\Gamma^{10}$  onto the point groups  $G_o^{+M}$  leads to the result that two of the three modes originating from  $\Gamma^{10}$  of  $O_h$  in the cubic phase, may induce lattice vibrations in single domains. The lattice site displacements  $u_l$  of the resulting mixed modes transform as  $\Gamma^{10}$  of  $D_{4h}$  in the  $[001]$  domain,  $\Gamma^6$  and  $\Gamma^7$  of  $D_{2h}$  in the  $[110]$  domain and  $\Gamma^6$  of  $D_{3d}$  in the  $[111]$  domain (see tables C.2, C.3 and C.4, respectively). It is obvious that the experimental results cannot be explained on basis of this mode, because it does not lead to the formation of mixed modes transforming as  $\Gamma^9$  of  $D_{4h}$  and  $\Gamma^8$  of  $D_{2h}$ , as required by the results in table 6.7.

Only little attention has been given to the observed interaction between the mixed modes and the magnons along the  $[r00]$  direction, mainly because the experimental results are scarce. On basis of the preceding interpretation of the mixed modes it is possible to make some remarks with regard to this interaction. As the magnons have a spin  $S^z = 1$ , the coupling with mixed modes (with  $S^z = 0$ ) can only be due to an interaction Hamiltonian which has the symmetry of  $G_o^M(\underline{q})$ . Spin-orbit coupling seems to be the most probable interaction mechanism. The selection rules applicable to the interaction between mixed modes and magnons may be found in table

B.2: coupling is possible if the mixed modes transform as  $\Gamma^3$  of  $C_4$ ,  $\Gamma^2$  of  $C_s$ , or  $\Gamma^1$  of  $C_1$ . To apply the selection rules the compatibility between the representations of  $G_o^{+M}$  and  $G_o^M(\underline{q})$  has to be determined for each single domain, which leads to the results in table 7.3. It turns out that the polar modes originating from the  $\Gamma^9$  modes in the cubic phase, may interfere with the magnons in each of the domains investigated in this work.

Summarizing the discussion presented in this chapter, one may conclude that almost all experimental results can be explained, at least qualitatively, by polar electron-hole excitations interacting with lattice vibrations. Spin-orbit coupling plays a dominant role in the observed phenomena. When the crystal is magnetized, two characteristic properties of the mixed mode, viz. the electron distribution over the sites, and the amplitudes and phases of the displacement vectors  $\underline{u}_l(t)$ , are governed by spin-orbit coupling. Secondly, the interaction between the mixed modes and the magnons would be impossible in absence of spin-orbit coupling. The symmetry properties of the

Table 7.3.

Subduction table for the representations of the mixed modes onto the magnetic point groups  $G_o^M(\underline{q})$  for  $\underline{q} = (0,0,\tau)$  and  $(\tau,0,0)$ .

	$\underline{M} // [001]$			$\underline{M} // [\bar{1}10]$			$\underline{M} // [111]$			
$G_o^{+M}$	$D_{4h}$	$\Gamma^9$	$\Gamma^{10}$	$D_{2h}$	$\Gamma^6$	$\Gamma^7$	$\Gamma^8$	$D_{3d}$	$\Gamma^5$	$\Gamma^6$
$G_o^M(0,0,\tau)$	$C_4$	$\Gamma^1$	$\Gamma^3 \oplus \Gamma^4$	$C_s$	$\Gamma^2$	$\Gamma^1$	$\Gamma^1$	$C_1$	$\Gamma^1$	$\Gamma^1 \oplus \Gamma^1$
$G_o^M(\tau,0,0)$	$C_s$	$\Gamma^2$	$\Gamma^1 \oplus \Gamma^1$	$C_1$	$\Gamma^1$	$\Gamma^1$	$\Gamma^1$	$C_1$	$\Gamma^1$	$\Gamma^1 \oplus \Gamma^1$

mixed modes determine the characteristic features of the scattering cross section, in particular the peculiar variation of the cross section as a function of the magnetization direction. Polar modes of the type considered above are most easily observed if the scattering vector  $\underline{Q}$  is either parallel with or perpendicular to the magnetization direction. Along these directions the cross section for energy loss scattering is a periodic function of  $\underline{Q}$  due to interference between the scattering contributions from different sites. If, on the other hand,  $\underline{Q}$  is not oriented along or perpendicular to  $\underline{M}$ , the scattering cross section is in general small as a result of destructive interference.

Other aspects of the experimental data, in particular the constant frequency of each of the modes, and the irreversibility of the neutron scattering process due to relaxation effects, are related to the fact that the mixed mode is a localized excitation in interaction with its surroundings. The observation that the energy loss scattering does not vary appreciably with temperature is in accordance with the interpretation in terms of a single electron excitation connecting states close to the Fermi level.

A few comments should be added with regard to the frequency of the mixed modes. To explain the pronounced maxima in the energy loss cross section at the zone boundary points X and L, we had to assume that the vibrations of the atoms in alternate layers perpendicular to  $\underline{Q}$  were in opposite directions, parallel and antiparallel with  $\underline{Q}$ . In this case, the oscillations of the atoms in the mixed mode are very similar to those in a longitudinal lattice vibration with a wave vector  $\underline{q}$  corresponding to X or L, the main difference being that the mixed mode involves only a small number of atoms. Still, one might expect that the frequency of the localized mode would be approximately equal to the frequency of the longitudinal phonon in X or L, if the coupling with the electron-hole excitation were "switched off". It seems therefore probable that the energy difference between the polar electron distribution and the periodic electron distribution is roughly equal to the energy difference between the longitudinal phonon and the mixed mode at the same point at the zone boundary. From the experimental results in  $\underline{Q} = (3,0,0)$  for the multidomain sample (cf. figure 5.5) one obtains in this way an estimated value for the energy of the electron excitation: - 17.8 meV. The minus sign indicates that in this exceptional case, where a local perturbation has been created in the lattice, the polar electron distribution has a lower energy than the periodic electron distribution. The value given above has been derived from the frequencies  $\nu = 8.55$  THz and 4.25 THz; accidentally, the difference is almost equal to the frequency of the mixed mode.

There is a striking similarity between the scattering by the mixed modes and the scattering by the perturbed  $\Delta_5$  and  $\Lambda_3$  phonons close to the points X and L (see figures 5.3, 5.4 and 5.6). The scattering by the perturbed phonons is obviously in disagreement with the detailed-balance condition. An explanation of this disagreement between energy loss and energy gain scattering in terms of relaxation effects, as presented in section 7.4

for the mixed modes, may be given if one assumes that the perturbation of the phonons is due to the interaction with the polar electron-hole excitations: As a consequence of the perturbation of the lattice, introduced in the course of the creation process, a localized electron-hole excitation is created in addition to the phonon. Since the polar electron excitations are essentially longitudinal modes, the interaction with the transverse phonons is weak. The coupling leads to a change in the direction of the polarization vector of the phonon and a slight change in the phonon frequency. Both effects have in fact been observed. If these mixed modes are initially created as strongly localized modes, which are not in equilibrium with the lattice, violation of the detailed-balance condition may be expected in this case, too.

For the theoretical description of the electrons in transition metals it is of interest that polar electron-hole excitations, in combination with lattice vibrations, are found to be present in nickel. From the fact that the frequencies of the mixed electronic-vibrational modes are well-defined, one may conclude that their life time must be larger than  $\approx 0.7 \times 10^{-12}$  s. Furthermore, it has been shown that these mixed modes, which have frequencies of the same order as the phonon frequencies, may be observed by means of neutron scattering. If a mixed mode is created in a neutron scattering process, it is fairly localized, but not in equilibrium with the surrounding lattice. It seems likely that mixed excitations with low frequencies are also present in other metals, especially in those metals where the electron-phonon interaction is strong. However, it is easier to perform an investigation on these modes in a ferromagnetic metal, because it is possible to distinguish the scattering by the modes from possible spurious scattering processes by applying a magnetic field along symmetry directions.



APPENDIX A

Character tables

In this appendix a compilation is given of the transformations and character tables used in the preceding chapters and in appendices B and C.

The proper rotations  $\{R|Q\}$  are defined by means of the following notation for the symmetry directions: [24]

$$\begin{array}{lll} \underline{a} : [110] & \underline{\alpha} : [\bar{1}\bar{1}1] & \underline{x} : [100] \\ \underline{b} : [1\bar{1}0] & \underline{\beta} : [\bar{1}1\bar{1}] & \underline{y} : [010] \\ \underline{c} : [101] & \underline{\gamma} : [11\bar{1}] & \underline{z} : [001] \\ \underline{d} : [\bar{1}01] & \underline{\delta} : [111] & \\ \underline{e} : [01\bar{1}] & & \\ \underline{f} : [011] & & \end{array}$$

The transformations are denoted by

- E : the identity operation,
- $C_{na}$ , etc.: rotation through  $2\pi/n$  in the right-hand screw sense about the  $\underline{a}$  direction,
- I : space inversion,
- $IC_{na}$ , etc.: improper rotation.

In table A.1 a list is given of the transformation matrices for the proper rotations R. The traces of the matrices  $D_{\frac{1}{2}}(R)$ , which are needed for the reduction of  $\Gamma_S^\alpha \otimes D_{\frac{1}{2}}$  into double-valued representations  $\Gamma_D^\beta$ , are listed in table A.2. In the following tables A.3 - A.15 the characters of the irreducible representations are given for 14 of the 32 point groups. The subscripts in  $\Gamma_S^\alpha$  and  $\Gamma_D^\beta$  have been omitted and the representations are denoted by a superscript only; in some cases the notation according to Bouckaert et al. (BSW) [44] is given in addition. A class of operations, which may consist of more than one element, is denoted by  $R_i$  in the tables A.5 - A.15. The characters for the "barred" rotations  $\bar{R}$  have been omitted from the tables. These may be derived by making use of the relations  $\chi(\bar{R}) = \chi(R)$  for the single-valued representations and  $\chi(\bar{R}) = -\chi(R)$  for the double-valued ones. In general the double-valued representations are listed only if they have actually been mentioned or used in the text. In the last column of each table the letters a, b or c indicate to which case the representation belongs with respect to time reversal. The phonon polarization vectors for the

doubly degenerate  $\Delta_5$  and  $\Lambda_3$  branches have been determined by means of the two-dimensional representations given in tables A.11 and A.13. The two-dimensional representations  $\Gamma^{10}$  of  $D_{4h}$  and  $\Gamma^6$  of  $D_{3d}$ , given in tables A.12 and A.14, respectively, have been used to determine the eigenvectors  $\underline{\psi}$  and  $\underline{u}$  for the polar modes (cf. appendix C). For the other two- and three-dimensional representations only the characters are tabulated. Finally, each table contains a list of the corresponding point groups  $G_o^M(Q)$ ,  $G_o^{+M}(Q)$ ,  $G_o^M(q)$ ,  $G_o^{+M}(q)$  or  $G_o(q)$  with their symmetry operations.

Table A.1.

Coordinate transformation matrices  $\underline{R}$

R	$\underline{R}$	R	$\underline{R}$	R	$\underline{R}$	R	$\underline{R}$
E	$\begin{pmatrix} 1 & 0 & 0 \\ 0 & 1 & 0 \\ 0 & 0 & 1 \end{pmatrix}$	$C_{2y}$	$\begin{pmatrix} \bar{1} & 0 & 0 \\ 0 & 1 & 0 \\ 0 & 0 & \bar{1} \end{pmatrix}$	$C_{2a}$	$\begin{pmatrix} 0 & 1 & 0 \\ 1 & 0 & 0 \\ 0 & 0 & \bar{1} \end{pmatrix}$	$C_{2e}$	$\begin{pmatrix} \bar{1} & 0 & 0 \\ 0 & 0 & \bar{1} \\ 0 & \bar{1} & 0 \end{pmatrix}$
$C_{2x}$	$\begin{pmatrix} 1 & 0 & 0 \\ 0 & \bar{1} & 0 \\ 0 & 0 & \bar{1} \end{pmatrix}$	$C_{2z}$	$\begin{pmatrix} \bar{1} & 0 & 0 \\ 0 & \bar{1} & 0 \\ 0 & 0 & 1 \end{pmatrix}$	$C_{2b}$	$\begin{pmatrix} 0 & \bar{1} & 0 \\ \bar{1} & 0 & 0 \\ 0 & 0 & \bar{1} \end{pmatrix}$	$C_{2f}$	$\begin{pmatrix} \bar{1} & 0 & 0 \\ 0 & 0 & 1 \\ 0 & 1 & 0 \end{pmatrix}$
$C_{4x}$	$\begin{pmatrix} 1 & 0 & 0 \\ 0 & 0 & 1 \\ 0 & \bar{1} & 0 \end{pmatrix}$	$C_{4z}$	$\begin{pmatrix} 0 & 1 & 0 \\ \bar{1} & 0 & 0 \\ 0 & 0 & 1 \end{pmatrix}$	$C_{2c}$	$\begin{pmatrix} 0 & 0 & 1 \\ 0 & \bar{1} & 0 \\ 1 & 0 & 0 \end{pmatrix}$	$C_{3\delta}$	$\begin{pmatrix} 0 & 1 & 0 \\ 0 & 0 & 1 \\ 1 & 0 & 0 \end{pmatrix}$
$C_{4x}^{-1}$	$\begin{pmatrix} 1 & 0 & 0 \\ 0 & 0 & \bar{1} \\ 0 & 1 & 0 \end{pmatrix}$	$C_{4z}^{-1}$	$\begin{pmatrix} 0 & \bar{1} & 0 \\ 1 & 0 & 0 \\ 0 & 0 & 1 \end{pmatrix}$	$C_{2d}$	$\begin{pmatrix} 0 & 0 & \bar{1} \\ 0 & \bar{1} & 0 \\ \bar{1} & 0 & 0 \end{pmatrix}$	$C_{3\delta}^{-1}$	$\begin{pmatrix} 0 & 0 & 1 \\ 1 & 0 & 0 \\ 0 & 1 & 0 \end{pmatrix}$

Improper rotations:  $\underline{I} = -\underline{E}$ ,  $\underline{IR} = -\underline{R}$

Table A.2.

Traces of the matrices  $D_{\frac{1}{2}}(R)$

R	TrD $_{\frac{1}{2}}$	R	TrD $_{\frac{1}{2}}$	R	TrD $_{\frac{1}{2}}$	R	TrD $_{\frac{1}{2}}$
E	2	C $_{2y}$	0	C $_{2a}$	0	C $_{2e}$	0
C $_{2x}$	0	C $_{2z}$	0	C $_{2b}$	0	C $_{2f}$	0
C $_{4x}$	$\sqrt{2}$	C $_{4z}$	$\sqrt{2}$	C $_{2c}$	0	C $_{3g}$	1
C $_{4x}^{-1}$	$\sqrt{2}$	C $_{4z}^{-1}$	$\sqrt{2}$	C $_{2d}$	0	C $_{3g}^{-1}$	1

Table A.3.

Character table for the point group  $C_1$

		E	time rev.
$\Gamma_S^{\alpha}$	$\Gamma^1$	1	a

$$G_o^M(\underline{Q}) = C_1 \text{ for } \underline{M} // [111], \underline{Q} = (1,0,0), (0,1,1), (0,1,\bar{1});$$

$$\underline{M} // [001], \underline{Q} = (0,1,1).$$

Table A.4.

Character table for the point group  $C_2$

		E	I	time rev.
$\Gamma_S^{\alpha}$	$\Gamma^1$	1	1	a
	$\Gamma^2$	1	-1	a

$$G_o^M(\underline{q}) = C_1 \text{ for } \underline{M} // [111], \underline{q} = (1,0,0).$$

Table A.5.

Character table for the point groups  $C_8$  and  $C_2$

	BSW		$R_1$	$R_2$	time rev.
$\Gamma_S^\alpha$	+	$\Gamma^1$	1	1	a
	-	$\Gamma^2$	1	-1	a
$\Gamma_D^\beta$		$\Gamma^3$	1	i	b
		$\Gamma^4$	1	-i	b
	$\underline{M}$	$\underline{Q}$	$R_1$	$R_2$	
$G_o^M(Q) = C_8 :$	$[001]$	(1,1,0), (1,0,0)	E	$IC_{2z}$	
	$[110]$	(0,0,1), ( $\frac{1}{2}, \bar{1}, 0$ ) (0,0,2), (2,2,0)	E	$IC_{2a}$	
	$[01\bar{1}]$	( $\eta, \zeta, \zeta$ )	E	$IC_{2e}$	
$G_o^{+M}(Q) = C_8 :$	$[001]$	(0,1,1)	E	$IC_{2x}$	
	$[111]$	(1,0,0), (0,1,1)	E	$IC_{2e}$	
$G_o^{+M}(Q) = C_2 :$	$[111]$	(0,1, $\bar{1}$ )	E	$C_{2e}$	

Table A.6.

Character table for the point group  $C_{2h}$

		$R_1$	$R_2$	$R_3$	$R_4$	time rev.
$\Gamma_S^\alpha$	$\Gamma^1$	1	1	1	1	a
	$\Gamma^2$	1	1	-1	-1	a
	$\Gamma^3$	1	-1	-1	1	a
	$\Gamma^4$	1	-1	1	-1	a
	$\underline{M}$	$\underline{q}$	$R_1$	$R_2$	$R_3$	$R_4$
$G_o^M(q) = C_{2h} :$	$[001]$	(1,0,0)	E	$C_{2z}$	I	$IC_{2z}$
	$[110]$	(0,0,1), (0,0,0)	E	$C_{2a}$	I	$IC_{2a}$
$G_o^{+M}(q) = C_{2h} :$	$[111]$	(1,0,0)	E	$C_{2e}$	I	$IC_{2e}$

Table A.7.

Character table for the point group  $C_{2v}$

BSW		$R_1$	$R_2$	$R_3$	$R_4$	time rev.
$\Gamma_S^{\alpha}$	$\Sigma_1 \Gamma^1$	1	1	1	1	a
	$\Sigma_2 \Gamma^2$	1	1	-1	-1	a
	$\Sigma_3 \Gamma^3$	1	-1	-1	1	a
	$\Sigma_4 \Gamma^4$	1	-1	1	-1	a
$\Gamma_D^{\beta}$	$\Sigma_5 \Gamma^5$	2	0	0	0	c

$G_o^{+M}(\underline{Q}) = C_{2v}$	$\underline{M}$	$\underline{Q}$	$R_1$	$R_2$	$R_3$	$R_4$
	$[001]$	$(1,0,0)$	E	$C_{2x}$	$IC_{2y}$	$IC_{2z}$
	$[001]$	$(1,1,0)$	E	$C_{2a}$	$IC_{2z}$	$IC_{2b}$
	$[110]$	$(0,0,1), (0,0,2)$	E	$C_{2z}$	$IC_{2a}$	$IC_{2b}$
	$[110]$	$(1, \bar{1}, 0), (\bar{2}, 2, 0)$	E	$C_{2b}$	$IC_{2z}$	$IC_{2a}$
$G_o(\underline{q}) = C_{2v}$ for $\underline{q} = (0, \zeta, \zeta)$			E	$C_{2f}$	$IC_{2x}$	$IC_{2e}$

Table A.8.

Character table for the point group  $D_{2h}$

		$R_1$	$R_2$	$R_3$	$R_4$	$R_5$	$R_6$	$R_7$	$R_8$	time rev.
$\Gamma_S^{\alpha}$	$\Gamma^1$	1	1	1	1	1	1	1	1	a
	$\Gamma^2$	1	-1	1	-1	1	-1	1	-1	a
	$\Gamma^3$	1	-1	-1	1	1	-1	-1	1	a
	$\Gamma^4$	1	1	-1	-1	1	1	-1	-1	a
	$\Gamma^5$	1	1	1	1	-1	-1	-1	-1	a
	$\Gamma^6$	1	-1	1	-1	-1	1	-1	1	a
	$\Gamma^7$	1	-1	-1	1	-1	1	1	-1	a
	$\Gamma^8$	1	1	-1	-1	-1	-1	1	1	a

$G_o^{+M}(\underline{q}) = D_{2h}$	$\underline{M}$	$\underline{q}$	$R_1$	$R_2$	$R_3$	$R_4$	$R_5$	$R_6$	$R_7$	$R_8$
	$[001]$	$(1,0,0)$	E	$C_{2x}$	$C_{2y}$	$C_{2z}$	I	$IC_{2x}$	$IC_{2y}$	$IC_{2z}$
	$[110]$	$(0,0,1), (0,0,2)$	E	$C_{2z}$	$C_{2a}$	$C_{2b}$	I	$IC_{2z}$	$IC_{2a}$	$IC_{2b}$

Table A.9.

Character table for the point group  $C_4$

		$R_1$	$R_2$	$R_3$	$R_4$	time rev.
$\Gamma_S^{\alpha}$	$\Gamma^1$	1	1	1	1	a
	$\Gamma^2$	1	-1	1	-1	a
	$\Gamma^3$	1	i	-1	-i	b
	$\Gamma^4$	1	-i	-1	i	b

$$G_o^M(\underline{Q}) = C_4 \text{ for } \underline{M} // [001], \underline{Q} = (0,0,1): R_1 = E; R_2 = C_{4z}; R_3 = C_{2z};$$

$$R_4 = C_{4z}^{-1}.$$

Table A.10.

Character table for the point group  $C_{4h}$

		$R_1$	$R_2$	$R_3$	$R_4$	$R_5$	$R_6$	$R_7$	$R_8$	time rev.
$\Gamma_S^{\alpha}$	$\Gamma^1$	1	1	1	1	1	1	1	1	a
	$\Gamma^2$	1	-1	1	-1	1	-1	1	-1	a
	$\Gamma^3$	1	i	-1	-i	1	i	-1	-i	b
	$\Gamma^4$	1	-i	-1	i	1	-i	-1	i	b
	$\Gamma^5$	1	1	1	1	-1	-1	-1	-1	a
	$\Gamma^6$	1	-1	1	-1	-1	1	-1	1	a
	$\Gamma^7$	1	i	-1	-i	-1	-i	1	i	b
	$\Gamma^8$	1	-i	-1	i	-1	i	1	-i	b

$$G_o^M(\underline{q}) = C_{4h} \text{ for } \underline{M} // [001], \underline{q} = (0,0,1): R_1 = E; R_2 = C_{4z}; R_3 = C_{2z};$$

$$R_4 = C_{4z}^{-1}; R_5 = I; R_6 = IC_{4z};$$

$$R_7 = IC_{2z}; R_8 = IC_{4z}^{-1}.$$

Table A.11.

Character table for the point group  $C_{4v}$

BSW <sup>*</sup> )			$R_1$	$R_2$	$R_3$	$R_4$	$R_5$	time rev.
$\Gamma_S^\alpha$	$\Delta_1$	$\Gamma^1$	1	1	1	1	1	a
	$\Delta_2$	$\Gamma^2$	1	1	-1	1	-1	a
	$\Delta_1'$	$\Gamma^3$	1	1	1	-1	-1	a
	$\Delta_2'$	$\Gamma^4$	1	1	-1	-1	1	a
	$\Delta_5$	$\Gamma^5$	2	-2	0	0	0	a
$\Gamma_D^\beta$	$\Delta_6$	$\Gamma^6$	2	0	$\sqrt{2}$	0	0	c
	$\Delta_7$	$\Gamma^7$	2	0	$-\sqrt{2}$	0	0	c

\*.) The notation  $\Delta_6$  and  $\Delta_7$  for  $\Gamma_D^\beta$  is due to Elliott [99].

$$G_o^{-M}(\underline{Q}) = C_{4v} \text{ for } \underline{M} // [001], \underline{Q} = (0,0,1) \quad \begin{matrix} R_1 & R_2 & R_3 & R_4 & R_5 \\ E & C_{2z} & C_{4z}, C_{4z}^{-1} & IC_{2x}, IC_{2y} & IC_{2a}, IC_{2b} \end{matrix}$$

$$G_o(\underline{q}) = C_{4v} \text{ for } \underline{q} = (\zeta, 0, 0) \quad \begin{matrix} E & C_{2x} & C_{4x}, C_{4x}^{-1} & IC_{2y}, IC_{2z} & IC_{2e}, IC_{2f} \end{matrix}$$

Two-dimensional representation  $\Delta_5$  for  $\underline{q} = (\zeta, 0, 0)$ :

$$\begin{matrix} E & C_{2x} & C_{4x} & C_{4x}^{-1} & IC_{2y} & IC_{2z} & IC_{2f} & IC_{2e} \\ \begin{pmatrix} 1 & 0 \\ 0 & 1 \end{pmatrix} & \begin{pmatrix} -1 & 0 \\ 0 & -1 \end{pmatrix} & \begin{pmatrix} 0 & 1 \\ -1 & 0 \end{pmatrix} & \begin{pmatrix} 0 & -1 \\ 1 & 0 \end{pmatrix} & \begin{pmatrix} -1 & 0 \\ 0 & 1 \end{pmatrix} & \begin{pmatrix} 1 & 0 \\ 0 & -1 \end{pmatrix} & \begin{pmatrix} 0 & -1 \\ -1 & 0 \end{pmatrix} & \begin{pmatrix} 0 & 1 \\ 1 & 0 \end{pmatrix} \end{matrix}$$

Table A.12.

Character table for the point group  $D_{4h}$

BSW		$R_1$	$R_2$	$R_3$	$R_4$	$R_5$	$R_6$	$R_7$	$R_8$	$R_9$	$R_{10}$	time rev.	
$\Gamma_S^\alpha$	$X_1$	$\Gamma^1$	1	1	1	1	1	1	1	1	1	a	
	$X_2$	$\Gamma^2$	1	1	1	-1	-1	1	1	-1	-1	a	
	$X_3$	$\Gamma^3$	1	-1	1	-1	1	1	-1	1	-1	a	
	$X_4$	$\Gamma^4$	1	-1	1	1	-1	1	-1	1	-1	a	
	$X_5$	$\Gamma^5$	2	0	-2	0	0	2	0	-2	0	0	a
	$X'_1$	$\Gamma^6$	1	1	1	1	1	-1	-1	-1	-1	-1	a
	$X'_2$	$\Gamma^7$	1	1	1	-1	-1	-1	-1	-1	1	1	a
	$X'_3$	$\Gamma^8$	1	-1	1	-1	1	-1	1	-1	1	-1	a
	$X'_4$	$\Gamma^9$	1	-1	1	1	-1	-1	1	-1	-1	1	a
	$X'_5$	$\Gamma^{10}$	2	0	-2	0	0	-2	0	2	0	0	a

$$G_o^{\pm M}(\underline{q}) = D_{4h} \text{ for } \underline{M} // [001], \underline{q} (0,0,1):$$

$$R_1 = E; R_2 = C_{2x}, C_{2y}; R_3 = C_{2z}; R_4 = C_{4z}, C_{4z}^{-1}; R_5 = C_{2a}, C_{2b};$$

$$R_6 = I; R_7 = IC_{2x}, IC_{2y}; R_8 = IC_{2z}; R_9 = IC_{4z}, IC_{4z}^{-1}; R_{10} = IC_{2a}, IC_{2b}.$$

Two-dimensional representation  $\Gamma^{10}$

E	$C_{2x}$	$C_{2y}$	$C_{2z}$	$C_{4z}$	$C_{4z}^{-1}$	$C_{2a}$	$C_{2b}$
$\begin{pmatrix} 1 & 0 \\ 0 & 1 \end{pmatrix}$	$\begin{pmatrix} 1 & 0 \\ 0 & -1 \end{pmatrix}$	$\begin{pmatrix} -1 & 0 \\ 0 & 1 \end{pmatrix}$	$\begin{pmatrix} -1 & 0 \\ 0 & -1 \end{pmatrix}$	$\begin{pmatrix} 0 & 1 \\ -1 & 0 \end{pmatrix}$	$\begin{pmatrix} 0 & -1 \\ 1 & 0 \end{pmatrix}$	$\begin{pmatrix} 0 & 1 \\ 1 & 0 \end{pmatrix}$	$\begin{pmatrix} 0 & -1 \\ -1 & 0 \end{pmatrix}$

$$\Gamma^{10}(\text{IR}) = -\Gamma^{10}(\text{R})$$



Table A.13.

Character table for the point group  $C_{3v}$

BSW <sup>*)</sup>		$R_1$	$R_2$	$R_3$	time rev.
$\Gamma_S^\alpha$	$\Lambda_1 \Gamma^1$	1	1	1	a
	$\Lambda_2 \Gamma^2$	1	1	-1	a
	$\Lambda_3 \Gamma^3$	2	-1	0	a
$\Gamma_D^\beta$	$\Lambda_4 \Gamma^4$	1	-1	i	b
	$\Lambda_5 \Gamma^5$	1	-1	-i	b
	$\Lambda_6 \Gamma^6$	2	1	0	c

\*) The notation  $\Lambda_4, \Lambda_5$  and  $\Lambda_6$  for  $\Gamma_D^\beta$  is due to Parmenter [100]

$G_o(\underline{q}) = C_{3v}$  for  $\underline{q} = (\zeta, \zeta, \zeta) : R_1 = E ; R_2 = C_{3\delta}, C_{3\delta}^{-1} ; R_3 = IC_{2b}, IC_{2d}, IC_{2e}$ .

Two-dimensional representation  $\Lambda_3$  for  $\underline{q} = (\zeta, \zeta, \zeta)$ .

E	$C_{3\delta}$	$C_{3\delta}^{-1}$	$IC_{2b}$	$IC_{2d}$	$IC_{2e}$
$\begin{pmatrix} 1 & 0 \\ 0 & 1 \end{pmatrix}$	$\begin{pmatrix} -\frac{1}{2} & -\frac{1}{2}\sqrt{3} \\ \frac{1}{2}\sqrt{3} & -\frac{1}{2} \end{pmatrix}$	$\begin{pmatrix} -\frac{1}{2} & \frac{1}{2}\sqrt{3} \\ -\frac{1}{2}\sqrt{3} & -\frac{1}{2} \end{pmatrix}$	$\begin{pmatrix} -1 & 0 \\ 0 & 1 \end{pmatrix}$	$\begin{pmatrix} \frac{1}{2} & \frac{1}{2}\sqrt{3} \\ \frac{1}{2}\sqrt{3} & -\frac{1}{2} \end{pmatrix}$	$\begin{pmatrix} \frac{1}{2} & -\frac{1}{2}\sqrt{3} \\ -\frac{1}{2}\sqrt{3} & -\frac{1}{2} \end{pmatrix}$

Table A.14.

Character table for the point group  $D_{3d}$

		$R_1$	$R_2$	$R_3$	$R_4$	$R_5$	$R_6$	time rev.
$\Gamma_S^\alpha$	$\Gamma^1$	1	1	1	1	1	1	a
	$\Gamma^2$	1	1	-1	1	1	-1	a
	$\Gamma^3$	2	-1	0	2	-1	0	a
	$\Gamma^4$	1	1	1	-1	-1	-1	a
	$\Gamma^5$	1	1	-1	-1	-1	1	a
	$\Gamma^6$	2	-1	0	-2	1	0	a

$$G_o^{+M} = D_{3d} \text{ for } \underline{M} // [111]: R_1 = E; R_2 = C_{3\delta}, C_{3\delta}^{-1}; R_3 = C_{2b}, C_{2d}, C_{2e};$$

$$R_4 = I; R_5 = IC_{3\delta}, IC_{3\delta}^{-1}; R_6 = IC_{2b}, IC_{2d}, IC_{2e}.$$

Two-dimensional representation  $\Gamma^6$

$$\begin{matrix} E & C_{3\delta} & C_{3\delta}^{-1} & C_{2b} & C_{2d} & C_{2e} \\ \begin{pmatrix} 1 & 0 \\ 0 & 1 \end{pmatrix} & \begin{pmatrix} -\frac{1}{2} & -\frac{1}{2}\sqrt{3} \\ \frac{1}{2}\sqrt{3} & -\frac{1}{2} \end{pmatrix} & \begin{pmatrix} -\frac{1}{2} & \frac{1}{2}\sqrt{3} \\ -\frac{1}{2}\sqrt{3} & -\frac{1}{2} \end{pmatrix} & \begin{pmatrix} -1 & 0 \\ 0 & 1 \end{pmatrix} & \begin{pmatrix} \frac{1}{2} & \frac{1}{2}\sqrt{3} \\ \frac{1}{2}\sqrt{3} & -\frac{1}{2} \end{pmatrix} & \begin{pmatrix} \frac{1}{2} & -\frac{1}{2}\sqrt{3} \\ -\frac{1}{2}\sqrt{3} & -\frac{1}{2} \end{pmatrix} \end{matrix}$$

$$\Gamma^6(\text{IR}) = -\Gamma^6(R)$$

Table A.15.

Character table for the point group  $O_h$

BSW	$R_1$	$R_2$	$R_3$	$R_4$	$R_5$	$R_6$	$R_7$	$R_8$	$R_9$	$R_{10}$	time rev.
$\Gamma_1 \Gamma^1$	1	1	1	1	1	1	1	1	1	1	a
$\Gamma_2 \Gamma^2$	1	1	1	-1	-1	1	1	1	-1	-1	a
$\Gamma_{12} \Gamma^3$	2	-1	2	0	0	2	-1	2	0	0	a
$\Gamma_{15} \Gamma^4$	3	0	-1	1	-1	3	0	-1	1	-1	a
$\Gamma_{25} \Gamma^5$	3	0	-1	-1	1	3	0	-1	-1	1	a
$\Gamma_1' \Gamma^6$	1	1	1	1	1	-1	-1	-1	-1	-1	a
$\Gamma_2' \Gamma^7$	1	1	1	-1	-1	-1	-1	-1	1	1	a
$\Gamma_{12}' \Gamma^8$	2	-1	2	0	0	-2	1	-2	0	0	a
$\Gamma_{15}' \Gamma^9$	3	0	-1	1	-1	-3	0	1	-1	1	a
$\Gamma_{25}' \Gamma^{10}$	3	0	-1	-1	1	-3	0	1	1	-1	a

$$G_o = O_h: R_1 = E; R_2 = C_{3\alpha}, C_{3\beta}, C_{3\gamma}, C_{3\delta}, C_{3\alpha}^{-1}, C_{3\beta}^{-1}, C_{3\gamma}^{-1}, C_{3\delta}^{-1};$$

$$R_3 = C_{2x}, C_{2y}, C_{2z}; R_4 = C_{4x}, C_{4y}, C_{4z}, C_{4x}^{-1}, C_{4y}^{-1}, C_{4z}^{-1};$$

$$R_5 = C_{2a}, C_{2b}, C_{2c}, C_{2d}, C_{2e}, C_{2f};$$

the elements in  $R_{5+j}$  are the improper rotation IR corresponding to the proper rotations R in  $R_j$ .

APPENDIX B

Analysis of neutron scattering data by application of selection rules

In this appendix a group-theoretical analysis is given of the time-of-flight results summarized in tables 6.3, 6.4 and 6.5. We recall that scattering by the mixed modes was observed at  $\underline{Q} = (0,0,1)$ ,  $(1,0,0)$  and  $(\bar{1},0,0)$  in a  $[001]$  domain, and at  $\underline{Q} = (0,0,1)$  in a  $[110]$  domain. The mixed mode was not observed at  $\underline{Q} = (1,1,0)$  and  $(0,1,1)$  in a  $[001]$  domain, at  $\underline{Q} = (1,\bar{1},0)$  in a  $[110]$  domain, and at  $\underline{Q} = (0,0,1)$ ,  $(0,1,1)$  and  $(0,1,\bar{1})$  in a  $[111]$  domain. The absence of scattering for a particular scattering vector  $\underline{Q}$  is interpreted as a consequence of the selection rule for neutron scattering, which is based on the point group of  $\underline{Q}$  (cf. section 3.4.3). Below we shall treat the two cases (a) and (b) mentioned in section 6.6.

Case (a): Neutron scattering with or without spin flip on basis of the point groups  $G_o^M(\underline{Q})$ . In table B.1 the subgroups  $G_o^M(\underline{Q})$  for the investigated points  $\underline{Q}$  are listed, while the symmetry operations and character tables belonging to these point groups are given in appendix A.

By inspection of the character tables one may easily identify the irreducible representations for excitations with spin 0 and  $\pm 1$ , which can give rise to neutron scattering without and with spin flip, respectively. Excitations with spin 0 transform as  $\Gamma^1$  in each group, whereas excitations with spin  $\pm 1$  are characterized by  $\chi(IC_{2z}) = \chi(C_{2z}) = -1$  and  $\chi(IC_{4z}) = \chi(C_{4z}) = \pm i$  in the  $[001]$  domain and by  $\chi(IC_{2a}) = \chi(C_{2a}) = -1$  in the  $[110]$  domain. The representations of observable excitations are listed in the left-hand part of table B.2.

One may conclude from table B.1 that the selection rules based on the magnetic point groups do not give a satisfactory explanation for all experimental results:

1. In several cases the point group is  $C_1$  with only one single-valued representation  $\Gamma^1$ . Hence neutron scattering by the mixed mode is not forbidden in the points  $\underline{Q}_1$ ,  $\underline{Q}_2$  and  $\underline{Q}_3$  for the  $[111]$  domain and in  $\underline{Q}_2$  for the  $[001]$  domain.
2. For the  $[110]$  domain the subduction of an arbitrary representation of  $C_{2h}$  onto the identical point groups of  $\underline{Q}_1$  and  $\underline{Q}_2$  yields the same representation of  $C_s$ , and the cross sections in these points should therefore be of comparable magnitude.

Both conclusions are valid irrespective of the spin states of the neutron before and after scattering, and are in disagreement with the experimental results.

Table B.1

Magnetic and pseudo-magnetic point groups in single domains

$\underline{M}$	$\underline{q}, \underline{Q}_i$	$G_o^M$	table	$G_o^{\pm M}$	table
[001]	$\underline{q} = (1,0,0)$	$C_{2h}$	A.6	$D_{2h}$	A.8
	$\underline{Q}_1 = (1,0,0)$	$C_s$	A.5	$C_{2v}$	A.7
	$\underline{Q}_2 = (0,1,1)$	$C_1$	A.3	$C_s$	A.5
[001]	$\underline{q} = (0,0,1)$	$C_{4h}$	A.10	$D_{4h}$	A.12
	$\underline{Q}_1 = (0,0,1)$	$C_4$	A.9	$C_{4v}$	A.11
	$\underline{Q}_2 = (1,1,0)$	$C_s$	A.5	$C_{2v}$	A.7
[111]	$\underline{q} = (1,0,0)$	$C_i$	A.4	$C_{2h}$	A.6
	$\underline{Q}_1 = (1,0,0)$	$C_1$	A.3	$C_s$	A.5
	$\underline{Q}_2 = (0,1,1)$	$C_1$	A.3	$C_s$	A.5
	$\underline{Q}_3 = (0,1,\bar{1})$	$C_1$	A.3	$C_2$	A.5
[110]	$\underline{q} = (0,0,1)$	$C_{2h}$	A.6	$D_{2h}$	A.8
	$\underline{Q}_1 = (0,0,1)$	$C_s$	A.5	$C_{2v}$	A.7
	$\underline{Q}_2 = (1,\bar{1},0)$	$C_s$	A.5	$C_{2v}$	A.7

Table B.2

Excitations observable by means of neutron scattering with scattering vector  $\underline{Q}$ .

$G_o^M(\underline{Q})$	$C_4$	$C_s$	$C_1$	$C_{4v}$	$C_{2v}$	$C_s$	$C_2$	$G_o^{\pm M}(\underline{Q})$
$\Delta s = 0$	$\Gamma^1$	$\Gamma^1$	$\Gamma^1$	$\Gamma^1, \Gamma^3$	$\Gamma^1, \Gamma^2$	$\Gamma^1$	$\Gamma^1$	$\Delta s = 0$
$\Delta s = \pm 1$	$\Gamma^3, \Gamma^4$	$\Gamma^2$	$\Gamma^1$					

On the other hand, one may select three possible representations for the mixed mode with  $\underline{q} = (0,0,1)$  in the  $[001]$  domain that are in agreement with the experimental results. To establish the selection rules one has to reduce the eight irreducible representations of  $G_o^M(\underline{q}) = C_{4h}$  onto the subgroups  $G_o^M(Q_1) = C_4$  and  $G_o^M(Q_2) = C_s$ . This subduction is performed by means of (2.5) and (2.6), where the summation in (2.6) is restricted to the elements of the subgroups and the characters are taken from the appropriate tables in appendix A. The results are collected in table B.3. Since the mixed mode is observed in  $Q_1 = (0,0,1)$  it must transform as  $\Gamma^1$  of  $C_4$  if its spin is 0 or as  $\Gamma^3(\Gamma^4)$  if its spin is  $\pm 1$ . The absence of scattering in  $Q_2 = (1,1,0)$  indicates that the mode transforms as  $\Gamma^2$  of  $C_s$  if its spin is 0 or as  $\Gamma^1$  if its spin is  $\pm 1$ . From table B.3 it is found that the excitations transforming as  $\Gamma^5$ ,  $\Gamma^7$  and  $\Gamma^8$  of  $C_{4h}$  satisfy these requirements.

Table B.3.

Subduction table for excitations with  $\underline{q} = (0,0,1)$  in a  $[001]$  single domain. Possible representations for the mixed mode have been indicated.

$\underline{q} \cdot Q_i$	$G_o^M$	table	$\Gamma_S^\alpha$							
$\underline{q} = (0,0,1)$	$C_{4h}$	A.10	$\Gamma^1$	$\Gamma^2$	$\Gamma^3$	$\Gamma^4$	$\Gamma^5$	$\Gamma^6$	$\Gamma^7$	$\Gamma^8$
$Q_1 = (0,0,1)$	$C_4$	A.9	$\Gamma^1$	$\Gamma^2$	$\Gamma^3$	$\Gamma^4$	$\Gamma^1$	$\Gamma^2$	$\Gamma^3$	$\Gamma^4$
$Q_2 = (1,1,0)$	$C_s$	A.5	$\Gamma^1$	$\Gamma^1$	$\Gamma^2$	$\Gamma^2$	$\Gamma^2$	$\Gamma^2$	$\Gamma^1$	$\Gamma^1$

Case (b): Neutron scattering without spin flip on basis of the pseudo-magnetic point groups  $G_o^{+M}(Q)$ . As mentioned in section 6.6, excitations transforming as irreducible representations of a pseudo-magnetic point group do not have a magnetic moment, and only scattering without spin flip can occur. Furthermore, there is no distinction between the two spin states of the neutron: the spin states  $|+\rangle$  and  $|-\rangle$  transform either as a two-dimensional representation ( $\Gamma^5$  of  $C_{2v}$ ,  $\Gamma^6$  of  $C_{4v}$ ) or as a pair of complex conjugate, one-dimensional representations ( $\Gamma^3$  and  $\Gamma^4$  of  $C_s$  or  $C_2$ ). In the latter case  $\Gamma^3$  and  $\Gamma^4$  represent two different linear combinations of both spin states and neutron scattering without

spin change occurs if the initial and final state of the neutron transform as the same representation. If the neutron states transform as a two-dimensional representation, one may distinguish between scattering processes with and without spin flip by applying the selection rule considered in section 3.4.3.

The selection rules are applied to the point groups  $G_o^{+M}(Q)$  listed in table B.1. For each of these groups the observable excitations with spin 0 are given in the right-hand part of table B.2, and the subduction of the representations of  $G_o^{+M}(q)$  onto the subgroups  $G_o^{+M}(Q)$  in table B.4. It should be emphasized that the pseudo-magnetic point groups for the scattering vectors  $Q_1$  and  $Q_2$  in the  $[110]$  domain do not consist of the same elements; hence the subduction onto these two groups yields in general different irreducible representations, which means that the scattering cross sections in  $Q_1$  and  $Q_2$  are different. On the other hand the point groups  $G_o^{+M}(Q_1)$  and  $G_o^{+M}(Q_2)$  for the  $[111]$  domain are identical and the cross sections in  $Q_1$  and  $Q_2$  are therefore of comparable magnitude in this domain.

A selection of possible irreducible representations for the mixed mode can be made by means of the subduction table B.4, which leads to the results given in table 6.7. When the experimental results in  $Q_1 = (0,0,1)$  and  $Q_2 = (1,1,0)$  in the  $[001]$  domain are treated on basis of pseudo-magnetic point groups, one finds that the mixed mode with  $q = (0,0,1)$  transforms either as  $\Gamma^4$  or as  $\Gamma^9$  of  $G_o^{+M}(q) = D_{4h}$ .

Table B.4

Subduction table for excitations in single domains.

Possible representations for the mixed mode have been indicated.

$\underline{M}$	$\underline{q}, \underline{Q}_i$	$G_o^{\pm M}$	table	$\Gamma_S^\alpha$
[001]	$\underline{q} = (0,0,1)$	$D_{4h}$	A.12	$\Gamma^1 \Gamma^2 \Gamma^3$ $\boxed{\Gamma^4}$ $\Gamma^5$ $\Gamma^6 \Gamma^7 \Gamma^8$ $\boxed{\Gamma^9}$ $\Gamma^{10}$
	$\underline{Q}_1 = (0,0,1)$	$C_{4v}$	A.11	$\Gamma^1 \Gamma^2 \Gamma^4$ $\boxed{\Gamma^3}$ $\Gamma^5$ $\Gamma^3 \Gamma^4 \Gamma^2$ $\boxed{\Gamma^1}$ $\Gamma^5$
	$\underline{Q}_2 = (1,1,0)$	$C_{2v}$	A.7	$\Gamma^1 \Gamma^4 \Gamma^1$ $\boxed{\Gamma^4}$ $\Gamma^2 \oplus \Gamma^3$ $\Gamma^2 \Gamma^3 \Gamma^2$ $\boxed{\Gamma^3}$ $\Gamma^1 \oplus \Gamma^4$
[001]	$\underline{q} = (1,0,0)$	$D_{2h}$	A.8	$\Gamma^1 \Gamma^2 \Gamma^3 \Gamma^4$ $\boxed{\Gamma^5}$ $\Gamma^6 \Gamma^7$ $\boxed{\Gamma^8}$
	$\underline{Q}_1 = (1,0,0)$	$C_{2v}$	A.7	$\Gamma^1 \Gamma^4 \Gamma^3 \Gamma^2$ $\boxed{\Gamma^2}$ $\Gamma^3 \Gamma^4$ $\boxed{\Gamma^1}$
	$\underline{Q}_2 = (0,1,1)$	$C_s$	A.5	$\Gamma^1 \Gamma^2 \Gamma^2 \Gamma^1$ $\boxed{\Gamma^2}$ $\Gamma^1 \Gamma^1$ $\boxed{\Gamma^2}$
[110]	$\underline{q} = (0,0,1)$	$D_{2h}$	A.8	$\Gamma^1 \Gamma^2 \Gamma^3$ $\boxed{\Gamma^4}$ $\Gamma^5 \Gamma^6 \Gamma^7$ $\boxed{\Gamma^8}$
	$\underline{Q}_1 = (0,0,1)$	$C_{2v}$	A.7	$\Gamma^1 \Gamma^4 \Gamma^3$ $\boxed{\Gamma^2}$ $\Gamma^2 \Gamma^3 \Gamma^4$ $\boxed{\Gamma^1}$
	$\underline{Q}_2 = (1, \bar{1}, 0)$	$C_{2v}$	A.7	$\Gamma^1 \Gamma^3 \Gamma^2$ $\boxed{\Gamma^4}$ $\Gamma^2 \Gamma^4 \Gamma^1$ $\boxed{\Gamma^3}$
[111]	$\underline{q} = (1,0,0)$	$C_{2h}$	A.6	$\Gamma^1 \Gamma^2 \Gamma^3$ $\boxed{\Gamma^4}$
	$\underline{Q}_1 = (1,0,0)$	$C_s$	A.5	$\Gamma^1 \Gamma^2 \Gamma^1$ $\boxed{\Gamma^2}$
	$\underline{Q}_2 = (0,1,1)$	$C_s$	A.5	$\Gamma^1 \Gamma^2 \Gamma^1$ $\boxed{\Gamma^2}$
	$\underline{Q}_3 = (0,1, \bar{1})$	$C_2$	A.5	$\Gamma^1 \Gamma^1 \Gamma^2$ $\boxed{\Gamma^2}$

Neutron-phonon scattering in single domains

To establish the selection rules for neutron-phonon scattering in single domains the representations of the phonons should be subduced onto the magnetic or pseudo-magnetic point groups. For phonons with  $\underline{q}$  along the  $[001]$  direction the results of this subduction are collected in table B.5.

Table B.5

*Subduction table for  $\Delta_1$  and  $\Delta_5$  phonons in single domains*

$\underline{M}$	$\underline{q}$	$G_o^{\pm M}(\underline{q})$	$\Delta_1$	$\Delta_5$	$G_o^M(\underline{q})$	$\Delta_1$	$\Delta_5$
[001]	( $\zeta, 0, 0$ )	$C_{2v}$	$\Gamma^1$	$\Gamma^3 \oplus \Gamma^4$	$C_s$	$\Gamma^1$	$\Gamma^1 \oplus \Gamma^2$
[001]	( $0, 0, \zeta$ )	$C_{4v}$	$\Gamma^1$	$\Gamma^5$	$C_4$	$\Gamma^1$	$\Gamma^3 \oplus \Gamma^4$
[111]	( $\zeta, 0, 0$ )	$C_s$	$\Gamma^1$	$\Gamma^1 \oplus \Gamma^2$	$C_1$	$\Gamma^1$	$2\Gamma^1$
[110]	( $0, 0, \zeta$ )	$C_{2v}$	$\Gamma^1$	$\Gamma^3 \oplus \Gamma^4$	$C_s$	$\Gamma^1$	$\Gamma^1 \oplus \Gamma^2$



APPENDIX C

Symmetry properties of polar modes

In this appendix the eigenvectors are tabulated for the polar modes that originate from the triply degenerate  $\Gamma^9$  state in the cubic crystal. The eigenvectors  $\underline{\psi}$  of the electron-hole excitations are listed in table C.1 for three magnetization directions. Each mode may be characterized by a specific polarization direction, indicated in the last row of the table. The probability to find the electron at site  $\underline{z}$  is given by  $\psi_{\underline{z}}^* \psi_{\underline{z}}$ , where the positions of the sites are shown in figure 7.1.

Table C.1.

Eigenvectors  $\underline{\psi}$  of polar modes in single domains<sup>\*)</sup>

z	$\underline{M} // [001]$			$\underline{M} // [110]$			$\underline{M} // [111]$		
	$\underline{\psi}(\Gamma^9)$	$\underline{\psi}_1(\Gamma^{10})$	$\underline{\psi}_2(\Gamma^{10})$	$\underline{\psi}(\Gamma^6)$	$\underline{\psi}(\Gamma^7)$	$\underline{\psi}(\Gamma^8)$	$\underline{\psi}(\Gamma^5)$	$\sqrt{3} \times \underline{\psi}_1(\Gamma^6)$	$\underline{\psi}_2(\Gamma^6)$
1	0	0	0	0	0	0	0	0	0
2	0	b	b	b	0	0	f	-2e	0
3	0	-b	b	0	d	0	0	0	d
4	a	0	c	c	e	a	f	e	e
5	-a	0	c	c	e	-a	0	-3d/2	1/2 d
6	a	-c	0	-c	e	a	0	3d/2	1/2 d
7	a	c	0	c	-e	a	f	e	-e
8	0	-b	-b	-b	0	0	-f	2e	0
9	0	b	-b	0	-d	0	0	0	-d
10	-a	0	-c	-c	-e	-a	-f	-e	-e
11	a	0	-c	-c	-e	a	0	3d/2	-1/2 d
12	-a	c	0	c	-e	-a	0	-3d/2	-1/2 d
13	-a	-c	0	-c	e	-a	-f	-e	e
pol. dir.	[001]	[100]	[010]	[110]	[110]	[001]	[111]	[112]	[110]

\*)  $a = 8^{-1/2}$ ;  $f = 6^{-1/2}$ ; the values of b, c, d, and e are defined for each domain separately, and are subject to the normalization condition

$$\sum_{z=1}^{13} \psi_z^* \psi_z = 1.$$

A polar electron-hole mode induces vibrations of the lattice sites, which are described by the displacement vectors  $\underline{u}_l$ . For each of the polar modes in table C.1 the symmetry properties of the vectors  $\underline{u}_l$  for the 13 sites in figure 7.1 are summarized in the tables C.2, C.3 and C.4. When some components  $u_l^x$ ,  $u_l^y$ , or  $u_l^z$  in the tables are equal the corresponding oscillations of the sites are in phase and have equal amplitudes. Similarly, components with the same absolute value but opposite signs correspond with oscillations in opposite phase with equal amplitudes.

Table C.2.

Displacement vectors  $\underline{u}$  for mixed polar modes  
in a [001] domain;  $G_O^{\pm M} = D_{4h}^*$

l	$\underline{u}(\Gamma^9)$			$\underline{u}_1(\Gamma^{10})$			$\underline{u}_2(\Gamma^{10})$		
	$u_l^x$	$u_l^y$	$u_l^z$	$u_l^x$	$u_l^y$	$u_l^z$	$u_l^x$	$u_l^y$	$u_l^z$
1	0	0	b	a	0	0	0	a	0
2	0	0	c	b	e	0	e	b	0
3	0	0	c	b	-e	0	-e	b	0
4	0	-a	d	c	0	0	0	d	-f
5	0	a	d	c	0	0	0	d	f
6	a	0	d	d	0	f	0	c	0
7	-a	0	d	d	0	-f	0	c	0
8	0	0	c	b	e	0	e	b	0
9	0	0	c	b	-e	0	-e	b	0
10	0	-a	d	c	0	0	0	d	-f
11	0	a	d	c	0	0	0	d	f
12	a	0	d	d	0	f	0	c	0
13	-a	0	d	d	0	-f	0	c	0

\*) a, b, c, ... are defined for  $\Gamma^9$  and  $\Gamma^{10}$ , separately.

$\underline{u}_2(\Gamma^{10})$  is constructed by means of the projection

$$P_{21}(\Gamma^{10})\underline{u}_1(\Gamma^{10}) = \underline{u}_2(\Gamma^{10})$$

to obtain the proper phase relationship between  $\underline{u}_1$  and  $\underline{u}_2$ .

Table C.3.

Displacement vectors  $\underline{u}$  for mixed polar modes  
in a  $[110]$  domain;  $G_o^{+M} = D_{2h}$  \*)

$l$	$\underline{u}(\Gamma^6)$			$\underline{u}(\Gamma^7)$			$\underline{u}(\Gamma^8)$		
	$u_l^x$	$u_l^y$	$u_l^z$	$u_l^x$	$u_l^y$	$u_l^z$	$u_l^x$	$u_l^y$	$u_l^z$
1	a	a	0	a	-a	0	0	0	c
2	b	b	0	b	-b	0	0	0	d
3	c	c	0	c	-c	0	0	0	e
4	d	e	f	d	-e	f	a	-b	f
5	d	e	-f	d	-e	-f	-a	b	f
6	e	d	-f	e	-d	f	b	-a	f
7	e	d	f	e	-d	-f	-b	a	f
8	b	b	0	b	-b	0	0	0	d
9	c	c	0	c	-c	0	0	0	e
10	d	e	f	d	-e	f	a	-b	f
11	d	e	-f	d	-e	-f	-a	b	f
12	e	d	-f	e	-d	f	b	-a	f
13	e	d	f	e	-d	-f	-b	a	f

\*) a, b, c, ..... are defined for each representation separately.

Table C.4.

Displacement vectors  $\underline{u}$  for mixed polar modes  
in a  $[111]$  domain;  $G_o^{\pm M} = D_{3d}$  \*)

z	$\underline{u}(\Gamma^5)$			$\sqrt{3} \times \underline{u}_1(\Gamma^6)$			$\underline{u}_2(\Gamma^6)$		
	$u_z^x$	$u_z^y$	$u_z^z$	$u_z^x$	$u_z^y$	$u_z^z$	$u_z^x$	$u_z^y$	$u_z^z$
1	a	a	a	a	a	-2a	a	-a	0
2	b	b	d	c-h	c-h	-2e	b	-b	0
3	c	c	e	g-i	g-i	-2f	d	-d	0
4	d	b	b	e	b+h	-b-c	e	-c	h
5	e	c	c	f	d+i	-d-g	f	-g	i
6	c	e	c	d+i	f	-d-g	g	-f	-i
7	b	d	b	b+h	e	-b-c	c	-e	-h
8	b	b	d	c-h	c-h	-2e	b	-b	0
9	c	c	e	g-i	g-i	-2f	d	-d	0
10	d	b	b	e	b+h	-b-c	e	-c	h
11	e	c	c	f	d+i	-d-g	f	-g	i
12	c	e	c	d+i	f	-d-g	g	-f	-i
13	b	d	b	b+h	e	-b-c	c	-e	-h

\*) a, b, c, ..... are defined for  $\Gamma^5$  and  $\Gamma^6$ , separately.  
 $\underline{u}_1(\Gamma^6)$  is constructed by means of the projection

$$P_{12}(\Gamma^6)\underline{u}_2(\Gamma^6) = \underline{u}_1(\Gamma^6).$$

Structure factors for mixed polar modes

The neutron scattering by a mixed polar mode is related to the structure factor of the mode, which is defined in (7.4). In the following tables C.5, C.6 and C.7 the structure factors  $F(\underline{Q})$  are listed for those points  $\underline{Q}$  that are of interest for the present investigation. The parameters  $a, b, \dots$ , used for a specific mode, are identical to the parameters occurring in the displacement vector  $\underline{u}$  for the same mode. It should be emphasized that the parameters are defined for each representation, separately.

Table C.5.

Structure factors  $F(\underline{Q})$  for mixed polar modes  
in a  $[001]$  domain

$\underline{Q}$	$\Gamma^9$	$(\Gamma^{10})_1$	$(\Gamma^{10})_2$
(0,0,1)	$b+4c-8d$	0	0
(1,0,0)	0	$a-4b+4c-4d$	0
(0,1,0)	0	0	$a-4b+4c-4d$
(1,1,0)	0	$a+4b-4c-4d$	$a+4b-4c-4d$
(1, $\bar{1}$ ,0)	0	$a+4b-4c-4d$	$-a-4b+4c+4d$
(0,1,1)	$b-4c$	0	$a-4b-4c+4d$
( $\frac{1}{2}, \frac{1}{2}, \frac{1}{2}$ )	$\frac{1}{2}(b+8a)$	$\frac{1}{2}(a-4e+4f)$	$\frac{1}{2}(a-4e+4f)$
(0,0,2)	$b+4c+8d$	0	0

Table C.6.

Structure factors  $F(Q)$  for mixed polar modes  
in a  $[110]$  domain

$Q$	$\Gamma^6$	$\Gamma^7$	$\Gamma^8$
(0,0,1)	0	0	$c+2d+2e-8f$
(1,0,0)	$a-2b-2c+4d-4e$	$a-2b-2c+4d-4e$	0
(0,1,0)	$a-2b-2c+4d-4e$	$-a+2b+2c-4d+4e$	0
(1,1,0)	$2a+4b+4c-8d-8e$	0	0
( $\bar{1}$ ,1,0)	0	$-2(a+2b+2c-4d-4e)$	0
( $\frac{1}{2}, \frac{1}{2}, \frac{1}{2}$ )	0	$-a-2b+2c-4f$	$\frac{1}{2}c+d-e+4a+4b$
( $\bar{2}$ ,2,0)	0	$-4(a+2b+2c+4d+4e)$	0

Table C.7.

Structure factors  $F(Q)$  for mixed polar modes  
in a  $[111]$  domain<sup>\*</sup>

$Q$	$\Gamma^5$	$(\Gamma^6)_1$	$(\Gamma^6)_2$
(0,0,1)	$a-4b-4c+2d+2e$	$-2a+4b+4c+4d-4e-4f+4g$	0
(1,0,0)	$a-4b-4c+2d+2e$	$a-2b-2c-2d+2e+2f-2g$	$a-2b-2c-2d+2e+2f-2g$
(0,1,0)	$a-4b-4c+2d+2e$	$a-2b-2c-2d+2e+2f-2g$	$-a+2b+2c+2d-2e-2f+2g$
(1,1,0)	$2a-4d-4e$	$2a-4b+4c-4d-4e-4f+4g+-8h-8i$	0
(1, $\bar{1}$ ,0)	0	0	$2a+4b-4c+4d-4e-4f-4g$
( $\frac{1}{2}, \frac{1}{2}, \frac{1}{2}$ )	$(3a/2)-6b+6c-3d+3e$	0	0
( $\frac{1}{2}, \frac{1}{2}, \frac{1}{2}$ )	$\frac{1}{2}a-2b+2c+3d-3e$	$a-2b+2d-2h+2i$	$a+2b-2d+2h-2i$

<sup>\*</sup>) The column for  $(\Gamma^6)_1$  contains the values  $\sqrt{3} \times F(Q)$ .

REFERENCES

1. S. Hautecler and W. van Dingenen, *J. de Phys.* 25 (1964) 653.
2. R.J. Birgeneau, J. Cordes, G. Dolling, and A.D.B. Woods, *Phys. Rev.* 136 (1964) A1359.
3. S. Hautecler and W. van Dingenen, *Physica* 34 (1967) 257.
4. M. Hatherly, K. Hirakawa, R.D. Lowde, J.F. Mallett, M.W. Stringfellow, and B.H. Torrie, *Proc. Phys. Soc.* 84 (1964) 55.
5. T. Riste, G. Shirane, H.A. Alperin, and S.J. Pickart, *J. Appl. Phys.* 36 (1964) 1076.
6. A. Furrer, T. Schneider, and W. Hälg, *Solid State Comm.* 4 (1966) 99.
7. M.W. Stringfellow, *J. Phys. C* 1 (1968) 950.
8. S.J. Pickart, H.A. Alperin, V.J. Minkiewicz, R. Nathans, G. Shirane, and O. Steinsvoll, *Phys. Rev.* 156 (1967) 623.
9. S. Komura, R.D. Lowde, and C.G. Windsor, in Neutron Inelastic Scattering, Vienna, IAEA (1968), Vol. II, p. 101.
10. H.A. Mook, R.M. Nicklow, E.D. Thompson, and M.K. Wilkinson, *J. Appl. Phys.* 40 (1969) 1450.
11. V.J. Minkiewicz, M.F. Collins, R. Nathans, and G. Shirane, *Phys. Rev.* 182 (1969) 624.
12. C. Kittel, *Phys. Rev.* 110 (1958) 836.
13. E. Schlömann, *J. Appl. Phys.* 31 (1960) 1647.
14. B.Kh. Ishmukhametov, *Fiz. Metal. Metalloved.* 17 (1964) 323, 641.
15. K.B. Vlasov and B.Kh. Ishmukhametov, *JETP (USSR)* 46 (1964) 201; English translation: *Soviet Phys. JETP* 19 (1964) 142.
16. H. Bömmel and K. Dransfeld, *Phys. Rev. Letters* 3 (1959) 83.
17. G.A. Alers, J.R. Neighbours, and H. Sato, *J. Phys. Chem. Solids* 9 (1958) 21.
18. G.A. deWit and B.N. Brockhouse, *J. Appl. Phys.* 39 (1968) 451.
19. E. Frikkee, *Phys. Letters* 34A (1971) 23.
20. E. Frikkee, RCN-140 (1971).

21. E.P. Wigner, Group Theory and its Application to the Quantum Mechanics of Atomic Spectra, New York, Academic Press (1959).
22. V. Heine, Group Theory in Quantum Mechanics, London, Pergamon Press (1960).
23. M. Tinkham, Group Theory and Quantum Mechanics, New York, McGraw-Hill (1964).
24. J.F. Cornwell, Group Theory and Electronic Energy Bands in Solids, Amsterdam, North-Holland Publ. Co. (1969).
25. C.J. Bradley and A.P. Cracknell, The Mathematical Theory of Symmetry in Solids, Oxford, Clarendon Press (1972).
26. J.S. Lomont, Applications of Finite Groups, New York, Academic Press (1959).
27. F. Bloch, Z. Phys. 52 (1928) 555.
28. G.F. Koster, J.O. Dimmock, R.G. Wheeler, and H. Statz, Properties of the Thirty-Two Point Groups, Cambridge, M.I.T. Press (1963).
29. O.V. Kovalev, Irreducible Representations of the Space Groups, New York, Gordon and Breach Science Publ. (1965).
30. W. Opechowski, Physica 7 (1940) 552.
31. R.J. Elliott, Phys. Rev. 96 (1954) 280.
32. L.M. Falicov and J. Ruvalds, Phys. Rev. 172 (1968) 498.
33. E.P. Wigner, Nachr. Ges. Wiss. Göttingen, Math. Phys. (1932) 546 (English translation in |21|).
34. B.A. Tavger and V.M. Zaitsev, Soviet Phys. JETP 3 (1956) 430.
35. J.O. Dimmock and R.G. Wheeler, J. Phys. Chem. Solids 23 (1962) 729.
36. A.P. Cracknell, J. Phys. C, Metal Phys. Suppl. (1970) S175.
37. A.P. Cracknell, Adv. Phys. 17 (1968) 367.
38. M. Born and K. Huang, Dynamical Theory of Crystal Lattices, Oxford, Clarendon Press (1956).
39. A.A. Maradudin, E.W. Montroll, and G.H. Weiss, Solid State Physics, Suppl. 3, New York, Academic Press (1963).



40. E.P. Wigner, Nachr. Ges. Wiss. Göttingen, Math. Phys. (1930) 133  
(English translation in A.P. Cracknell, Applied Group Theory,  
Oxford, Pergamon Press (1968)).
41. S.H. Chen, Phys. Rev. 163 (1967) 532.
42. A.A. Maradudin and S.H. Vosko, Rev. Mod. Phys. 40 (1968) 1.
43. J.L. Warren, Rev. Mod. Phys. 40 (1968) 38.
44. L.P. Bouckaert, R. Smoluchowski, and E. Wigner, Phys. Rev. 50  
(1936) 58.
45. S. Wakoh, J. Phys. Soc. Japan 20 (1965) 1894.
46. L. Hodges, H. Ehrenreich, and N.D. Lang, Phys. Rev. 152 (1966) 505.
47. J.W.D. Connolly, Phys. Rev. 159 (1967) 415.
48. E.I. Zornberg, Phys. Rev. B1 (1970) 244.
49. J.M. Tyler, T.E. Norwood, and J.L. Fry, Phys. Rev. B1 (1970) 297.
50. J. Callaway and H.M. Zhang, Phys. Rev. B1 (1970) 305.
51. J. Langlinalis and J. Callaway, Phys. Rev. B5 (1972) 124.
52. T. Izuyama, Progr. Theor. Phys. 23 (1960) 969.
53. T. Izuyama, D.J. Kim, and R. Kubo, J. Phys. Soc. Japan 18 (1963) 1025.
54. F. Englert and M.M. Antonoff, Physica 30 (1964) 429.
55. D.C. Mattis, Phys. Rev. 132 (1963) 2521.
56. E.D. Thompson, Adv. Phys. 14 (1965) 213.
57. M.M. Antonoff, J. Appl. Phys. 38 (1967) 1059.
58. H. Yamada and M. Shimizu, J. Phys. Soc. Japan 22 (1967) 1404.
59. L.R. Walker, "Spin Waves and other Magnetic Modes", in Magnetism,  
editors T. Rado and H. Suhl, New York, Academic Press (1963),  
Vol. I, p. 377.
60. D.M. Edwards, Proc. Roy. Soc. A300 (1967) 373.
61. E.D. Thompson and J.J. Myers, Phys. Rev. 153 (1967) 574.
62. J. Schwinger, Phys. Rev. 73 (1948) 407.

63. L.L. Foldy, Phys. Rev. 83 (1951) 688, 87 (1952) 693.
64. I.I. Gurevich and L.V. Tarasov, Low-Energy Neutron Physics, Amsterdam, North-Holland Publ. Co. (1968).
65. Y.A. Izyumov and R.P. Ozerov, Magnetic Neutron Diffraction, New York, Plenum Press (1970).
66. W. Marshall and S.W. Lovesey, Theory of Thermal Neutron Scattering, Oxford, Clarendon Press (1971).
67. L.I. Schiff, Quantum Mechanics, New York, McGraw-Hill, second edition (1955), § 29.
68. A.J.P. Meyer and G. Asch, J. Appl. Phys. 32 (1961) 330S.
69. H.A. Mook and C.G. Shull, J. Appl. Phys. 37 (1966) 1034.
70. H.A. Mook, Phys. Rev. 148 (1966) 495.
71. C.G. Shull and E.O. Wollan, Phys. Rev. 81 (1951) 527.
72. Ref. [66], p. 62.
73. Ref. [66], p. 52.
74. R.M. Bozorth, Ferromagnetism, New York, D. van Nostrand, Inc. (1951), p. 270.
75. R.J. Elliott, Proc. Roy. Soc. (London) A235 (1956) 289.
76. C.G. Windsor, R.D. Lowde, and G. Allan, Phys. Rev. Letters 22 (1969) 849.
77. R.D. Lowde and C.G. Windsor, Adv. Phys. 19 (1970) 813.
78. S.W. Lovesey and C.G. Windsor, J. de Phys. 32, Suppl. C1 (1971) 573.
79. S.W. Lovesey and C.G. Windsor, Phys. Rev. B4 (1971) 3048.
80. H. Teutsch, Nukleonik 3 (1961) 15.
81. J. Bergsma, Thesis, Leiden (1970); RCN-121 (1970).
82. M.J. Cooper and R. Nathans, Acta Cryst. 23 (1967) 357.
83. R. Stedman and G. Nilsson, Phys. Rev. 145 (1966) 492.
84. M. Nielsen and H. Bjerrum Møller, Acta Cryst. A25 (1969) 547.

85. O. Steinsvoll, IFA NF-20 (1969).
86. H. Bjerrum Møller and M. Nielsen, in Instrumentation for Neutron Inelastic Scattering Research, Vienna, IAEA (1970), p. 49.
87. J. Bergsma and C. van Dijk, RCN-34 (1965); also in Inelastic Scattering of Neutrons by Condensed Systems, BNL 940 (1966), p. 163.
88. R. Stedman, Rev. Sci. Instr. 39 (1968) 878.
89. R.M. Bozorth, Ferromagnetism, New York, D. van Nostrand, Inc. (1951), p. 567.
90. J.J.M. Franse, Thesis, Amsterdam (1969).
91. G. Dolling and A.D.B. Woods, "Thermal Vibrations of Crystal Lattices", in Thermal Neutron Scattering, editor P.A. Egelstaff, London, Academic Press (1965), p. 205.
92. W.A. Kamitakahara and B.N. Brockhouse, in Neutron Inelastic Scattering, Vienna, IAEA (1972), p. 73.
93. J.R.D. Copley, Solid State Comm. 9 (1971) 531.
94. S.A. Werner and R. Pynn, J. Appl. Phys. 42 (1971) 4736.
95. J.C. Slater, Phys. Rev. 52 (1937) 198.
96. J.B. Sokoloff, Phys. Rev. 173 (1968) 617.
97. E.P. Wohlfarth, Proc. Intern. Conf. Magnetism Nottingham (1964), p. 51.
98. E. Frikkee, J. Phys. C 2 (1969) 345, 928.
99. R.J. Elliott, Phys. Rev. 96 (1954) 280.
100. R.H. Parmenter, Phys. Rev. 100 (1955) 573.
101. J.H. van Vleck, Rev. Mod. Phys. 25 (1953) 220.

LIST OF SYMBOLS

		page
$a$	lattice constant	5
$\underline{a}_1, \underline{a}_2, \underline{a}_3$	basis vectors of the primitive lattice	5
$ A\rangle,  A_0\rangle$	final and initial eigenstates of the scattering specimen	32
$a_j^+(\mathbf{q}), a_j(\mathbf{q})$	Boson creation and annihilation operators	40
$b_L$	nuclear scattering length	33
$\underline{b}_1, \underline{b}_2, \underline{b}_3$	basis vectors of the reciprocal lattice	5
$c$	velocity of light	34
$c_{jk\sigma}^+, c_{jk\sigma}$	Fermion creation and annihilation operators	27
$C_{nx}$ , etc.	rotation through $2\pi/n$ about x direction	127
$d_{200}$	spacing between lattice planes (200)	62
$D$	spin-wave stiffness constant	29
$D_{\frac{1}{2}}$	two-dimensional representation based on the spin functions $u_{\pm\frac{1}{2}}$	11
$\underline{D}(\mathbf{q})$	dynamical matrix	16
$d\sigma/d\Omega$	differential scattering cross section	32
$d^2\sigma/d\Omega dE$	double differential scattering cross section	32
$d\Omega$	solid angle element	31
$-e$	electron charge	
$\underline{e} = \underline{Q}/Q$	unit scattering vector	35
$E$	identity transformation	127
$\overline{E}$	rotation through $2\pi$	11
$E, E_0$	final and initial energy of the neutron	32
$\underline{E}$	unit matrix	128
$E_F$	Fermi energy	45
$E_i$	energy eigenvalue	
$E(jk\sigma)$	energy eigenvalue of electron	22
$F_L(\mathbf{Q})$	magnetic form factor	35
$F(\mathbf{Q})$	structure factor of a localized mode	115, 147
$f(\underline{r})$	radial part of one-electron wave function	23
$g, g_0$	order of group $G, G_0$	7
$g$	gyromagnetic ratio of electron	44
$g(\omega)$	phonon frequency distribution	43
$G$	space group	6

	page
$G_o$	point group 8
$G_o^M$	unitary subgroup of the magnetic point group 13
$G_o^{PM}$	pseudo-magnetic point group 15
$G_o(\underline{q})$ , etc.	point group of the wave vector $\underline{q}$ 9
$G_o(\underline{Q})$ , etc.	point group of the scattering vector $\underline{Q}$ 48
$H$	Hamiltonian
$H_o$	Hamiltonian of unperturbed system
$H'$	perturbation operator
$\hbar$	Planck's constant divided by $2\pi$
$\hbar\omega$	energy loss of the neutron 32
$\underline{H}(\underline{r})$	magnetic field 34
$I$	space inversion 127
$\text{Im}$	imaginary part of complex number 44
$j$	band or branch index 16,22
$\underline{k}, \underline{k}_o$	final and initial wave vector of the neutron 31
$\underline{k}$	electron wave vector 22
$k_B$	Boltzmann's constant
$\underline{L}$	lattice vector 5
$l_\alpha$	dimension of representation $\Gamma^\alpha(T)$ 7
$L$	$\underline{q} = (\frac{1}{2}, \frac{1}{2}, \frac{1}{2})$ 19
$m_n$	neutron mass
$m_p$	proton mass
$m_e$	electron mass
$\underline{m} = \underline{M}/M$	unit vector along magnetization direction 42
$M$	average mass of a Ni atom 15
$\underline{M}$	magnetization vector 13
$M(\underline{q})$	magnetic point group 13
$\underline{n}$	primitive translation 8
$n_{j\underline{k}\sigma}$	Fermion occupation number 28,45
$n_j(\underline{q})$	Boson occupation number 40
$N$	number of lattice sites 8
$O(\underline{r}, t)$	arbitrary operator 32
$P_i$	momentum operator of $i$ -th electron 21
$P(A_o), P(s_o)$	statistical weight factors 32
$P(T)$	operator corresponding to transformation $T$ 7
$P_{ij}^\alpha$	projection operator 7
$\underline{q}$	wave vector of a collective excitation 8,16,28

	page
$\underline{Q} = \underline{k}_o - \underline{k}$	scattering vector 32
$Q$	rotation transforming $\underline{q}$ into $-\underline{q}$ or $-\underline{q} + \underline{l}$ 12
$\underline{r}_i$	position vector of $i$ -th electron 21
$R$	proper or improper rotation 8,128
$\bar{R} = \bar{E}R$	extra rotation belonging to double group 11
$\text{Re}$	real part of complex number 45
$R_i$	class of transformations 127
$R(\omega, \underline{q})$	resolution function 56
$\underline{R}_L(t)$	position of atom at lattice site $\underline{l}$ 15
$s, s_o$	spin quantum numbers of scattered and incident neutron 31
$S_L$	effective spin of atom at site $\underline{l}$ 35
$\underline{S}(\underline{r})$	spin density distribution 34
$\underline{S}(\underline{q})$	Fourier transform of $\underline{S}(\underline{r})$ 44
$S^+$	$= S^x + iS^y$ 44
$S_k^+$	spin raising operator for itinerant electrons 28
$t$	time variable
$T$	absolute temperature
$T = \{R \underline{n}\}$	transformation consisting of a rotation $R$ and a translation $\underline{n}$ 6
$T$	translation group 9
$u_{\pm \frac{1}{2}}$	spin functions 11,22
$u_{jk}(\underline{r})$	periodic part of one-electron wave function 22
$\underline{u}$	displacement vector for localized mode 114,144
$\underline{u}_L(t)$	displacement of atom at lattice $\underline{l}$ 15
$v$	velocity of electron 34
$v_o$	volume of the primitive cell 5
$v_o$	velocity of incident neutron 52
$V_n, V_m$	nuclear and magnetic interaction operators 33,34
$V(\underline{r}_i)$	lattice potential 21
$V(\underline{q})$	matrix element for electron-electron interaction 28,46
$W(Q)$	Debye-Waller factor 36
$w_{j\sigma}(\underline{r}-\underline{l})$	Wannier function 109
$X_i$	irreducible representation of point group $D_{4h}$ 134
$X$	$\underline{q} = (1,0,0)$
$\alpha$	Cartesian component index

		page
$\alpha_i$	interatomic force constant	17
$B$	Cartesian component index	
$B_i$	interatomic force constant	17
$\gamma$	Cartesian component index	
$\gamma$	gyromagnetic ratio of neutron	34
$\gamma_i$	interatomic force constant	17
$\Gamma^i, \Gamma^\alpha(T)$	representation	7
$\Gamma_S^\alpha$	single-valued irreducible representation	11
$\Gamma_D^\beta$	double-valued irreducible representation	11
$\Gamma^\alpha(s)(T')$	subduced representation of $\Gamma^\alpha(T)$	8
$\delta_3$	interatomic force constant	17
$\delta_{i,j}, \delta_{ij}$	Kronecker delta function: $\delta_{ij} = 0$ if $i \neq j$ and 1 if $i = j$	
$\delta(x)$	Dirac delta function: $\delta(x) = 0$ if $x \neq 0$ ; $\int dx \delta(x) = 1$	
$\Delta_i$	irreducible representation of point group $C_{4v}$	133
$\epsilon(k)$	energy of one-electron state	28
$2\theta_A, 2\theta_M$	scattering angles at analyzer and monochromator crystals	50,54
$\Theta$	time reversal operator	13
$\Theta_D$	Debye temperature	39
$\lambda_0$	wave length of incident neutron	62
$\Lambda_i$	irreducible representation of point group $C_{3v}$	135
$\mu$	magnetic moment of neutron	34
$\mu_B$	Bohr magneton ( $= e\hbar/2m_e c$ )	34
$\mu_N$	nuclear magneton ( $= e\hbar/2m_p c$ )	34
$\nu, \nu(q)$	frequency or dispersion relation	
$\underline{\epsilon}_j$	phonon polarization vector	16
$\rho$	radius of curvature for chopper slits	52
$\underline{\sigma}$	electron spin	22,34
$\sigma_n, \sigma_m$	nuclear and magnetic scattering cross section	38
$\Sigma_i$	irreducible representation of point group $C_{2v}$	131
$\underline{\tau}$	reciprocal lattice vector	6
$\phi$	scattering angle at specimen	51,54
$\underline{\Phi}$	interatomic force constant matrix	15

		page
$\chi_{\alpha}(T)$	character of representation $\Gamma^{\alpha}(T)$ ( $= \sum_j \Gamma_{jj}^{\alpha}(T)$ )	7
$\chi_{\alpha\beta}^{\pm}, \chi_{\alpha}^{\pm}$	dynamic susceptibility	44
$\chi_{\alpha\beta}^{\pm}, \chi_{\alpha}^{\pm}$	dynamic susceptibility of non-interacting electrons	45
$\psi$	specimen orientation	51,54
$\psi_i^{\alpha}$	eigenfunction transforming as the i-th row of $\Gamma^{\alpha}$	7
$\psi_{jk\alpha}(\underline{r})$	eigenfunction of electron	18
$\underline{\psi}$	eigenvector of localized mode	112,143
$\omega_{ch}$	chopper frequency	52
$\omega(\underline{q})$	magnon dispersion relation	29
$\omega_j(\underline{q})$	phonon dispersion relation	16
$\Omega$	solid angle	31



#### SUMMARY

The present thesis deals with excitations in ferromagnetic nickel in the frequency range between 1 and 10 THz, the interest being focused on the mutual interaction between the excitations in the electron system (magnons and electron-hole excitations) and those in the crystal lattice (phonons). The experimental investigation was carried out on natural Ni by means of two neutron spectrometers installed at the High Flux Reactor in Petten. All the experiments except one were performed at room temperature, both on multidomain and single-domain single crystals. A separate experiment was performed at  $T = 82$  K.

To investigate the coupling between the electrons and the phonons, a search was made for magnetic perturbations of the phonons. From the observation of "forbidden" neutron-phonon scattering along the symmetry directions  $[100]$  and  $[111]$  it was concluded that the polarization vectors of the phonons deviate from the directions expected in a crystal with cubic symmetry. The deviations of the polarization directions were interpreted as a result of the spin-orbit coupling of the electrons, which leads to a reduction in the symmetry of the crystal.

In addition to the phonons and magnons, a new type of excitation was found. The formation of these excitations, which possess both electronic and vibrational properties, is probably a result of electron-phonon interaction. Various mixed modes with different transformation properties were observed. Each of the modes could only be observed in a limited region of the Brillouin zone, their neutron scattering cross section being strongly dependent on the orientation of the scattering vector  $\underline{Q}$  and the magnetization direction. The energy of each mode was found to be almost independent of the wave vector, and the analysis of the experimental data led to the conclusion that the spin quantum number  $S^z$  of the modes is probably zero. Most of these results could be explained by assuming that the mixed modes consist of a localized lattice vibration coupled with a polar electron-hole excitation.

The analysis of the experimental results has to a large extent been carried out by means of group-theoretical methods. Selection rules were applied to derive the transformation properties of the perturbed phonons and the mixed modes from the scattering cross sections observed in different points in reciprocal space.

Strikingly enough, the neutron scattering by the mixed modes and the perturbed transverse phonons was found to be in disagreement with the detailed-balance condition, which gives the relation between the cross sections for energy gain and energy loss processes. The perturbed phonons and mixed modes are easily observed in creation (energy loss) processes, but are almost unobservable in annihilation (energy gain) experiments. These results seem to indicate that the localized mixed modes and nearly transverse phonons that are created in an energy loss process, are not in equilibrium with the surrounding lattice. This may be the case if the relaxation time is larger than the time involved in the neutron scattering process.

## SAMENVATTING

Het in dit proefschrift beschreven onderzoek is gericht op de excitaties in ferromagnetisch nikkel, in het bijzonder op de wisselwerking tussen de excitaties in het elektronensysteem (magnonen en elektron-gat excitaties) en de excitaties in het kristalrooster (fononen). Het experimentele onderzoek is uitgevoerd met behulp van inelastische neutronenverstrooiing, waarbij gebruik is gemaakt van twee neutronenspektrometers, opgesteld bij de Hoge Flux Reactor te Petten. Met uitzondering van één experiment bij  $T = 82$  K zijn de metingen verricht bij kamertemperatuur. Als preparaat zijn éénkristallen van natuurlijk nikkel gebruikt, aanvankelijk ongemagnetiseerd, later gemagnetiseerd langs symmetrierichtingen.

De wisselwerking tussen elektronen en fononen kon worden aangetoond door de waarneming van magnetische storingen in de roostervibraties. Uit het optreden van "verboden" neutron-fononverstrooiing langs de  $[100]$  en  $[111]$  richtingen kon worden afgeleid dat de polarisatievectoren van de transversale fononen afwijken van de richtingen die voor een kristal met kubische symmetrie verwacht worden. Deze afwijkingen in de polarisatierichtingen worden toegeschreven aan een verlaging van de kristalsymmetrie als gevolg van de spin-baankoppeling van de elektronen.

Behalve fononen en magnonen zijn, onverwacht, gemengde excitaties waargenomen. Het bestaan van deze excitaties, die zowel magnetische als vibratieachtige eigenschappen blijken te bezitten, is waarschijnlijk een gevolg van de wisselwerking tussen de elektronen en het kristalrooster. Verschillende gemengde excitaties, te onderscheiden aan de hand van hun transformatie-eigenschappen, konden worden waargenomen. Elke excitatie bleek echter slechts in een beperkt gebied van de Brillouin zone waarneembaar te zijn, waarbij de werkzame doorsnede voor verstrooiing bovendien sterk afhankelijk is van de richting van de magnetisatie ten opzichte van de verstrooiingsvector. De energie van elke excitatie bleek nagenoeg onafhankelijk van de golfvector te zijn. Daarnaast kon uit de resultaten afgeleid worden dat de excitaties waarschijnlijk geen magnetisch moment bezitten ( $S^Z=0$ ). De meeste van bovengenoemde resultaten konden worden verklaard door aan te nemen dat de gemengde excitaties ontstaan door een koppeling tussen een lokale roostervibratie en een polaire electron-gat excitatie.

Bij de analyse van de experimentele resultaten is veelvuldig gebruik gemaakt van methoden uit de groepentheorie. Selectieregels zijn gedefinieerd voor de verstrooiing van neutronen door willekeurige excitaties in een kristal, waarna met behulp van deze regels de transformatie-eigenschappen van de waargenomen gestoorde fononen en gemengde excitaties zijn afgeleid uit de grootte van de werkzame doorsnede in verschillende punten van de reciproke ruimte.

In tegenstelling tot de verwachting bleek, dat de neutronenverstrooiing door de gemengde excitaties niet voldeed aan de "detailed-balance" voorwaarde, waardoor de verhouding tussen de werkzame doorsneden voor creatie- en annihilatie-processen wordt bepaald. De gestoorde transversale fononen en gemengde excitaties zijn goed waarneembaar in creatie-processen, daarentegen niet of nauwelijks in annihilatie-processen. In dit resultaat kan mogelijk een aanwijzing gezien worden dat de aangeslagen excitaties gedurende het verstrooiingsproces niet in thermisch evenwicht met het omringende rooster komen. Dit zou zich voor kunnen doen als de relaxatietijd groter is dan de tijd gedurende welke het verstrooiingsproces plaats vindt.

NAWOORD

Velen hebben op verschillende wijze medewerking verleend tijdens het in dit proefschrift beschreven onderzoek, en daarna bij de totstandkoming van het proefschrift zelf. Gaarne wil ik mijn dank en erkentelijkheid hiervoor uitspreken.

De grote belangstelling van Dr. B.O. Loopstra voor het onderzoek heeft mij sterk ik mijn werk gestimuleerd. De gesprekken met hem en met Dr. P.F. de Chatel zijn van grote betekenis geweest voor de voortgang van de experimenten en het uiteindelijke resultaat ervan.

Dr. J. Bergsma en Dr. C. van Dijk dank ik voor hun bereidheid de drie-kristalspektrometer geruime tijd ter beschikking te stellen.

De vliegtijdspektrometer werd ontworpen door de heer S. Slagter, die bovendien, in samenwerking met de heer P.H.J. Disseldorp, veel steun heeft verleend bij het oplossen van technische problemen die zich tijdens het onderzoek voordeden. De bouw en het onderhoud van de elektronische apparatuur werden verzorgd door de heren Th.H. Terwisscha van Scheltinga, H. Ames en P. Borst. Bovendien is bij de uitvoering van de experimenten medewerking verleend door de reactorbedrijfsgroep.

De directie van het Reactor Centrum Nederland ben ik erkentelijk voor de mogelijkheid de tekst tegelijkertijd als proefschrift en als extern rapport (RCN-185) te laten verschijnen. De figuren werden op zorgvuldige wijze vervaardigd door de heer F. de Jong. Veel waardering heb ik voor de uitvoering van het typewerk, dat in nauwe samenwerking werd verzorgd door mevr. Ph.Y. de Boer-Heiliegers, mej. M.J.M. Ligthart en mej. G.E. Möls. De reprografische dienst onder leiding van de heer E. van Rooy dank ik voor de druktechnische uitvoering.

Tenslotte dank ik mijn vrouw voor de steun en hulp die zij mij tijdens de totstandkoming van dit proefschrift gegeven heeft.

#### CURRICULUM VITAE

De auteur van dit proefschrift werd in 1934 geboren te Edam. Hij bezocht de Rijks Hogere Burgerschool te Purmerend waar hij in 1953 het eindexamen B aflegde. Na vervulling van zijn militaire dienstplicht begon hij in 1955 met zijn studie aan de Rijksuniversiteit te Leiden. In 1958 legde hij het candidaatsexamen A' af in de natuur- en wiskunde met bijvak sterrekunde. Gedurende de studie voor het doctoraalexamen nam hij deel aan experimenteel onderzoek op het gebied van de magnetische susceptibiliteit van éénkristallen, onder leiding van Prof. Dr. J. van den Handel. Daarnaast verleende hij assistentie bij het natuurkunde practicum. Bovendien was hij tijdens het studiejaar 1961/62 werkzaam in de groep Neutronenfysica van het Instituut for Atomenergi (IFA) te Kjeller, Noorwegen, waar hij als stagiair gedetacheerd was door het Reactor Centrum Nederland (RCN). Tenslotte legde hij in juli 1962 het doctoraalexamen natuurkunde met bijvak klassieke mechanica af. In augustus 1962 trad hij als wetenschappelijk medewerker in dienst van het RCN. Van 1962 tot 1965 was hij gedetacheerd bij het IFA te Kjeller, waar hij onderzoek verrichtte op het gebied van ferromagnetische metalen. Vervolgens zette hij zijn werkzaamheden voort in de groep Neutronenfysica van het onderzoekcentrum te Petten, waar gedurende de periode 1969-1972 het in dit proefschrift beschreven onderzoek werd uitgevoerd.







